2019-06

Multi-scale Gas Flow in Shale Pores with Water Films

Li, Ran

UNIVERSITY OF CALGARY

Multi-scale Gas Flow in Shale Pores with Water Films

by

Ran Li

A THESIS

SUBMITTED TO THE FACULTY OF GRADUATE STUDIES

IN PARTIAL FULFILMENT OF THE REQUIREMENTS FOR THE

DEGREE OF DOCTOR OF PHILOSOPHY

GRADUATE PROGRAM IN CHEMICAL AND PETROLEUM ENGINEERING

CALGARY, ALBERTA

JUNE, 2019

Abstract

This study first puts forward an analytical model for calculating gas velocity profiles and predicting gas apparent permeability enhancement factors in shale nanometer scale characteristic dimensions of different geometries (slit pores and circular pores). The proposed model considers the presence of a mobile high-viscosity water film through modified boundary conditions at a liquid-solid interface and a gas-liquid interface on the basis of the governing equations for pressure-driven flow, finding good agreements with experimental data and validating that a mobile high-viscosity water film enhances gas flow capacity. A mobile bulk water layer is introduced on the basis of the above derived model to explain the case of high water saturation. Next, water-gas phase behaviors are studied in shale rocks with a wide range of pore size distributions rather than single nanopores based on the fractal theory. Also, the research focus will then be switched from the pore scale to the reservoir scale. With a specific pore distribution, gas-water relative permeability can be calculated accordingly, which is a necessity for shale gas simulation study. Finally, with the introduction of the previously derived gas apparent permeability model and the relative permeability curves, reservoir simulation is conducted to evaluate the shale gas production performance. This study has been extended to the case of multiphase flow in shale nanopores and shale rocks, providing a better explanation of the fluid flow pattern in actual reservoir conditions.

Acknowledgements

My gratitude goes to my supervisor Dr. Zhangxing (John) Chen, who keeps providing support and suggestions to guide my research and study. He is always patient and careful to help me with all the problems during my graduate study.

I want to express my sincere appreciation to my examination committee members, Dr. Matthew Alexander Clarke, Dr. Hua Song, Dr. Xin Wang and Dr. Mehdi Ostadhassan. Thanks for their valuable suggestions and opinions.

I also appreciate all the members in the Reservoir Simulation Group and all the sponsors of the Reservoir Simulation Group.

Table of Contents

List of Tables

List of Figures and Illustrations

List of Symbols, Abbreviations and Nomenclature

Symbol	Parameter
a	constant, dimensionless
A	Hamaker constant, J
A_{ge}	equivalent gas cross-sectional area of the whole network, m^2
A_{gek}	equivalent gas cross-sectional area of the M^k parallel capillaries, m^2
A_{gws}	Hamaker constant of gas-water-solid system, J
A_{we}	equivalent water cross-sectional area of the whole network, m^2
A_{wek}	equivalent water cross-sectional area of the M^k parallel capillaries, m^2
A_{wgw}	Hamaker constant of a water-gas-water system, J
b	slip coefficient, dimensionless
b_0	slip factor, Pa
C	constant, dimensionless
d	constant, dimensionless
D	surface diffusion coeffcient, m^2/s
D_d	fractal dimension for capillary diameter distribution, dimensionless
D_f	fractal dimension, dimensionless
$D_{f,g}$	fractal dimension for gas phase, dimensionless
$D_{f,w}$	fractal dimension for water phase, dimensionless
D_l	fractal dimension for capillary length distribution, dimensionless
ΔE	water monomer binding energy, kJ/mol
f	constant, dimensionless
g	constant, dimensionless
G	Gibbs energy of the phase, J

h	height of the slit pore, m
h_e	stable water film thickness, m
h_f	water film thickness, m
h_{in}	pore height at the gas flow entrance, m
h_{out}	pore height at the gas flow exit, m
h_w	thickness of water layer, m
h_{wb}	thickness of bulk water film, m
h_{wh}	thickness of high-viscosity water film, m
j	constant, dimensionless
k	branch level, dimensionless
k_a	gas apparent permeability, m^2
k_B	Boltzmann constant, 1.381×10^{-23} J/K
$K_{e\tau}$	absolute permeability of whole network with branching angle, m^2
K_g	gas apparent permeability with the mobile high-viscosity water film, m^2
K_{ge}	gas equivalent permeability of the whole network, m^2
K_{gek}	gas equivalent permeability in the kth level capillary, m^2
$K_{ge\tau}$	gas equivalent permeability of whole network with branching angle, m^2
K_{gg}	gas permeability in gamma distribution network, m^2
K_{gi}	gas apparent permeability with the static high-viscosity water film, m^2
K_{gk}	gas permeability in the kth level capillary, m^2
K_{gl}	gas permeability in log-normal distribution network, m^2
K_{gnb}	gas apparent permeability without bulk water film, m^2
K_{gp}	gas equivalent permeability of traditional parallel network, m^2

$K_{gp\tau}$	gas equivalent permeability of traditional parallel network with branching angle, m^2
K_n	Knudsen number, dimensionless
k_{rg}	gas relative permeability, dimensionless
k_{rw}	water relative permeability, dimensionless
k_s	coefficient for structural force, N/m^2
K_{we}	water equivalent permeability of the whole network, m^2
K_{wek}	water equivalent permeability in the kth level capillary, m^2
$K_{we\tau}$	water equivalent permeability of whole network with branching angle, m^2
K_{wg}	water permeability in gamma distribution network, m^2
K_{wk}	water permeability in the kth level capillary, m^2
K_{wl}	water permeability in log-normal distribution network, m^2
k_∞	intrinsic permeability, m^2
l	characteristic wavelength, m
L	length of the pore model, m
L_0	straight-line distance, m
L_{BD}	dimensionless groups
l_{ge}	gas flow length of the whole network, m
l_{gek}	equivalent gas flow length of the M^k parallel capillaries, m
l_{gk}	pore length at branch level k, m
l_k	pore length at branch level k, m
l_{ls}	true slip length, m
L_s	length of liquid slugs, cm
L_t	actual path length, m
l_{we}	water flow length of the whole network, m

l_{wek}	equivalent water flow length of the M^k parallel capillaries, m
l_{wk}	pore length at branch level k, m
m	total number of branch level, dimensionless
M	branching number, dimensionless
M_g	gas molecular weight, kg/mol
n	constant, dimensionless
n_i	refractive index of Material i, dimensionless
n_L	liquid particle number density, dimensionless
N_s	dimensionless groups
n_t	foam texture, 1/cm
o_1	fitting coefficient, dimensionless
o_2	fitting coefficient, dimensionless
o_3	fitting coefficient, dimensionless
p	constant, dimensionless
P	pressure, Pa
P_0	saturated vapor pressure, Pa
P_c	critical pressure, Pa
P_e	excess pressure, Pa
P_l	Planck constant, 6.626×10^{-34} J·s
P_m	mean pressure, Pa
P_r	reduced pressure, dimensionless
P_v	vapor partial pressure, Pa
ΔP	applied pressure difference between the entrance and exit, Pa
ΔP_g	gas phase pressure drop of the whole network, Pa

ΔP_{gk}	gas phase pressure drop in the kth level capillary, Pa
ΔP_{w}	water phase pressure drop of the whole network, Pa
ΔP_{wk}	water phase pressure drop in the kth level capillary, Pa
q	constant, dimensionless
Q	volumetric flow rate, m^3/s
Q_g	volumetric rate of gas flow, m^3/s
Q_{gd}	Darcy volumetric rate of gas flow, m^3/s
Q_{gg}	volumetric rate of gas flow in gamma distribution network, m^3/s
Q_{gk}	volumetric rate of gas flow at branch level k, m^3/s
Q_{gl}	volumetric rate of gas flow in log-normal distribution network, m^3/s
Q_{HP}	volumetric flow rate calculated with non-slip boundary, m^3/s
Q_{wk}	volumetric rate of water flow at branch level k, m^3/s
Q_{wb}	volumetric rate of bulk water flow, m^3/s
Q_{wg}	volumetric rate of water flow in gamma distribution network, m^3/s
Q_{wh}	volumetric rate of high-viscosity water flow, m^3/s
Q_{wl}	volumetric rate of water flow in log-normal distribution network, m^3/s
R	gas constant, 8.314 J/(K·mol)
r	pore radius, m
r_0	pore radius, m
r_{0in}	pore radius at the gas flow entrance, m
r_{0out}	pore height at the gas flow exit, m
r_c	plateau border radius, cm
r_{cap}	capillary radius, cm
r_D	dimensionless radius, dimensionless

r_e	equivalent flow radius in the equivalent single channel, m
r_g	radius of gas flow in traditional parallel network, m
r_{g0}	radius of gas flow in the first-level capillary, m
r_k	pore radius at branch level k, m
S	effective surface area, m^2
S_w	water saturation, dimensionless
S_{wk}	water saturation in the kth level capillary, dimensionless
T	temperature, K
T_c	critical temperature, K
u	liquid flow velocity, m/s
v_g	gas velocity, $\mathrm{m/s}$
v_{gi}	gas velocity with the static high-viscosity water film, $\mathrm{m/s}$
v_{gs}	gas slip velocity, $\mathrm{m/s}$
v_{ls}	liquid slip velocity, $\mathrm{m/s}$
V_m	water molar volume, m^3/mol
v_w	water velocity, $\mathrm{m/s}$
v_{wb}	bulk water velocity, $\mathrm{m/s}$
v_{wh}	high-viscosity water velocity, $\mathrm{m/s}$
W	width of the slit pore, m
W_A	work of adhersion, J/m^2
X	length or area or volume of an object
z	direction perpendicular to the flow direction, dimensionless
Z	gas compressibility factor, dimensionless
z_D	dimensionless height, dimensionless

η	viscosity coefficient, Pa·s
α	fraction of an effective surface area occupied by solid, dimensionless
θ	contact angle, dimensionless
δ	thickness of a reduced water viscosity layer, m
ϵ_i	zero-frequency dielectric constant of material i, dimensinless
μ_g	gas viscosity, Pa·s
μ_{g0}	gas viscosity at $P = 1.01325 \times 10^5 Pa$ and $T = 423\ K$, Pa·s
μ_s	foam apparent viscosity, cp
μ_w	water viscosity in the interface region, Pa·s
μ_{wh}	high water viscosity near the wall, Pa·s
μ_{wb}	water viscosity in the interface region, Pa·s
μ_1	bulk water viscosity, Pa·s
μ_2	the reduced water viscosity, Pa·s
μ_∞	bulk water viscosity, Pa·s
σ	interfacial tension, dyne/cm
σ_l	liquid surface tension, N/m
σ_v	tangential momentum accommodation coefficient, dimensionless
λ	mean free path, m
λ_{cl}	characteristic length of water molecules, m
λ_s	slip coefficient, Pa·s/m
τ	pore tortuosity, dimensionless
Φ	excess free energy, J
ϕ_g	porosity occupied by gas, dimensionless
ϕ_0	porosity, dimensionless

$\Pi_{circular}(h_w)$	disjoining pressure of circular pore, Pa
$\Pi_e(h)$	electrostatic component of disjoining pressure, Pa
$\Pi_m(h)$	molecular component of disjoining pressure, Pa
$\Pi_s(h)$	structural component of disjoining pressure, Pa
$\Pi_{slit}(h_w)$	disjoining pressure of slit pore, Pa
$\Pi_1(h_w)$	force between water film and its absorbed surface, Pa
$\Pi_2(h_w)$	force between water film and the opposite surface, Pa
$\Pi_3(h_w)$	force between two water films, Pa
ε	relative dielectric permittivity of water, dimensionless
ε_0	electric constant in vacuum, F/m
ε_{II}	interaction between water atoms, kJ/mol
ε_{SI}	interaction between wall atom and water atom, kJ/mol
ε_{SS}	interaction between wall atoms, kJ/mol
ξ_1	electric potentials at the solid-water interface, V
ξ_2	electric potentials at the water-gas interface, V
γ	gas-water surface tension, N/m
ς	wedging coefficient, dimensionless
β	height decreasing rate along the flow direction, dimensionless
ζ	branching angle, degree
ω	pore diameter, m
ω_{max}	the largest pore diameter, m
ω_{min}	the smallest pore diameter, m

CHAPTER ONE: INTRODUCTION

Due to its advantages in terms of prices and CO_2 emissions, shale gas occupies an increasing share in the total energy production (Carey, 2012). In 2016, Energy Information Administration (EIA) predicted that the worldwide natural gas production would increase from 9.7×10^9 m^3 in 2015 to approximately 1.57×10^{10} m^3 in 2040. As a part of total natural gas production, shale gas was projected to grow both in terms of proportion (which would account for 30% of the total natural gas production in 2040) and absolute volume (which was expected to triple in 2040) (EIA, 2016). On this account, it is highly required to understand fluid transport mechanisms in shale formations to enhance shale gas recovery.

The complex geological structure and mineral composition bring about the deviation of shale gas behaviors from that of conventional gas. To figure out how gas molecules move through pores and throats with a size ranging from microscale down to nanoscale is essential to forecast and optimize shale gas production. Also, an efficient exploitation of low permeable shale formations with abundant micropores and nanopores usually requires horizontal well drilling and hydraulic fracturing to mobilize and recover trapped hydrocarbons. Horizontal well drilling is conducive to generate substantial contact areas with shale rocks to maximize the natural gas output. Hydraulic fracturing, for example, enables the creation of extensive artificial fractures to generate connectivity and provide numerous flow paths for the trapped shale gas, compensating for the limited flow capacity of nature fractures (Vidic et al., 2013; Wu et al., 2016). The subsequent injection of a fracturing fluid, together with the initial water, creates a multiphase flow condition in a fracture network containing nanopores in shale gas reservoirs. Therefore, the effect of water

layer existence should be taken into consideration during the prediction and evaluation of gas flow patterns.

In this study, on the basis of the governing equations for pressure-driven flow, gas flow models in the presence of water are established to measure the contributions of mobile water films to gas transport in different geometries (slit pores and circular pores). To reveal how rock wettability modifies fluid behaviors, water molecules true slippage and water viscosity have been calculated as a function of a contact angle. Likewise, at a gas-liquid contact surface, the presence of gas slippage is introduced to account for the interactions between gas and water molecules as a non-slip boundary is no longer applicable. Next, water-gas phase behaviors will be studied in shale matrix with a bundle of pores rather than single nanopores with fractal theory to evaluate the influence of pore size distribution in shale rocks. Finally, the research focus is switched from pore scale to reservoir scale. With the obtained description of multiphase transport behaviors, reservoir simulation has been conducted to predict the cumulative gas production and gas rate in actual reservoir conditions.

CHAPTER TWO: LITERATURE REVIEW

2.1 Shale Reservoir

Shale is a fine-grained and laminated sedimentary rock characteristically composed of clay-sized and silt-sized mineral particles (Blatt and Robert, 1996). Shale gas, which is mainly composed of methane and reserved in the complex and relatively impermeable shale formations, is becoming one of the main commercial natural gas resources with the advancement of exploitation technologies, bringing about the shale revolution and relieving the energy shortage (Stevens, 2012).

Shale reservoirs are always characterized by severe heterogeneity and multiple scale characteristics, such as natural fractures, micropores and nanopores (Wu et al., 2016). Loucks et al. (2009) divided shale pore sizes into two groups, which are micropores (a pore diameter larger than 0.75 μm) and nanopores (a pore diameter smaller than 0.75 μm) according to their observations of Barnett shale samples. In most cases, shale reservoirs are abundant in nanopores with a small quantity of micropores (Clarkson et al., 2013). The specific composition of shale results in its low porosity and low permeability properties. Image analysis, intrusive method and nonintrusive method are developed to characterize pore petrophysical properties (Li et al, 2015). Image analysis captures images of shale pores to figure out pore dimensions and pore distributions. Moncrieff (2009) provided images of Barnett shale samples and concluded the average porosity was around 2%. Wang and Reed (2009) considered the porosity of kerogen to be less than 25% with a scanning electron microscopy (SEM) image. Intrusive method injects non-wetting liquids and gases at different injection pressure into shale samples and records the injected volume. Tan et al. (2014) tested marine black shale formations on the Upper Yangtze Platform with the mercury injection capillary pressure (MICP) analysis method and found that samples porosities were less

than 4%. Chalmers et al. (2012) used helium isotherm adsorption for Barnett samples and measured the porosity to be 2.5%-6.6%. The porosity decreases with an increase in reservoir temperature, pressure and reservoir depth. Shale permeability is determined by numerous influencing factors, such as pore size and pressure, and ranges from a few nanodarcy to several hundred nanodarcy, which can be tested with steady state and unsteady state (such as pulse transient decay method and oscillating pore pressure method) methods (Henderson et al., 1998; Civan and Donaldson, 1989). Tan et al. (2014) found that the marine black shale formations permeability was less than 20.2 nD. The average matrix permeability of the Paleogene Shahejie Formation in China was determined to be around 27.4 to 31.1 nD. Also, the tortuosity of pores ranging from 2.8 to 10.0 nm was 8.44 (Hu et al., 2017). Shale usually has a large tortuosity, which is an indicator of poor connectivity and low flow capacity (Thomas and Clouse, 1990).

Generally, shale is composed of organic matter such as kerogen and bitumen and inorganic matter, for example, quartz and dolomite as well as clay minerals, among which quartz and clay minerals can account for around 30% and 60% while organic matter accounts for less than 3% proportion (Blatt, 1982). Shale rock is not only the sedimentary rock but also the source rock for gaseous hydrocarbons due to the existence of organic matter (Fertl and Rieke, 1980). Nanopores rich in organic matter tend to be oil-wet while inorganic pores are usually water-wet (Wu et al., 2016). Mineral composition determines fluid flow and distribution pattern, which can be figured out by x-ray diffraction and SEM analysis (Li et al., 2018; Shan et al., 2015).

Pore structures, including pore size, pore distribution, pore type, and pore geometry, are of critical importance to determine reserves and flow characteristics of fluids and further impact the gas

output (Ross and Bustin, 2009). Pore shapes such as circular pores, slit pores, wedged pores, inkbottle-shaped pores and irregular-shaped pores are commonly discovered in shale samples (Zhou et al., 2015). Characterization of the complex shale pore structures and pore types is a necessity to enhance hydrocarbons recovery. For instance, in general, free gas reserved in natural and artificial fractures usually adopts Darcy's flow while bulk gas transport in pores mainly takes the form of continuum flow, slip flow and transitional flow. Adsorbed gas molecules movement relies on adsorption/desorption and gas diffusion in organic pores (Wu et al., 2016). Fan and Ettehadtavakkol (2017) depicted the transport of gaseous hydrocarbons in inorganic pores and organic pores without the consideration of water existence. Under dry condition, shale gas mainly exists in form of free gas in inorganic pores. But it can also be reserved as dissolved gas or adsorbed gas in kerogen matrix. Zhao et al. (2018) showed the effects of water content on inorganic system and organic system. Water molecules were prior to be adsorbed at the inorganic surface and methane molecules and bulk water molecules stayed in the center of the channels. They declared that the water molecules could be transferred into organic pores and be adsorbed at the adsorption sites. Therefore, with the accurate description of shale nanopores characteristics, multiphase fluid transport mechanisms in shale pores of different dimensions can be determined. The complex flow behaviors of shale gas can be figured out with numerous study methods such as numerical simulation, lab experiments and analytical models.

2.2 Gas Slippage

Different pore characteristics appear to have significant effects on gas storage and gas flow behaviors (Loucks et al., 2009). Nanoscale confinement, which ranges from a few nanometers to several hundred nanometers, dominates shale formations compared with microscale confinement

(Curtis et al., 2012; Zhang et al., 2017). Numerous studies have shown that the existence of nanopores, for instance, organic intragranular pores and inorganic intergranular pores, leads to the deviation of gas transport mechanisms and inapplicability of conventional flow equations. This discrepancy has been attributed to the intense molecular interactions between a fluid and pore walls within a limited space (Figure 2-1). Some evidence has been obtained that as long as a pore diameter is large enough in comparison with the mean free path, gas intermolecular collisions are far more frequent than those between gas molecules and pore walls. In this case, continuum flow is the primary gas flow mechanism. As a pore diameter approaches the nanometer scale, the interactions between gas and flow channels become significant. Gas molecules gain a velocity at a gas-solid interface and the gas flux is thus increased to different degrees. In view of the difference in fluid-wall interactions, the flow boundary is no longer regarded as a non-slip boundary and gas slippage has been required to be introduced to modify the classical flow equations (Singh and Javadpour, 2013; Wu et al., 2015c).

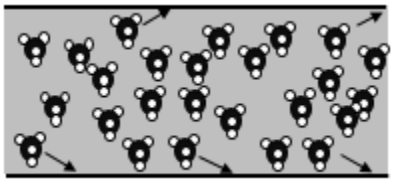

Figure 2-1 Gas slippage schematic diagram.

The Klinkenberg slip theory describes an increase in the gas flow rate by the modification of gas apparent permeability with a gas slip factor (Li et al., 2018). The slip factor is a function of the gas molecular properties and the applied pressure.

$$k_a = k_\infty(1 + \frac{b_0}{P_m}) \quad (2\text{-}1)$$

$$k_\infty = \frac{\phi_0}{\tau}\frac{r_0^2}{8} \tag{2-2}$$

where k_a is the gas apparent permeability, m^2; k_∞ is the intrinsic permeability, m^2; b_0 is slip factor, Pa; P_m is the mean pressure, Pa; ϕ_0 is porosity, dimensionless; τ is tortuosity, dimensionless; r_0 is a pore radius, m. The corrected gas apparent permeability is higher than the intrinsic permeability predicted by the Hagen Poiseuille equation. Gas with smaller molecular weight tends to obtain a larger gas slip factor (Klinkenberg, 1941).

To be more precise, Knudsen number K_n, a ratio of gas mean free path to a representative length scale, is proposed to measure the deviation of bulk gas flow behaviors from continuum flow and distinguish the continnum flow (K_n<10^{-3}), slip flow (10^{-3}< K_n<10^{-1}), transition flow (10^{-1}< K_n<10) and Knudsen diffusion (K_n>10) (Singh and Javadpour, 2013). Wu et al. (2015c) concluded that the Navier-Strokes equations were valid for continuum flow and the Navier-Strokes equations coupled with a gas slippage boundary condition could predict the slip flow accurately. However, in terms of transition flow, the introduction of slip boundary conditions was not enough to capture the flow behaviors accurately. Beskok and Karniadakis (1999) proposed a gas flow model in channels and pipes with a general slip boundary condition and predicted the velocity distribution which agreed well with the continuum flow, slip flow and free molecular flow. Brown et al. (1946) calculated the gas flow at low pressure in copper and iron pipes by a linear addition of continuum flow and slip flow. Thompson and Owens (1975) developed equations with diffuse wall conditions to describe molecular flow on the basis of slip flow and Knudsen diffusion. Considering slip flow and Knudsen diffusion, Javadpour (2009) derived a gas apparent permeablity equation by adding slip flow and Knudsen diffusion linearly. The obtained gas apparent permeablity was higher than Darcy's permeablity. Shabro et al. (2011) used pore-scale model and reservoir simulation with the

consideration of non-slip flow, slip flow, Knudsen diffusion, and Langmuir desorption. They concluded that slip flow and Knudsen diffusion contributed to an increase in gas apparent permeability.

Regarding single gas flow behaviors in shale, reservoir pressure and pore dimension are important influencing factors for shale gas flow behaviors as they determine Knudsen number and flow regime (Sakhaee-Pour and Bryant, 2012). Besides, pore geometry plays a significant role in determing gas transport. Circular pores have larger gas flow capacity than rectanguar pores given a certain cross-section area. A higher aspect ratio of rectangular pores further increases gas apparent permeability (Wu et al., 2015b). Wu et al. (2015c) also evaluated the real gas effect, mentioning that it led to a rise in gas flow capacity and the positive effect was more obvious for a smaller pore with higher pressure. Sun et al. (2017) combined the real gas effect and stress dependence on the basis of Beskok's model. In contrast, they found that the real gas effect had a negligible effect.

Besides bulk gas flow, surface diffusion should also be included for the adsorbed gas flow as organic pores are liable to adsorb gas molecules (Darabi et al., 2012). Wu et al. (2016) divided the surface diffusion models into three categories. Hopping model assumes that if adsorbed gas molecules gain enough energy to leave from one adsoption site to the next one, surface diffusion is activated (Higashi et al., 1963). Hydrodynamic model assumes that surface film viscous flow generates surface diffusion (Gilliland et al., 1958). Fickian model obtains surface diffusion by substracting a bulk gas flow flux from the total gas flow flux as it regards bulk gas flow and surface diffusion as an independent processes and neglects gas desorption (Kapoor et al., 1989). Chen and

Yang (1991) derived a unified model to explain the concentration dependence for surface diffusion based on the hopping theory. With regard to surface diffusion, higher pressure improves gas molecules coverage and further increases surface diffusion. A higher temperature contributes to an increase in a surface diffusion coefficient as the gas desorption is an endothermic process. Also, the properties of gas and solid determine surface diffusion to a certain extent (Wu et al., 2016).

2.3 Liquid Slip

The validity of the above discussion is limited to single gas flow in nanopores. In actual shale rocks, the existence of initial water saturation and the injection of a fracturing fluid disturb gas phase flow and pose influences on gas production (Li et al., 2017). Single water phase flow is first investigated to determine water molecules behaviors at a solid substrate.

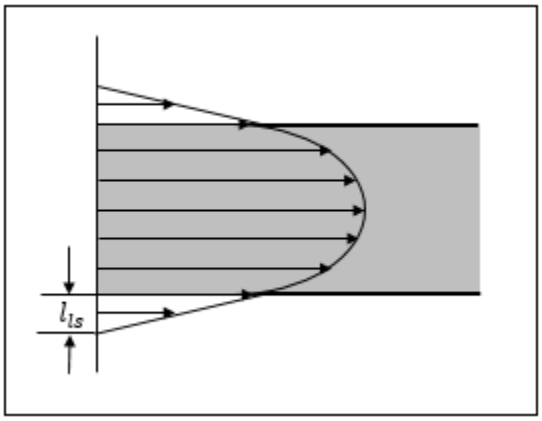

Figure 2-2 Water slippage schematic diagram.

Navier et al. (1823) presented the possibility of liquid slip on a solid surface and defined a slip length l_{ls} to measure it (Figure 2-2). In their study, slip length was determined as the distance from the solid surface to the location where the liquid velocity was extrapolated to zero.

$$v_{ls} = l_{ls} \frac{\partial u}{\partial z} \tag{2-3}$$

where v_{ls} is liquid slip velocity, m/s; l_{ls} is the liquid slip length, m; u is liquid flow velocity, m/s; z is the direction perpendicular to the flow direction.

Blake (1990) developed a liquid slip model involving interfacial wettability on the basis of the molecular-kinetic theory. He defined slip length as the ratio of a viscosity coefficient and a slip coefficient, which was closely related to a contact angle and an effective area occupied by solid molecules (Equation (2-4)):

$$\lambda_s = \frac{\eta}{\delta[e^{\frac{\alpha S \sigma_l (1-cos\theta)}{k_B T}} - 1]} \tag{2-4}$$

where λ_s is a slip coefficient, Pa·s/m; η is a viscosity coefficient, Pa·s; δ is the average distance between the adjacent molecules centers, m; α is the fraction of an effective surface area occupied by solid, dimensionless; S is an effective surface area, m^2; σ_l is liquid-surface tension, N/m; θ is a contact angle, degree; k_B is the Boltzmann constant, 1.381×10^{-23} J/K; T is temperature, K. Then the liquid slip length l_{ls} is manifested as

$$l_{ls} = \delta[e^{\frac{\alpha S \sigma_l (1-cos\theta^0)}{k_B T}} - 1] \tag{2-5}$$

According to Ruckenstein and Rajora (1983), a liquid slip velocity was proportional to a chemical potential gradient and a mobility coefficient. The mobility coefficient was further derived to be a function of a surface diffusion coefficient. The slip velocity and a volumetric flow rate are expressed as:

$$v_{ls} = \frac{D}{n_L k_B T}\frac{\Delta P}{L} \tag{2-6}$$

where v_{ls} is a liquid slip velocity, m/s; D is a surface diffusion coeffcient, m^2/s; n_L is the liquid particle number density, dimensionless; k_B is the Boltzmann constant, 1.381×10^{-23} J/K; T is temperature, K; ΔP is a pressure difference, Pa; L is the capillary length, m.

$$Q = \frac{\Delta P \pi r^4}{8\eta L}(1 + \frac{8\eta D}{n_L k_B T r^2}) \tag{2-7}$$

where Q is the volumetric flow rate, m^3/s; r is the capillary radius, m. Based on the Hagen-Poiseuille equation, the flow rate through capillaries with a liquid slip boundary condition is modified as (Langlois and Deville, 1964):

$$Q = \frac{\Delta P \pi r^4}{8\eta L}(1 + \frac{4l_{ls}}{r}) \tag{2-8}$$

where Q is the volumetric flow rate, m^3/s; ΔP is a pressure difference, Pa; r is the capillary radius, m; η is a viscosity coefficient, Pa·s; L is the capillary length, m; l_{ls} is the slip length, m. Comparing Equation (2-7) and (2-8) calculates the liquid slip length l_{ls}:

$$l_{ls} = \frac{2\eta D}{n_L k_B T r} \tag{2-9}$$

Mattia and Calabrò (2012) attibuted the liquid flow enhancement in carbon nanotubes to solid-liquid molecular interactions such as the work of adhersion and surface diffusion according to Ruckenstein and Rajora's theory. Mentioning that $n_L k_B T L$ was the energy of fluid molecules at an interfacial area and the energy could be replaced by the work of adhesion W_A, they defined the slip velocity by Equation (2-10) and the slip length was further derived as Equation (2-11). They further combined molecular interactions with flow rate model of Myers (2011) and predicted water flow behaviors in carbon nanotubes of different dimensions and wall surface structures.

$$v_s = \frac{D}{W_A}\Delta P \tag{2-10}$$

$$l_{ls} = \frac{2\eta DL}{W_A r} \tag{2-11}$$

where W_A is work of adhesion, J/m^2.

In terms of hydrophilic nanopores, water molecules are liable to be bound and restricted in the vicinity of a wall, as an ordered structure, under the long-range interactions composed of the Van der Waals force, electrostatic force and structural force (Li et al., 2017, 2018). The influences of high-viscosity water films along nanoscale substrates have been extensively investigated and a considerable amount of literature explain the related phenomena. In the case of carbon nanotubes, molecular dynamics (MD) simulations have been applied to validate the existence of confinement-modified water molecules behaviors and structure and the consequent reduction in water mobility in the corresponding region (Mashl et al., 2003). Similar results have been obtained with the evaluation of water-graphene interactions at the nanoscale, where an increase in water viscosity was ascribed to the enhanced non-bonded H-bond interactions between water molecules and a carbon structure (Qin and Buehler, 2015). Another example is the observation of water rate enhancement as a result of a large slip length along a water-solid interface by MD simulations within two parallel graphene layers (Neek-Amal et al., 2016). Based on previous experimental results and simulation data, the water viscosity and a slip length have been expressed as a function of a contact angle, thereby, explaining how surface forces and wettability of nanotubes modify a confined water flow rate (Wu et al., 2017b).

With reduced water viscosity in the vicinity of a wall and the introduction of a slip length, a two water layers flow model was established based on the Hagen-Poiseuille equation by Myers (2011).

The slip velocity was defined to be proportional to the slip length. Finally, the volumetric flow rate turned out to be:

$$Q = Q_{HP}\frac{(r-\delta)^4}{r^4}\{1+\frac{\mu_1}{\mu_2}\left[\frac{r^4}{(r-\delta)^4}-1\right]\} \quad (2\text{-}12)$$

where Q is the volumetric flow rate, m^3/s; Q_{HP} is the volumetric flow rate calculated by the Hagen-Poiseuille equation with a non-slip boundary, m^3/s; r is the capillary radius, m; δ is the thickness of a reduced water viscosity layer, m; μ_1 is the bulk water viscosity, Pa·s; μ_2 is the reduced water viscosity, Pa·s.

True slip and apparent slip are also proposed to describe the situations in which water molecules slide on a solid-liquid interface and a liquid-liquid interface seperately (Neto et al., 2005). Wu et al. (2017b) proposed a model for confined water flow by adding true slip and apparent slip linearly. True slip is discovered as a function of contact angle empirically (Huang et al., 2008). Apparent slip accounts for the confined water viscosity change due to interfacial interactions. In this case, liquid slip flow can be estimated with contact angle, which measures liquid-solid molecular interactions at the interface.

Afsharpoor and Javadpour (2016) investigated the liquid slip flow in shale pores of different geometries and discovered that liquid flow capacity was lower in noncircular pores than in circular pores. Neto et al. (2005) concluded that surface roughness and wettability posed potential influences on liquid slip behaviors. With a constant defined as the ratio of an actual surface area to an apparent surface area, roughness was introduced through a modification of the intrinstic angle (Wenzel, 1936). Bonaccurso et al. (2003) found a rise in slip with the consideration of roughness in experiments with silica surfaces. Hocking (1976) mentioned that roughness contributed to slip

on account of fluid trapping in crevices. In terms of surface wettability, liquid molecules were more easily to move along a solid substrate with a higher contact angle as a result of weaker solid-liquid interactions, leading to a larger slip length. The analysis of surface forces and the consequent determination of contact angle are discussed in the Appendix A.

2.4 Shale Wettability

Due to the complex mineral composition of shale rocks, shale wettability is quite different. Numerous investigation have been conducted as shale wettability determines fluid flow and shale gas production significantly. Siddiqui et al. (2018) stated that shale wettability was usually measured by Amott wettability index, United States Bureau of Mines (USBM) wettability index, Nuclear Magnetic Resonance (NMR) and contact angle. After extensive investigations, they concluded that brine ionic strength, pressure, temperature, pH, surface charge, clay content, and total organic carbon (TOC) were potential influencing factors during the determination of shale wettability.

Sessile drop tests adopted by Borysenko et al. (2009) declared that the advancing water/air contact angle of a hydrophilic shale sample to be around 10 ^{o} to 30 ^{o} and that of a hydrophobic shale sample from the Perth Basin to be 120 ^{o}. The subsequent liquid-liquid extraction tests confirmed a high affinity for water of hydrophilic shale by the comparing the particle distributions between water and oil. Spontaneous imbibition tests showed a high oil recovery rate for hydrophilic shale but an almost zero oil rate for hydrophobic shale. Contact angles ranging from 35 ^{o} to 90 ^{o} were also captured during the imbibition tests on the chips of shale samples from Marcellus Formation. Dehghanpour et al. (2013) prepared 5 shale samples from Fort Simpson (FS), Upper Muskwa

(UM), Lower Muskwa (LM), Upper Otter Park (UOP) and Lower Otter Park (LOP), among which the UOP sample had the highest quartz concentration. The measured air/water contact angles values were 27 º, 38 º, 45 º, 46 º and 50 º respectively. A contact angle digital goniometer instrument was used by Roshan et al. (2015) to measure the contact angles of Evergreen shale sample, which turned out to be 46 º, 30 º and 26 º when testing with 10% NaCl solution, 5% NaCl solution and deionized water.

Wu et al. (2017b) calculated the contact angle with water monomer binding energy, which was obtained with Lennard-Jones parameter related to the wall-water interactions energy (Equations (2-13) to (2-15)). The contact angle can also be calculated with the analysis of surface disjoining pressure as in Appendix A.

$$\varepsilon_{SI} = \sqrt{\varepsilon_{SS}\varepsilon_{II}} \tag{2-13}$$

$$\varepsilon_{SI} = -0.0619\Delta E \tag{2-14}$$

$$\theta = 185.8^{o} + \Delta E \times 14.5^{o} \tag{2-15}$$

where ε_{SS} is the interaction between wall atoms, kJ/mol; ε_{II} is the interaction between water atoms, kJ/mol; ε_{SI} is the interaction between wall atom and water atom, kJ/mol; ΔE is water monomer binding energy, kJ/mol.

2.5 Gas-Water Two-Phase Flow

Evidences of water existence have been illustrated by numerous literature. Gas Research Institute method was applied to measure the original water content to be 42% with Eagle Ford shale samples (Jung et al., 2013). Simpson and Dearing (2000) tested the moisture content of Oligocene shale core and West Delta Pleistocene shale core to be 15% and 12% separately. The water saturation

of Devonian Dunkirk Shale rock reached approximately 10%-30% according to the lab tests of Sondergeld et al. (2010).

According to Liu et al. (2018), the measurement of water saturation in shale gas reservoirs could be carried out by lab tests such as Dean–Stark extraction which relied on distillation extraction of water from the core samples, as well as logging interpretation which focused on the analysis of resistivity and porosity.

How water and gas co-exist in nanoscale pores remains to be a problem. Adefidipe et al. (2014) proposed mathematical equations to simulate two-phase transient flow in hydraulic fractures, which were governed by dynamic relative permeability function. They derived an analytical model to predict shale gas production at early stage assuming that the fracture was filled with gas and water and two phases flow existed. With Monte Carlo simulations, Jin and Firoozabadi (2014) investigated the effect of water on methane sorption in clay minerals. They concluded that water molecules preferential adsorption at clay nanopores reduced methane sorption. To introduce the effects of a water phase and figure out gas-water two-phase interactions in nanopores, Li et al. (2016b) analyzed the disjoining pressure and surface forces to obtain the relationship between a static water film thickness and humidity in different sized inorganic pores, with which they further examined the influences of water saturation on methane adsorption capacity, finding good agreements with experimental data of methane adsorption tests under different humidity. With the modified Beskok's models to describe the bulk-gas transport mechanisms and the consideration of a static adsorbed water film, Sun et al. (2017) have derived a gas apparent permeability model for inorganic pores to reflect the impacts of pore dimensions and humidity. Given that a water film

has been neglected, the gas apparent permeability was overestimated by approximately 11%. Feng et al. (2018) carried out water vapor adsorption tests on montmorillonite, kaolinite and illite to check the contributions of water, concluding that gas storage was liable to be overestimated without the existence of static water vapor and its influences on methane adsorption were relatively minimal. Besides inorganic pores, Zhao et al. (2018) also conducted MD simulation to verify the impacts of water content on methane adsorption on kerogen.

The pressure-driven gas-water two phase flow is also investigated. In order to obtain the relationship between flow patterns and fluids transport, Ho and Striolo (2015) used MD simulation to study water and methane two phase flow in slit nanopores. Cao et al. (2017) investigated two phase flow in fractures with the deviation of partial differential equations and found that the water phase flow impacts both the short-term and long-run shale gas production. Based on the Hagen-Poiseuille equations, Li et al. (2016) adopted capillary curves to introduce the interfacial effect between the gas phase and water phase. Similarly, Zhang et al. (2017) put forward a gas-water two-phase flow model with the combination of gas slippage, multilayer sticking and a water film in circular nanotubes to obtain gas-water relative permeability.

2.6 Gas-Water Relative Permeability of Shale Rocks

Relative permeabilities are able to describe multiphase transport properties of porous media and determine oil and gas output. Obtaining relative permeabilities accurately is rather difficult as random pore structures, complex rock composition and various reservoir conditions tend to impact the fluid flow capacity significantly. To predict flow patterns and interactions of the wetting and non-wetting phases, numerous studies have been conducted to measure and calculate relative

permeability curves with laboratory measurements, simulation and analytical approaches (Zhang et al., 2018).

Generally, steady-state and unsteady-state methods are the frequently used to obtain relative permeability curves. For the steady-state method, two phases are injected into pre-treated cores simultaneously at given rates and pressures. In terms of the unsteady-state method, one phase is displaced by another phase. Darcy's law is then applied to calculate effective permeabilities at each saturation (Henderson et al., 1998; Civan and Donaldson, 1989). The steady-state experimental method was chosen to measure nitrogen/water and steam/water relative permeabilities and a gas slip factor with Berea sandstones by Li and Horne (2004). With pretreated core samples from Bossier sands in Mimms Creek Field, Rushing et al. (2003) tested nitrogen/water relative permeabilities with the steady-state method at pressure differences of 10, 100, 500, 1000 and 8000 psi. It has been discovered that an increase in water saturation leads to a drop in the gas permeability.

However, the experimental methods are time-consuming and inconsistent in most cases. Simulations such as Lattice Boltzmann Model (LBM) and Monte Carlo simulation are widely carried out to simulate the multiphase flow in the described complex porous media (Chen and Doolen, 1998; Xiao et al., 2012). LBM deals with complex boundary conditions and incorporates microscopic interactions. Pan et al. (2001) applied Lattice Boltzmann (LB) and pore network modeling to simulate single phase flow in log-normal sphere-size distributed packing and related the permeability to porosity. The effects of a nanoscale pore structure on relative permeabilities were reported by Ma et al. (2018). With Graphics Processing Unit (GPU) enhanced Multiple-

Relaxation-Time LBM, air/water permeabilities were analyzed using bead packings with the incorporation of a modified slip boundary.

Due to the uncertainty of related empirical parameters and computational time, analytical models are proposed to identity the phase flow characteristics according to the assumed theoretical governing equations and boundary conditions in the proposed pore structures (Zhang et al., 2017). On the basis of the Hagen-Poiseuille equation and capillary equations, Li et al. (2016) modeled gas-water relative permeabilities in nanopores with interfacial effects and checked the influences of pore dimensions, surface diffusion and contact angle. Zhang et al. (2017) considered gas slippage, multilayer sticking and a water film in circular nanopores to calculate gas-water relative permeabilities.

2.7 Shale Pore Size Distribution

SEM, MICP and nitrogen gas (N_2) adsorption tests are frequently used to test the shale pore size distribution. Ghanbarian and Javadpour (2017) plotted log-normal pore size distribution of Eagle Ford Shale, Pierre Shale and Barnett Shale obtained with mercury intrusion method. Wang et al. (2017) also reported log-scale pore size distribution with an Eagle Ford shale sample. Ultrahigh pressure MICP tests were conducted by Moghaddam and Jamiolahmad (2016), who presented gamma distribution for the Barnett shale sample and normal distribution for the Eagle Ford shale and Pierre shale samples. Tian et al. (2017) put forward gamma distribution to analyze the effects of pore size distribution on gas apparent permeability.

Fractal theory is also incorporated to describe shale pore size distribution assuming that shale

reservoir follow statistically fractal scaling laws (Yu and Li, 2011). They introduced that the fractal objects always followed the scaling law:

$$X(L) \sim L^{D_f} \tag{2-16}$$

where X is the length or area or volume of an object; D_f is the fractal dimension, dimensionless; L is the range of length scale. Then the cumulative size distribution of pores and the total number of pores can be calculated as:

$$N(L \geq \omega) \sim \left(\frac{\omega_{max}}{\omega}\right)^{D_f} \tag{2-17}$$

$$N_t(L \geq \omega_{min}) \sim \left(\frac{\omega_{max}}{\omega_{min}}\right)^{D_f} \tag{2-18}$$

where ω is pore diameter, m; ω_{max} is the largest pore diameter, m; ω_{min} is the smallest pore diameter, m.

Yu and Li (2002) derived the fractal dimensions for multiphase flow (water phase and gas phase) on the basis of Equation (2-16):

$$D_{f,w} = d + \frac{\ln(S_w \phi)}{lnL} \tag{2-19}$$

$$D_{f,g} = d + \frac{\ln[(1-S_w)\phi]}{lnL} \tag{2-20}$$

where $D_{f,w}$ and $D_{f,g}$ are fractal dimension for water phase and gas phase, dimensionless.

2.8 Shale Gas Reservoir Simulation

Numerical simulation is frequently used to represent the complex flow in complicated geological structures to further predict and optimize shale gas production. Yu et al. (2017) adopted a complex hydraulic-fracture-propagation model representing complex fractures and a modified gas-diffusivity equation incorporating gas slippage, gas diffusion, and gas desorption to simulate gas

transport in shale reservoirs. The model was validated with field data and simulation work, forecasting gas cumulative production and calculating the contribution of all the mechanisms to gas production performance. A comprehensive model was derived by Yang et al. (2016) to analyze the involved gas transport mechanisms and the effects of fracture structures on gas production in shales with a complex non-planar fracture network. Zhao et al. (2018) simulated gas transport capacity with an analytical model considering slip flow, Knudsen diffusion surface diffusion, gas adsorption and a stress effect. The derived gas apparent permeability analytical model was then incorporated into reservoir simulation to simulate a gas production process. The mentioned research mainly focused on single gas phase flow to discover the importance of the involved gas transport mechanisms in shale gas reservoirs. Due to the co-existence of the water phase, relative permeability effect is also considered in numerous literature. Considering pressure dependent permeability and relative permeability effect, Novlesky et al. (2011) introduced shale gas modeling workflow for Nexen's Horn River reservoir with logarithmically spaced, locally refined, dual permeability (LS-LR-DK) methodology. Ali and Sheng (2015) evaluated the stress effect on permeability and gas production of Haynesville shale gas well with the local grid refinement (LGR) technique. Frantz et al. (2005) developed a Barnett shale gas production model for both vertical and horizontal wells with the incorporation of two phase flow, gas desorption and complex hydraulic fractures. Li et al. (2011) compared the differences of single porosity and dual porosity modelling approaches through an actual two phase flow shale gas model.

CHAPTER THREE: GAS TRANSPORT WITH MOBILE HIGH-VISCOSITY WATER FILM

3.1 Introduction

Gas flow behaviors in nanopores, especially in the vicinity of a wall, should be investigated as gas molecules movement properties in a limited space are different from the pattern of conventional flow. Consequently, the conventional pressure-driven flow equations should be modified to describe the deviation of shale gas flow. Also, the confined gas phase flow is liable to be affected by the occupied water molecules, leading to significant discrepancies between single gas flow and two-phase flow patterns. It has been discovered that different shale rock properties pose different effects on the two-phase flow. According to previous studies, water molecules tend to be arranged in an order at the hydrophilic solid substrate due the molecular forces at the interfacial area. Along with the increase in hydrophobicity of the wall, water molecules are likely to flow along the surface. Therefore, contact angle is introduced to capture the effects of solid properties on water true slip flow at the solid-water interface, which is further used to obtain the influences of water layers on gas flow capacity.

In this chapter, the properties and flow behaviors of water molecules in the vicinity of the solid surface are first investigated. Then an analytical model is put forward to calculate gas velocity profiles and predict a gas apparent permeability enhancement factor in shale nanometer scale characteristics of different geometries (slit pores and circular pores). Assuming that water saturation is low and all water molecules lie within the interaction range of solid surface, the proposed model considers the presence of a mobile high-viscosity water film through modified boundary conditions at a liquid-solid interface and a gas-liquid interface on the basis of the

governing equations for pressure-driven flow, finding good agreements with experimental data and confirming that a mobile high-viscosity water film enhances gas flow capacity. The importance of a mobile high-viscosity water film is further evaluated with varying pore sizes, pressures and surface wettability.

3.2 Model Establishment

Assuming a steady state and laminar flow, Myers (2011) provided potential reasons to the raised question of enhanced water flow in carbon nanotubes by a mathematical model composed of governing equations for a bulk water flow region with normal viscosity and an annular depletion region near a wall with reduced viscosity (Equation (2-12)). In this study, as shown in Figure 3-1, two divided flow regions, representing a gas flow region in the middle and a high-viscosity water film flow region at the wall separately, are assumed in slit pores and circular pores. It is also assumed that water saturation is low and water is reserved in the form of a high-viscosity water layer. Methane molecules dissolution in the water zone is ignored. Pressure driven flow equations and modified boundary conditions, which explain water true slip and gas slippage, are incorporated to obtain the analytical gas flow model with a mobile water film.

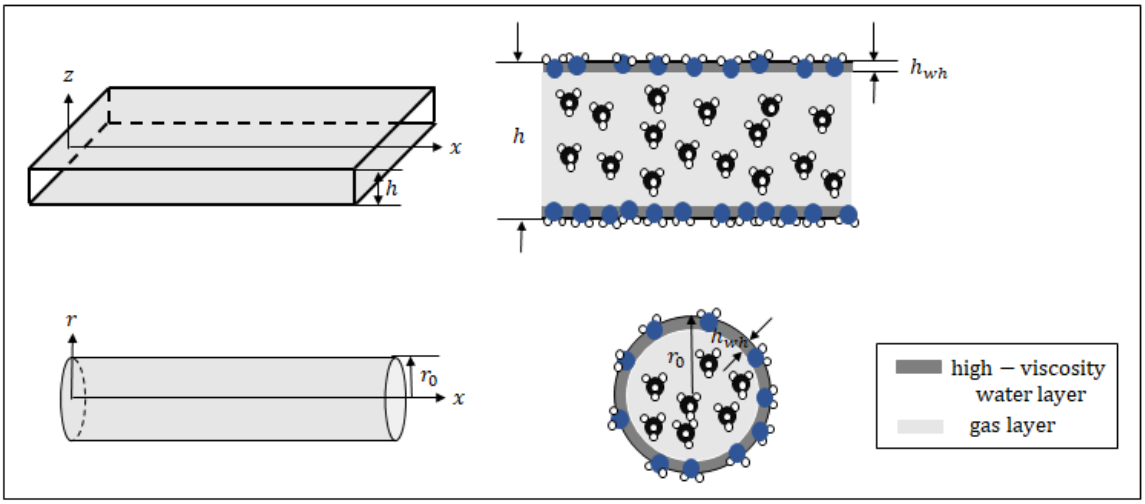

Figure 3-1 Schematic view of the model (high-viscosity water film).

3.2.1 Mobile High-Viscosity Water Film

The flow properties of confined water in nanopores, such as viscosity and slip along a boundary, are highly related to water-solid interactions and water intermolecular interactions. Compared with liquid-liquid attractions, relatively large liquid-solid attractions of a hydrophilic channel wall tends to result in the water molecules trapping in the pockets and crevices of the hydrophilic solid surface and an ordered arrangement of water molecules near the wall (Neto et al., 2005). In this way, the water viscosity in the corresponding region increases and multilayer sticking is achieved. On the contrary, if the solid becomes less hydrophilic, the water molecules initiate to move along the surface (Wu et al., 2017b). According to Majumder et al. (2005), this phenomenon could be attributed to the hydrogen bond between water molecules and water-solid attraction. Consequently, the properties of the liquid-solid interface, especially surface wettability and wall roughness, determine water slippage in nanopores significantly (Neto et al., 2005).

Mattia and Calabrò (2012) claimed that the work of adhesion W_A, which is the work required to separate liquid from a solid surface and create two new interfaces and obtained with the adsorbed vapour film pressure and contact angle, could be adopted to describe the liquid-solid molecular interactions per unit area. A larger W_A indicates a higher adhesion between two phases. In consequence, according to Mattia and Calabrò (2012), assuming that the film pressure of adsorbed vapour equals 19 mJ/m^2 and surface tension is 72 mN/m, $W_A$increases to 146 mJ/m^2 for the contact angle of 40 ^{o} and it drops to 96 mJ/m^2 when the contact angle is 86 ^{o}. Based on this theory and Equation (2-9) , the water slip length came out to be a function of the work of adhersion, surface diffusion, pore dimension and liquid viscosity near the wall (Equation (2-11)). With this equation, the effects of pore size and solid chemical properties on liquid slip can be estimated. Equation (2-11) tells that a solid surface with higher hydrophobicity tends to have smaller work of adhesion, which further promotes a larger water slip length. Huang et al. (2008) adopted MD simulations to study the water slippage at solid surfaces with different hydrophobicity, the contact angle of which was in the range of 0 ^{o} to 150 ^{o}. The water slip length, ranging from several nanometers to dozens of nanometers, has been found to be a function of the static contact angle representing the surface wettability (Equation (3-1)).

$$l_{ls} = C/(\cos\theta + 1)^2 \quad (3\text{-}1)$$

where l_{ls} is the true slip length, m; C is a constant, which is assigned to be 0.41, dimensionless. 0.41 is the value of C during the history match of the MD simulation data. The value changes to 6 for experimental data as the lab experiments are not able to achieve the ultra-smooth assumption (Wu et al., 2017b). Both Equations (2-11) and (3-1), which have been validated against experimental and simulation data, relate liquid slip length with contact angle.

Table 3-1 Water slip length comparison

Parameter	Literature enhancement factor, dimensionless	Slip length, m (Equation (2-8))	Slip length, m (Equation (2-11))	Slip length, m (Equation (3-1))
Whitby et al. (2008)	22 to 34	1.16×10^{-7} to 1.82×10^{-7}	2.29×10^{-8} to 8.83×10^{-8}	1.9237×10^{-9}
Majumder et al. (2005)	10,000 to 100,000	8.75×10^{-6} to 8.75×10^{-5}	2.44×10^{-7} to 1.84×10^{-6}	
Holt et al. (2006)	560 to 9,600	1.12×10^{-7} to 1.92×10^{-6}	4.04×10^{-8} to 1.23×10^{-7}	
Thomas and McGaughey (2009)	55 to 425	3.39×10^{-8} to 8.48×10^{-8}	3.80×10^{-9} to 8.18×10^{-9}	5.24×10^{-9}
Huang et al. (2008)				1.41×10^{-10} to 1.77×10^{-8}

Parameter	Tube radius, m	Tube length, m	Work of adhesion, J/m^2	Contact angle, degree
Whitby et al. (2008)	2.2×10^{-8}	7.8×10^{-5}	1.46×10^{-1}	40
Majumder et al. (2005)	3.5×10^{-9}	3.4×10^{-5}		
Holt et al. (2006)	8×10^{-10}	2×10^{-6}		
Thomas and McGaughey (2009)	2.5×10^{-9}	7.5×10^{-8}	9.6×10^{-2}	86
Huang et al. (2008)				45 to 148

To explore the water flow properties in carbon nanotubes, Thomas and McGaughey (2009) selected nanotubes with the lengths of 75 nm and 150 nm and diameters of 0.83 nm to 1.66 nm to measure a relationship between water structure and water flow with the MD simulation method. Majumder et al. (2005) designed pressure driven flow experiments with multi-walled carbon nanotubes and a polystyrene film. The unexpected high liquid velocity captured was ascribed to an ultra-frictionless wall. Holt et al. (2006) conducted water and gas flow experiments with micro-

fabricated membranes formed with a bundle of vertical double-walled nanotubes and multi-walled nanotubes. Both higher gas and water permeabilities were observed in comparison to theoretical values. Whitby et al. (2008) obtained experimental observations from the pressure-driven flow tests with decane, ethanol and water with 44 nm nanotubes and calculated slip length with Equation (2-8). With the published data of Thomas and McGaughey (2009), Majumder et al. (2005), Holt et al. (2006), Whitby et al. (2008) and Huang et al. (2008) (Table 3-1), the water slip length calculated with Equation (2-11) and (3-1) are listed in Table 3-1. There are various discrepancies between literature values and calculated values due to the assumption of the near-wall water viscosity and diffusion coefficients, which are likely to be different for different solid and liquid. As the published MD simulation data of Huang et al. (2008) presented the influences of contact angle ranging from 0 ^{o} to 150 ^{o}, Equation (3-1) is selected to calculate the slip length and introduce the effect of solid-liquid interactions.

It is quite obvious that the properties and structures of a solid substrate also change the confined water viscosity. Chen et al. (2008) conducted non-equilibrium MD simulation to observe the alteration of shear stress during nanoscale fluid flow at various tube size and flow rate. Besides the liquid slip length calculation, Thomas and McGaughey (2009) also put forward an equation to calculate the effective viscosity by area-weighted averaging. Zhang et al. (2011) tested confined water viscosity in single-walled carbon nanotubes with a diameter between 0.8 nm and 5.4 nm. The MD simulation results obtained through critical energy analysis were fitted successfully with an empirical equation as a function of pore size. Mentioning that the confined water viscosity was highly associated with the solid-liquid interactions, Wu et al. (2017b) fitted the dependence of

water viscosity in an interfacial area on the contact angle as follows, which has been validated against the data mentioned above:

$$\frac{\mu_{wh}}{\mu_{wb}} = -0.018\theta + 3.25 \quad (3\text{-}2)$$

where θ is the contact angle, degree; μ_{wb} is the bulk water viscosity, Pa·s; μ_{wh} is the water viscosity in the interface region, Pa·s. Note that μ_{wh} is assumed to be a constant by neglecting the variation of the water viscosity with the increasing distance away from a wall. Numerous MD simulations and experiments data suggest that the thickness of a high-viscosity water layer is 0.7 nm (Mashl et al., 2003; Qin et al., 2015; Neek-Amal et al., 2016). The calculation of contact angle refers to Appendix A.

In this research, under the assumption that the walls of nanopores are smooth and ignore the dissolved gas in water, the contact angle at the liquid-solid interface reflects the relationship between water-wall interactions and water intermolecular interactions, and, therefore, can be used to measure the water rheological properties and boundary conditions in the interfacial region (Wu et al., 2017b). A small contact angle indicates a high solid attraction for water molecules to overcome in order to move along the surface (Neto et al., 2005).

3.2.2 Gas Slippage and Properties

As for the gas slippage, Zhang et al. (2017) assumed similar gas molecules behaviors at a gas-water interface and introduced the slip velocity to describe the gas-water momentum transport controlled by gas-liquid interactions and gas intermolecular interactions, which results in (Karniadakis et al., 2002):

$$\begin{cases} v_{gs} = \frac{2-\sigma_v}{\sigma_v}\frac{\lambda}{1-b\lambda}\left(\frac{\partial v_g}{\partial z}\right) \text{ for slit pores} \\ v_{gs} = \frac{2-\sigma_v}{\sigma_v}\frac{\lambda}{1-b\lambda}\left(\frac{\partial v_g}{\partial r}\right) \text{ for circular pores} \end{cases} \tag{3-3}$$

where v_{gs} is the gas slip velocity, m/s; σ_v is the tangential momentum accommodation coefficient, dimensionless; b is a slip coefficient, dimensionless; v_g is the gas velocity in nanopores with a mobile high-viscosity water film, m/s; λ is the mean free path, m, which can be defined as:

$$\lambda = \frac{\mu_g}{P}\sqrt{\frac{\pi ZRT}{2M_g}} \tag{3-4}$$

where R is the gas constant, equaling to 8.314 J/(K·mol); M_g is the gas molecular weight, kg/mol; μ_g is the gas viscosity, Pa·s; P is the pressure, Pa; T is the temperature, K; Z is the gas compressibility factor, dimensionless, which is calculated as (Wu et al., 2017a):

$$Z = 0.702(\frac{P}{P_c})^2 e^{-2.5T/T_c} - 5.524\left(\frac{P}{P_c}\right)e^{-\frac{2.5T}{T_c}} + 0.044\left(\frac{T}{T_c}\right)^2 - 0.164\frac{T}{T_c} + 1.15 \tag{3-5}$$

where P_c is the critical pressure, Pa; T_c is the critical temperature, K.

The gas viscosity (μ_g) can be obtained as follows (Jarrahian and Heidaryan, 2014):

$$\mu_g = \mu_{g0}[1 + \frac{o_1}{{T_r}^5}\left(\frac{{P_r}^4}{{T_r}^{20}+{P_r}^4}\right) + o_2\left(\frac{P_r}{T_r}\right)^2 + o_3(\frac{P_r}{T_r})] \tag{3-6}$$

where μ_{g0} is the gas viscosity at $P = 1.01325 \times 10^5$ Pa and $T = 423$ K; P_r is the reduced pressure, dimensionless, equaling to the ratio of pressure and the critical pressure; o_1, o_2 and o_3 are the fitting coefficients, dimensionless.

3.2.3 Slit Pores with Mobile High-Viscosity Water Film

Considering the equilibrium distribution of a high-viscosity water film with a uniform thickness h_{wh} on the inner surface of a slit pore with a height of h as shown in Figure 3-1, the corresponding expressions for velocities in the gas region and the water region are (Bruus, 2008):

$$\begin{cases} \frac{\partial^2 v_g}{\partial z^2} = -\frac{\Delta P}{\mu_g L}, z \in [0, \frac{h}{2} - h_{wh}\,] \\ \frac{\partial^2 v_{wh}}{\partial z^2} = -\frac{\Delta P}{\mu_{wh} L}, z \in [\frac{h}{2} - h_{wh}\,, \frac{h}{2}] \end{cases} \tag{3-7}$$

where ΔP is an applied pressure difference between the entrance and exit, Pa; L is the length of the pore model, m; v_g is the gas velocity, m/s; v_{wh} is the water velocity, m/s; h is the height of the slit pore, m; h_{wh} is the thickness of the water layer, m, whose value is assigned as 0.7 nm.

According to the previous discussion, non-slip boundaries are modified to explain water true slip and gas slippage by introducing the true slip length l_{ls} and gas slip velocity v_{gs}. The corresponding boundary conditions to preserve velocity and shear stress continuity can be described as (Bruus, 2008; Myers, 2011):

$$\begin{cases} \left(\frac{\partial v_g}{\partial z}\right)|_{z=0} = 0 \\ v_{wh}|_{z=\frac{h}{2}} = -l_{ls} \frac{\partial v_{wh}}{\partial z}|_{z=\frac{h}{2}} \\ \mu_g \left(\frac{\partial v_g}{\partial z}\right)|_{z=\frac{h}{2}-h_{wh}} = \mu_{wh} \left(\frac{\partial v_{wh}}{\partial z}\right)|_{z=\frac{h}{2}-h_{wh}} \\ v_g|_{z=\frac{h}{2}-h_{wh}} = v_{wh}|_{z=\frac{h}{2}-h_{wh}} - v_{gs}|_{z=\frac{h}{2}-h_{wh}} \end{cases} \tag{3-8}$$

Let z_D be the dimensionless height, that is, $z_D = z/(\frac{h}{2})$. The gas velocity profile satisfying the boundary conditions in Equation (3-8) is deduced as:

$$\begin{cases} v_g = \frac{\Delta P}{L}\left[-\frac{(z_D h)^2}{8\mu_g} + \frac{(h-2h_{wh})^2}{8\mu_g} - \frac{(h-2h_{wh})^2}{8\mu_{wh}} + \frac{h^2}{8\mu_{wh}} + \frac{l_{ls}h}{2\mu_{wh}} + \frac{2-\sigma_v}{\sigma_v}\frac{\lambda}{1-b\lambda}\frac{(h-2h_{wh})}{2\mu_g}\right] \\ v_{wh} = \frac{\Delta P}{L}\left[-\frac{(z_D h)^2}{8\mu_{wh}} + \frac{h^2}{8\mu_{wh}} + \frac{l_{ls}h}{2\mu_{wh}}\right] \end{cases} \tag{3-9}$$

A gas flow rate equation can be further calculated through the integration of Equation (3-9) along the z axis:

$$\begin{cases} Q_g = \frac{2\Delta PW}{3\mu_g L}\left(\frac{h}{2} - h_{wh}\right)^3 + \frac{\Delta PW}{\mu_{wh} L}\left(\frac{h}{2} - h_{wh}\right)\left(l_{ls}h - {h_{wh}}^2 + hh_{wh}\right) + \frac{2-\sigma_v}{\sigma_v}\frac{2\lambda}{1-b\lambda}\frac{\Delta PW}{\mu_g L}\left(\frac{h}{2} - h_{wh}\right)^2 \\ Q_{wh} = \frac{\Delta PW}{\mu_{wh} L}\left(\frac{h{h_{wh}}^2}{2} - \frac{{h_{wh}}^3}{3} + l_{ls}hh_{wh}\right) \end{cases} \tag{3-10}$$

where Q_g is the volumetric rate of gas flow in nanopores with the mobile high-viscosity water film, m^3/s; Q_{wh} is the volumetric rate of water flow in nanopores with the mobile high-viscosity water film, m^3/s; W is the width of a slit pore, m.

In the case of Darcy's equation, the gas flow rate Q_{gd} takes the following form:

$$Q_{gd} = \frac{K_g(h-2h_{wh})W}{\mu_g}\frac{\Delta P}{L} \tag{3-11}$$

The ratio of porosity to tortuosity is applied to correct the flow rate in porous media, where the tortuosity is the ratio of the average actual path length to the straight-line distance in pores. If the water occupied space and pore tortuosity τ are taken into account, one obtains:

$$Q_{gd} = \frac{\phi_g}{\tau} Q_g \tag{3-12}$$

where ϕ_g is the porosity occupied by gas, taking $(1 - 2h_{wh}/h)\phi$ for slit pores and $(r_0 - h_{wh})^2\phi/{r_0}^2$ for circular pores, dimensionless.

Substitution of Equations (3-11) and (3-12) into Equation (3-10) results in the following equation for the determination of gas apparent permeability:

$$K_g = \frac{\phi_g}{\tau}\left[\frac{1}{3}\left(\frac{h}{2} - h_{wh}\right)^2 + \frac{\mu_g}{2\mu_{wh}}\left(l_{ls}h - {h_{wh}}^2 + hh_{wh}\right) + \frac{2-\sigma_v}{\sigma_v}\frac{\lambda}{1-b\lambda}\left(\frac{h}{2} - h_{wh}\right)\right] \quad (3\text{-}13)$$

where K_g is the gas apparent permeability in nanopores with a mobile high-viscosity water film, m^2.

Neglecting the mobility of the high-viscosity water film in the boundary conditions above yields Equation (3-14):

$$\begin{cases} \left(\frac{\partial v_g}{\partial z}\right)|_{z=0} = 0 \\ v_g|_{z=\frac{h}{2}-h_{wh}} = -v_{gs}|_{z=\frac{h}{2}-h_{wh}} \end{cases} \quad (3\text{-}14)$$

Following the same procedure in the case of the mobile water film, the gas velocity profile and gas apparent permeability equations when the water film loses its mobility can be derived as:

$$v_{gi} = \frac{\Delta P}{\mu_g L}\left[-\frac{(z_D h)^2}{8\mu_g} + \frac{(h-2h_{wh})^2}{8\mu_g} + \frac{2-\sigma_v}{\sigma_v}\frac{\lambda}{1-b\lambda}\frac{(h-2h_{wh})}{2\mu_g}\right] \quad (3\text{-}15)$$

$$K_{gi} = \frac{\phi_g}{\tau}\left[\frac{1}{3}\left(\frac{h}{2} - h_{wh}\right)^2 + \frac{2-\sigma_v}{\sigma_v}\frac{\lambda}{1-b\lambda}\left(\frac{h}{2} - h_{wh}\right)\right] \quad (3\text{-}16)$$

where v_{gi} is the gas velocity in nanopores with a static high-viscosity water film, m/s; K_{gi} is the gas apparent permeability in nanopores with a static high-viscosity water film, m^2.

3.2.4 Circular Pores with Mobile High-Viscosity Water Film

The gas transport behaviors in circular pores will now be considered. The flow governing equations for gas and water in this case are (Bruus, 2008):

$$\begin{cases} \frac{\mu_g}{r}\frac{\partial}{\partial \mathrm{r}}\left(r\frac{\partial v_g}{\partial r}\right) = \frac{\partial P}{\partial x}, r \in [0, r_0 - h_{wh}] \\ \frac{\mu_{wh}}{r}\frac{\partial}{\partial \mathrm{r}}\left(r\frac{\partial v_{wh}}{\partial r}\right) = \frac{\partial P}{\partial x}, r \in [r_0 - h_{wh}, r_0] \end{cases} \tag{3-17}$$

where r_0 is the pore radius, m.

With the boundary conditions listed in Equation (3-18), similar to the previous case, it can be shown that the determination of the gas velocity profile with regard to curved surfaces is given by Equation (3-19):

$$\begin{cases} \left(\frac{\partial v_g}{\partial r}\right)|_{r=0} = 0 \\ v_{wh}|_{r=r_0} = -l_{ls}\frac{\partial v_{wh}}{\partial r}|_{r=r_0} \\ \mu_g\left(\frac{\partial v_g}{\partial r}\right)|_{r=r_0-h_{wh}} = \mu_{wh}\left(\frac{\partial v_{wh}}{\partial r}\right)|_{r=r_0-h_{wh}} \\ v_g|_{r=r_0-h_{wh}} = v_{wh}|_{r=r_0-h_{wh}} - v_{gs}|_{r=r_0-h_{wh}} \end{cases} \tag{3-18}$$

$$\begin{cases} v_g = -\frac{\Delta P {r_0}^2}{4\mu_g L}{r_D}^2 + \frac{\Delta P}{4\mu_g L}(r_0 - h_{wh})^2 + \frac{\Delta P h_{wh}}{4\mu_{wh} L}(2r_0 - h_{wh}) + l_{ls}\frac{\Delta P}{2\mu_{wh} L}r_0 + \frac{2-\sigma_v}{\sigma_v}\frac{\lambda}{1-b\lambda}\frac{\Delta P}{2\mu_g L}(r_0 - h_{wh}) \\ v_{wh} = -\frac{\Delta P {r_0}^2}{4\mu_{wh} L}{r_D}^2 + l_{ls}\frac{\Delta P}{2\mu_{wh} L}r_0 + \frac{\Delta P}{4\mu_{wh} L}{r_0}^2 \end{cases} \tag{3-19}$$

where r_D is the dimensionless radius, which is defined as $r_D = r/r_0$.

Finally, the gas apparent permeability equation can be obtained through the integration of Equation (3-19) and a further replacement of Equation (3-12):

$$K_g = \frac{\phi_g}{\tau}\left[\frac{(r_0 - h_{wh})^2}{8} + \frac{\mu_g}{4\mu_{wh}}\left(2r_0 h_{wh} - {h_{wh}}^2 + 2l_{ls}r_0\right) + \frac{2-\sigma_v}{\sigma_v}\frac{\lambda}{1-b\lambda}\frac{(r_0 - h_{wh})}{2}\right] \tag{3-20}$$

If the contribution of water molecules sliding along a substrate is ignored, then

$$v_{gi} = -\frac{\Delta P {r_0}^2}{4\mu_g L}{r_D}^2 + \frac{\Delta P}{4\mu_g L}(r_0 - h_{wh})^2 + \frac{2-\sigma_v}{\sigma_v}\frac{\lambda}{1-b\lambda}\frac{\Delta P}{2\mu_g L}(r_0 - h_{wh}) \tag{3-21}$$

$$K_{gi} = \frac{\phi_g}{\tau}\left[\frac{(r_0 - h_{wh})^2}{8} + \frac{2-\sigma_v}{\sigma_v}\frac{\lambda}{1-b\lambda}\frac{(r_0 - h_{wh})}{2}\right] \quad (3\text{-}22)$$

3.3 Model Validation

To achieve a general relationship between shale permeability and reservoir pressure, Rutter et al. (2015) collected core samples with a diameter of 22.5 mm and a length of 22.5 mm and recorded permeability over the whole range of reservoir pressure. The collected samples have been heated at 60 ^{o}C to remove initial water and guarantee a dry condition (Rutter et al., 2015). Figure 3-2(a) compares the experimentally measured permeability with the permeability estimated by the proposed model under the assumption that h_w equals 0 nm. To measure the difference between the fitting results and the measured data, R^2 for this validation is calculated to be 0.70. Another validation is carried out between the proposed model and dry specimens from Mimms Creek Field with a diameter of 25.58 mm and a length of 52.6 mm, whose gas apparent permeability were measured at pressure differentials of 10, 100, 500, 1000 and 2000 psi to explore the two phase gas slippage effects (Rushing et al., 2003). According to Fig. 3-3(b), R^2 for the fitting is 0.97, proving that the proposed model gives results consistent with the experiment data in terms of a dry condition.

Simultaneously, the relationship between shale permeability and reservoir pressure in a wet condition is validated in Figures 3-2(c) to 3-2(e). Wu et al. (2014) observed gas-water flow behaviors and analyzed the effects of water saturation with the laboratory-on-chip approach. They collected numerous experimental data over a wide range of pressure and water saturation. Pure nitrogen was used as gas phase and pure water was used as water phase. The pressure drop was recorded with pressure tensors and gas flow rate was determined by measuring the movement of

gas slug. Gas permeability can be calculated with the obtained pressure drops and flow rates. Figures 3-2(c) and 3-2(d) present good agreements between their results and the provided mathematical model with R^2 to be 0.98 and 0.97 at different water saturation. Wet specimens from Mimms Creek Field mentioned above are also used to validate the proposed model, the R^2 of which turns out to be 0.84. It can be concluded that the validity of the proposed model has been confirmed, with which the gas transport phenomenon can be captured with the accuracy needed in engineering applications.

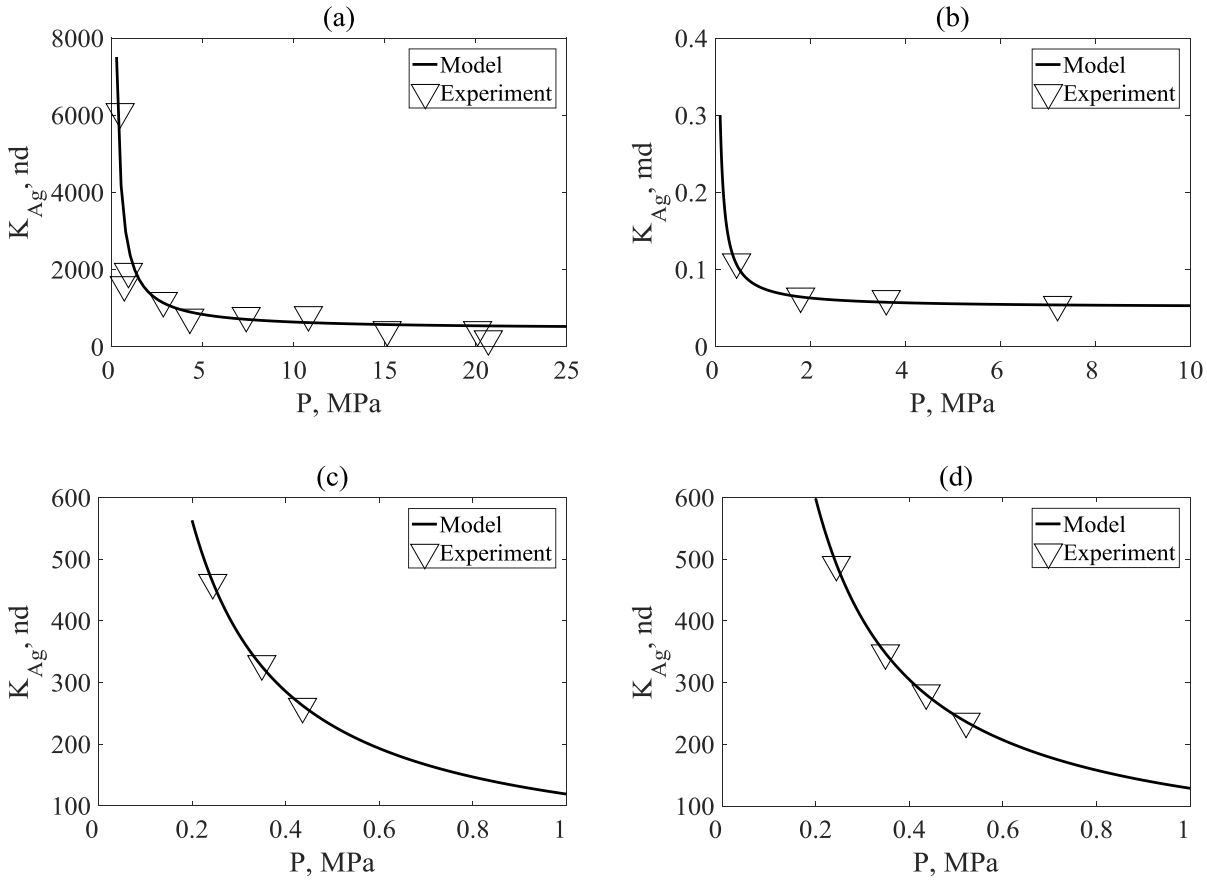

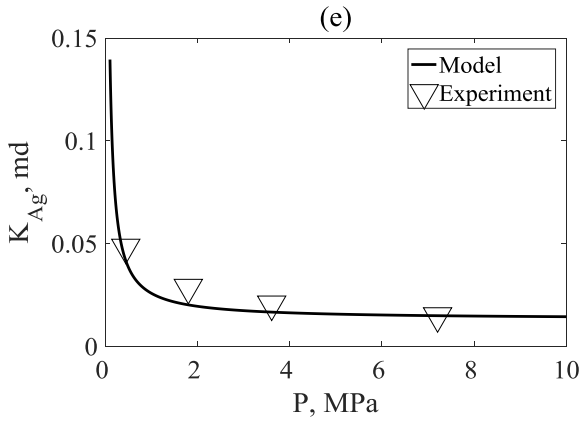

Figure 3-2 (a) Validation of gas apparent permeability with experimental data of dry shale sample reported by Rutter et al. (2015), $L = 22.5\,mm$, $h = 100\,nm$, $T = 300\,K$, $\phi = 0.09$, $\theta = 30°$, and $h_w = 0\,nm$; (b) validation of gas apparent permeability with experimental data of dry shale sample reported by Rushing et al. (2003), $L = 52.6\,mm$, $h = 104\,nm$, $T = 273.15\,K$, $\phi = 0.094$, $\theta = 30°$, and $h_w = 0\,nm$; (c) validation of gas apparent permeability with experimental data of wet shale sample reported by Wu et al. (2014), $h = 3.3\,nm$, $T = 273.15\,K$, $\phi = 0.09$, $\theta = 30°$, and $h_w = 0.7\,nm$; (d) validation of gas apparent permeability with experimental data of wet shale sample reported by Wu et al. (2014), $h = 4.7\,nm$, $T = 273.15\,K$, $\phi = 0.09$, $\theta = 30°$, and $h_w = 0.7\,nm$; (e) validation of gas apparent permeability with experimental data of wet shale sample reported by Rushing et al. (2003), $L = 52.6\,mm$, $h = 54\,nm$, $T = 273.15\,K$, $\phi = 0.094$, $\theta = 30°$, and $h_w = 0.7\,nm$.

3.4 Results and Discussion

3.4.1 Velocity Profile

The presence of a mobile high-viscosity water film occupies the gas flow cross-section and provides molecular interactions at the interface, thereby bringing about effects on gas velocity profiles in nanoscale tubes. Figures 3-3(a) to 3-3(c) predict gas flow patterns with a mobile water

film and a static water film in nanotubes measuring 3 nm, 6 nm and 12 nm separately. In all the three figures, the solid line refers to the case with the mobile water film while the dash line reflects the situation in which the water film remains static. The unfit for the calculated velocity is m/s per Pa/m. Figures 3-3(a) to 3-3(c) clarify how high-viscosity water film and gas slippage contribute to gas flow velocity. To distinguish the discrepancy between the two cases, Figure 3-3(d) calculates the relative difference for all the mentioned pore radii. Generally, whether the water film is mobile or not, the gas velocity resembles a parabolic shape and the gas front at the centerline achieves the highest flow rate. It is further noticed that the mobile high-viscosity water film enhances the gas velocity and reduces gas flow resistance to varying degrees for the whole range of pore cross section. The reason is that, at the liquid-solid contact region, water phase gains an extra flow velocity though liquid slip, which is not quite obvious for the inorganic pores in this example. For Figure 3-3(a), the hydrophilic surface only provides 0.12 nm liquid slip length and consequently 1.76×10^{-15} m/s water flow velocity at the solid wall. Besides, in contrast to the static water molecules, the mobile water film leads to a higher gas velocity at the boundary, which is conducive to generate an increase in gas transport capacity. For instance, for the pore size of 3 nm, the mobile water velocity achieves 1.30×10^{-14} m/s at the water-gas interface. In consequence, the gas velocity interceptions at the water-gas interface are 1.08×10^{-13} m/s and 9.47×10^{-14} m/s corresponding to the cases of the mobile water film and the static water film (Figure 3-3(a)). Figure 3-3(d) reinforces this conclusion and further reveals that the relative difference increases from 6.28% to 9.08% with the increasing distance away from the centerline in the case of the 3 nm sized pore, indicating that the gas transport at the gas zone boundary is the most sensitive to the mobility of a high-viscosity water film due to the water-gas molecular interactions at the interface. The contrast of Figure 3-3(a) with Figures 3-3(b) and 3-4(c) tells that a larger pore dimension leads to increases in both

water velocity and gas velocity. The water velocity is 7.06×10^{-15} m/s and 1.87×10^{-13} m/s at the two interfaces separately in the 12 nm sized nanopore, producing a minimum gas velocity at 8.14×10^{-13} m/s. Also, comparing Figures 3-3(a) to 3-3(c) comes with another conclusion that the difference brought about by the mobile water film is even larger with a reduction in the pore size. Figure 3-3(d) displays that the relative differences in gas flow profiles at the centerline are as large as 6.28%, 3.06% and 1.58% in turn, demonstrating that gas flow behaviors in large pores are less affected by the mobile water film. This is because gas transport can be affected by gas slippage in control of the molecule-wall collisions, which are less dominant compared with intermolecular collisions provided with a larger pore height. Also, the given contribution of mobile water molecules is less significant compared to the increasing share of gas movement in a larger flow area. Figure 3-3(e) provides single gas phase flow velocity profile as a comparison. It is quite obvious that the existence of water molecules occupies gas flow channel and brings about the drop of gas flow capacity, which far outweighs the positive effect of mobile water molecules.

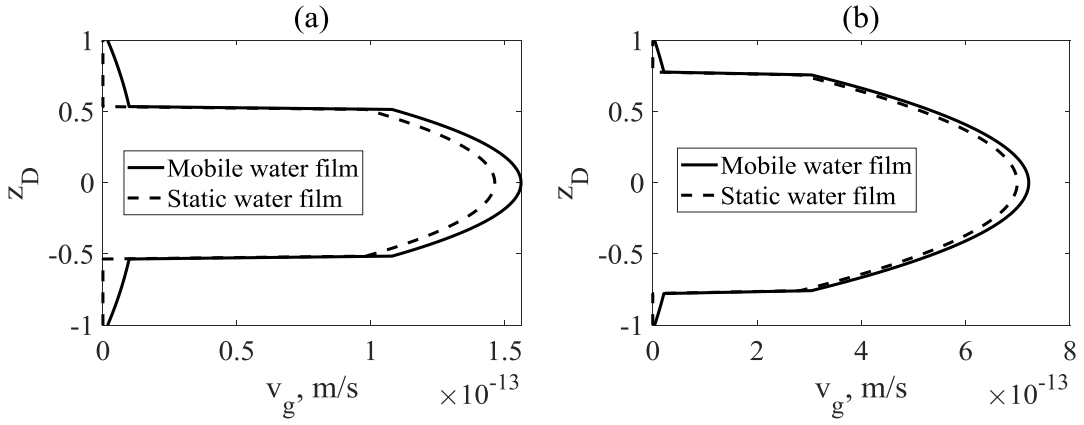

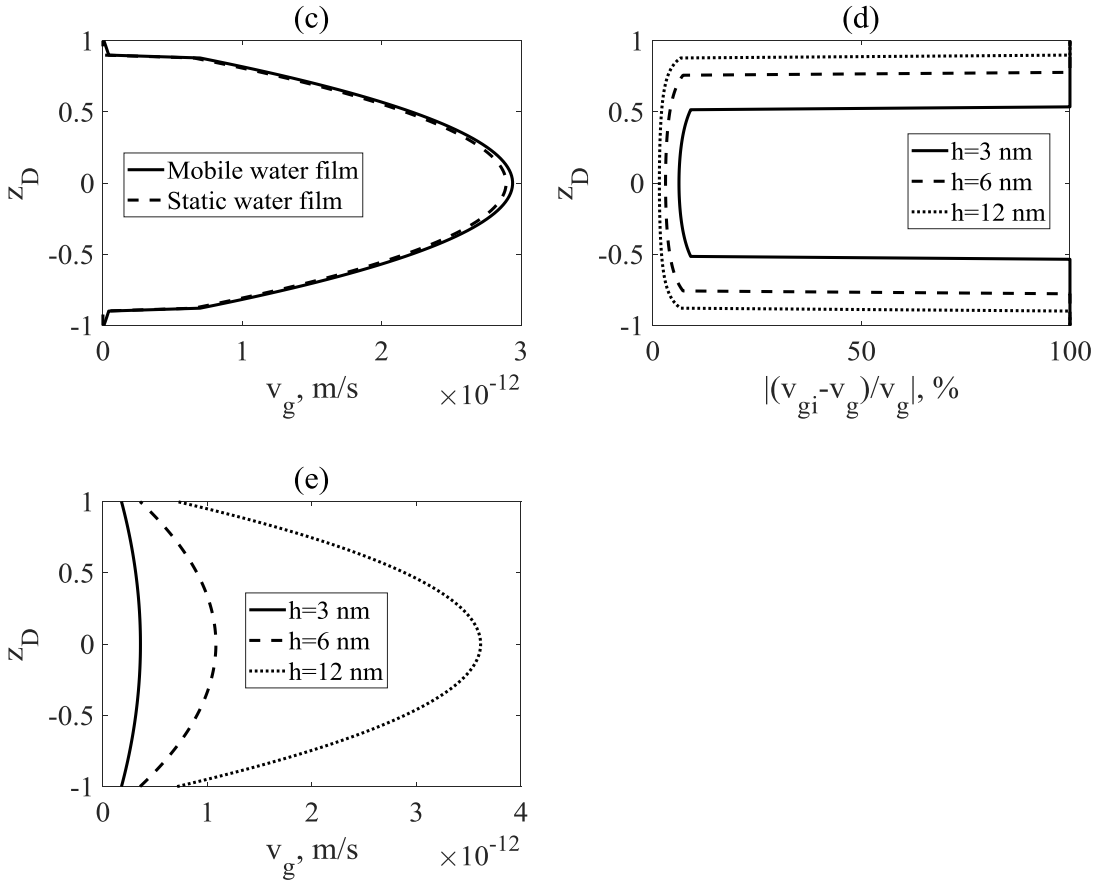

Figure 3-3 (a) Gas velocity profile at $h = 3\,nm$; (b) gas velocity profile at $h = 6\,nm$; (c) gas velocity profile at $h = 12\,nm$; (d) relative difference between the gas velocity with mobile water film and that with static water film at different pore sizes of 3 nm, 6 nm and 12 nm. $P = 50\,MPa$, $T = 350\,K$, $\phi = 0.09$, $\theta = 30°$, $h_w = 0.7\,nm$; (e) Gas velocity profile without water layer at different pore sizes of 3 nm, 6 nm and 12 nm. $P = 50\,MPa$, $T = 350\,K$, $\phi = 0.09$.

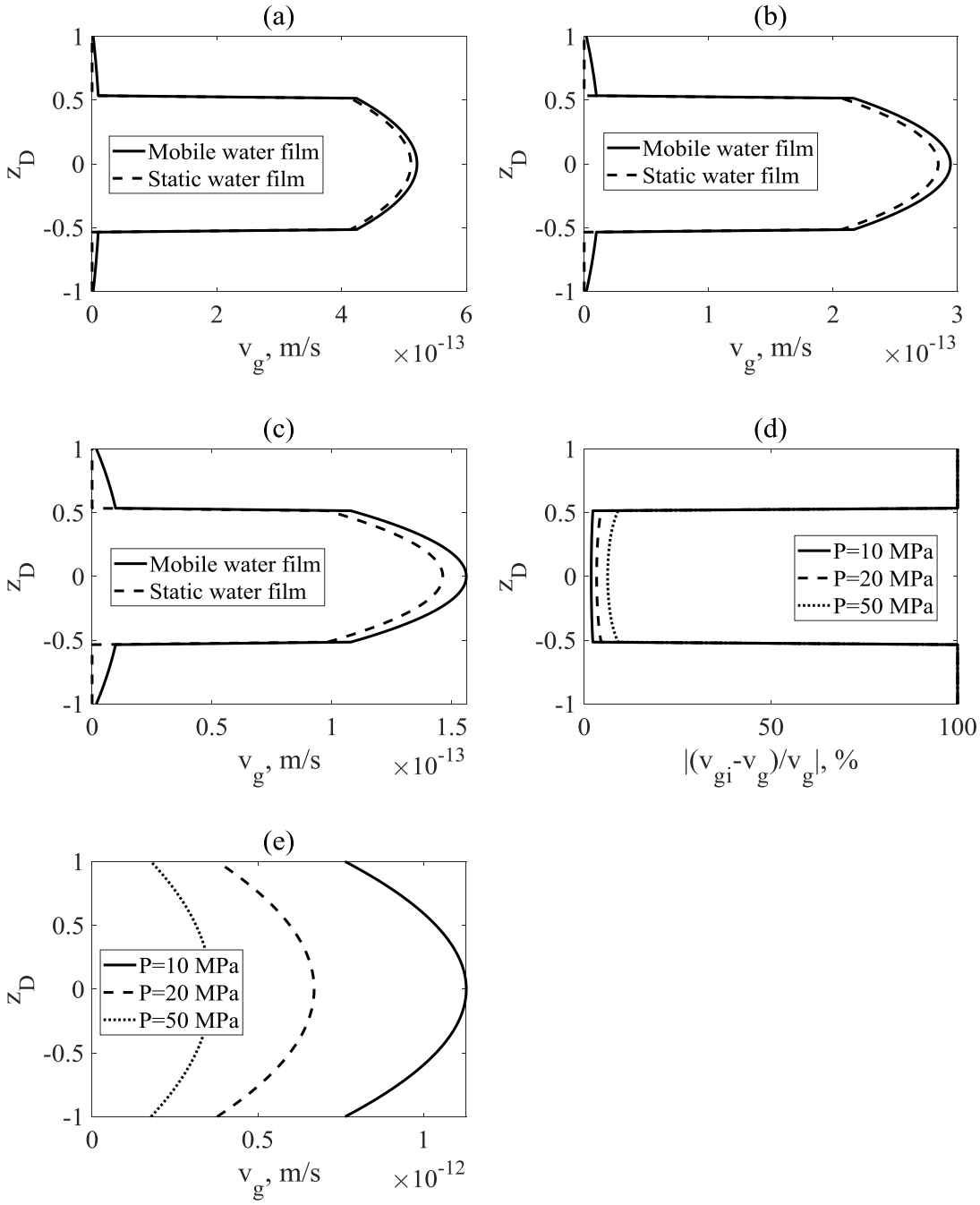

Figure 3-4 (a) Gas velocity profile at $P = 10\ MPa$; (b) gas velocity profile at $P = 20\ MPa$; (c) gas velocity profile at $P = 50\ MPa$; (d) relative difference between the gas velocity with mobile water film and that with static water film at different pressure of $10\ MPa$, $20\ MPa$ and $50\ MPa$. $h = 3\ nm$, $T = 350\ K$, $\phi = 0.09$, $\theta = 30°$, $h_w = 0.7\ nm$; (e) Gas velocity profile without water

layer at different pressure of 10 MPa, 20 MPa and 50 MPa. $h = 3\ nm$, $T = 350\ K$, $\phi = 0.09$.

Figures 3-4(a) to 3-4(c) put a particular emphasis on the impacts of pressure. The boundary gas velocities with a mobile water film reach 4.20×10^{-13} m/s, 2.14×10^{-13} m/s and 1.08×10^{-13} m/s at the pressure of 10 MPa, 20 MPa and 50 MPa, respectively. A smaller gas velocity not only comes from a higher gas viscosity but also from a shorter gas mean free path at a higher pressure. Also, it is obvious that, given a larger pressure (from 10 MPa to 50 MPa), the relative difference increases from 2.31% to 9.08% at the boundary, which is potentially attributed to an increasing influences of the gas velocity caused by the mobile water film as the gas velocity is smaller at larger pressure while the water velocity remains relatively unchanged (Figure 3-4(d)). Figure 3-4(e) also serves as a contrast to depict the flow pattern of single gas phase.

3.4.2 Gas Transport Capacity

Figures 3-3 and 3-4 prove that the existence of a mobile higher-viscosity water film contributes to a larger gas velocity, and the gas transport capacity tends to be enhanced in this way. The gas apparent permeability enhancement factor ϵ, defined as the ratio of K_g to K_{gi}, is proposed to evaluate the enhanced gas transport capacity. Consistent with the previous discussion, Figures 3-5(a) and 3-5(b) indicate that the gas transport efficiency is likely to be underestimated without the mobile water film as ϵ is always larger than 1. The enhancement factors are 1.0464, 1.0255, 1.0030 and 1.0003 when the pore heights are 5 nm, 10 nm, 100 nm and 1000 nm under the pressure of 50 MPa, respectively, following the same pattern as in Figure 3-3 and confirming that the positive impact of the mobile water film reduces with a larger pore dimension (Figure 3-5(a)). According to Figure 3-5(b), when the pressure is assigned with 0.1 MPa, 1 MPa, 10 MPa and 50 MPa, the

enhancement factors turn out to be 1.0002, 1.0023, 1.0206 and 1.0759, respectively, providing more evidence to support the previous opinion that the contribution of the mobile water film on gas flow capacity increases with an increasing pressure. In view of the analysis above, the smaller the pore is and the larger the pressure is, the larger positive effect is imposed on the gas flow behaviors by the mobile water film. Considering the nanoscale pore size (1-100 nm) and high-pressure reservoir condition (>10 MPa) for a shale gas reservoir, there is a need to take the mobile high-viscosity water film into account.

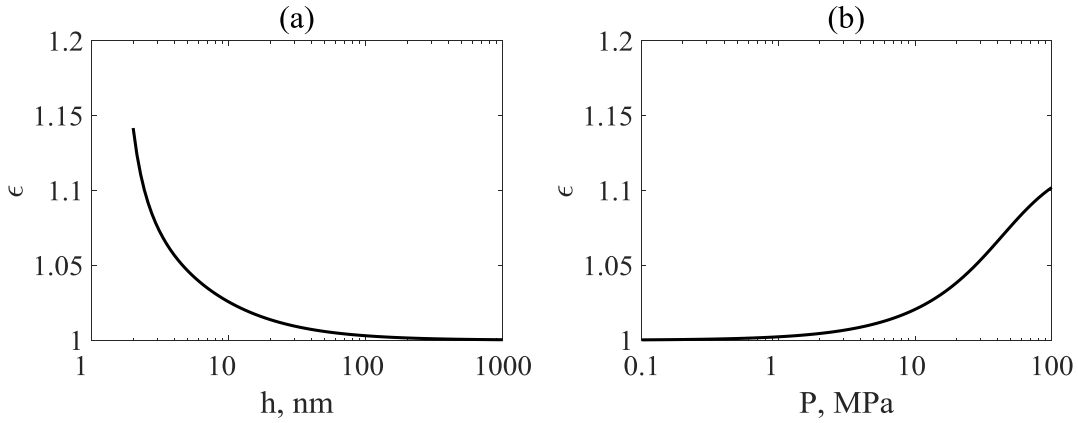

Figure 3-5 (a) Relationship between the enhancement factor of gas apparent permeability and pore size, $P = 50\ MPa$; (b) relationship between the enhancement factor of gas apparent permeability and pressure, $h = 3\ nm$. $T = 350\ K$, $\phi = 0.09$, $\theta = 30°$, $h_w = 0.7\ nm$.

3.4.3 Surface Wettability Effect

Figure 3-6 shows the dependence of the velocity profile on surface wettability. In particular, the gas velocity at the centerline is 1.56×10^{-13} m/s when the contact angle at the water-wall surface is 30 °. Once the water-solid molecular attractions get weaker, the contact angle turns larger, leading to fewer ordered water molecules and a lower water viscosity. Water velocity at the solid surface increases from 1.76×10^{-15} m/s to 3.41×10^{-15} m/s and 1.02×10^{-14} m/s in turn. Figure 3-6(a)

demonstrates that hydrophobic surface generates larger water slippage and smaller water viscosity near the wall. In this way, the higher mobility of the water film accelerates the gas velocity at the gas-water interface. Increasing the contact angle to 60 º and 90 º leads to an increase in the gas velocity to 1.60×10^{-13} m/s and 1.70×10^{-13} m/s respectively, at the centerline (Figure 3-6(a)). Figure 3-6(b) describes the slope of the gas velocity against the contact angle ranging from 30 º to 90 º, clarifying that strong hydrophilicity has a negative effect on enhancing the gas flow rate.

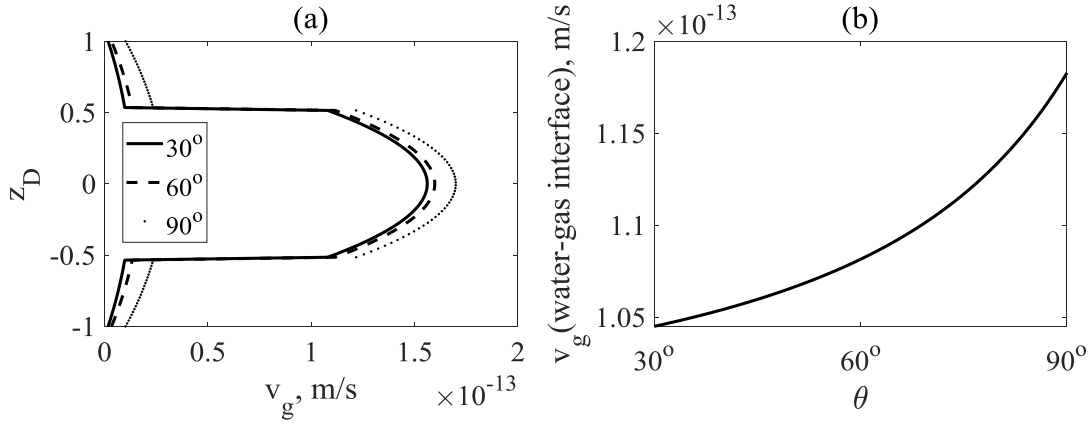

Figure 3-6 (a) Gas velocity profile at contact angles of 30°, 60°, 90°; (b) relationship between gas velocity and contact angle. $P = 50\ MPa$, $h = 3\ nm$. $T = 350\ K$, $\phi = 0.09$, $h_w = 0.7\ nm$.

Figure 3-7(a) assists to accurately capture how a gas apparent permeability enhancement factor changes with the contact angle. Furthermore, $d(\epsilon)/d(\theta)$ is calculated in differently sized pores to measure the influences of confinement (Figure 3-7(b)). Reconcile to the trend of Figure 3-3(d) in which the gas velocity is less affected in larger pores for a given mobility of the water film, ϵ is more sensitive to the contact angle in smaller pores. Likewise, Figure 3-7(c) indicates that a larger pressure results in higher sensitivity of gas transport capacity to surface wettability in accordance with Figure 3-4(d), verifying the fact that the gas velocity is more sensitive to a mobile water film under a higher pressure.

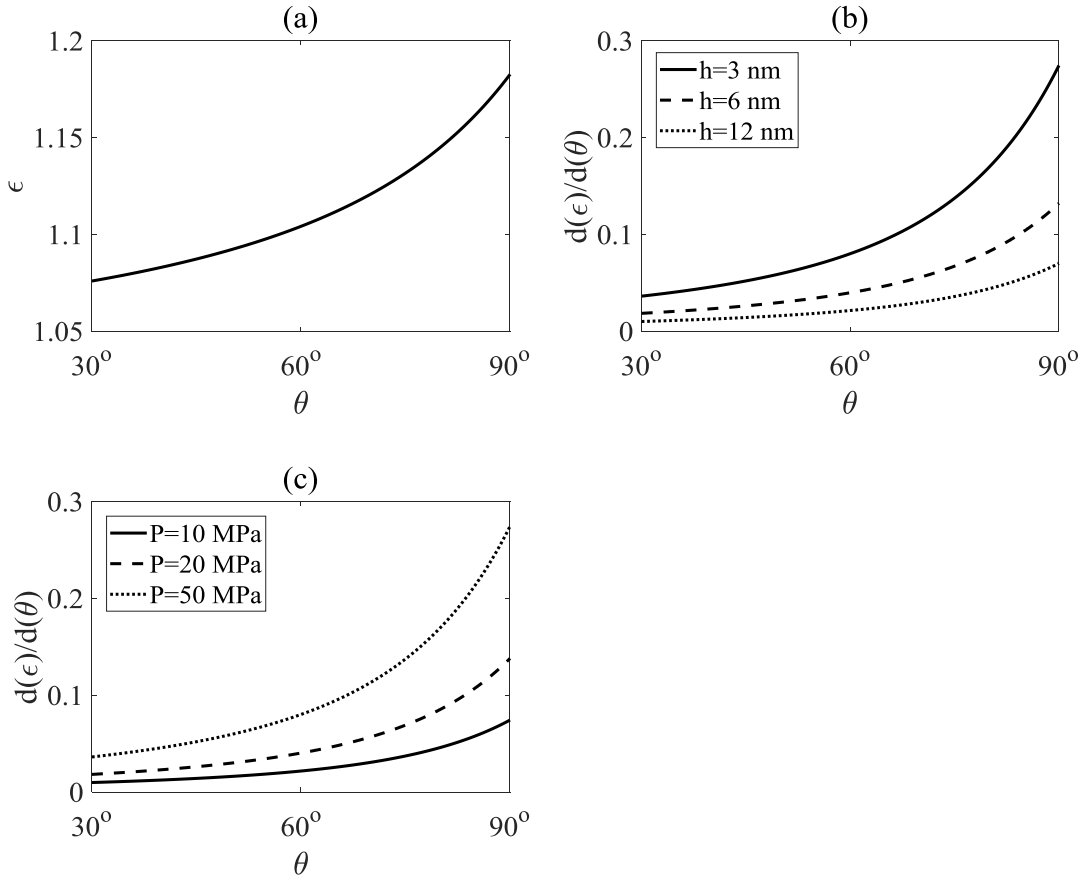

Figure 3-7 (a) Relationship between enhancement factor of the gas apparent permeability and the contact angle for the case of $P = 50\ MPa$ and $h = 3\ nm$; (b) relationship bewteen $d(\epsilon)/d(\theta)$ and contact angle at different pore sizes of 3 nm, 6 nm and 12 nm, $P = 50\ MPa$; (c) relationship bewteen $d(\epsilon)/d(\theta)$ and contact angle at different pressure of $10\ MPa$, $20\ MPa$ and $50\ MPa$, $h = 3\ nm$, $P = 50\ MPa$, $T = 350\ K$, $\phi = 0.09$, $h_w = 0.7\ nm$.

Figure 3-8 plots the two extreme situations when the solid surfaces are particular hydrophilic and hydrophobic. It can be seen that there tends to be an almost static or slow-moving water film surrounding the gas phase for the hydrophilic pores. In contrast, the velocity difference between gas phase and water phase is only 0.14% in the case of hydrophobic pores according to Figure 3-8(b).

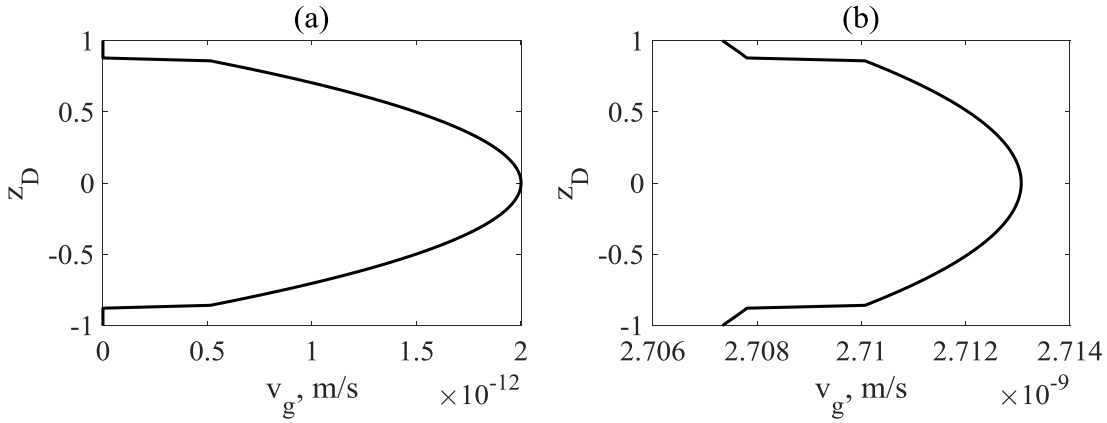

Figure 3-8 (a) Gas velocity profile at extreme hydrophilic surface; (b) gas velocity profile at extreme hydrophobic surface. $P = 50\ MPa$, $h = 10\ nm$. $T = 350\ K$, $\phi = 0.09$, $h_w = 0.7\ nm$.

3.4.4 Pore Geometry

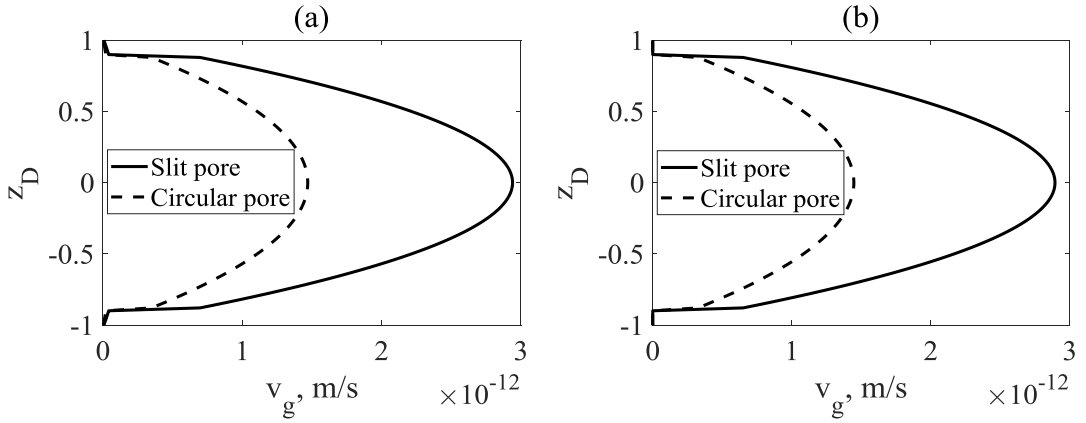

Figure 3-9 (a) Gas velocity profile in slit pore and circular pore with mobile water film; (b) gas velocity profile in slit pore and circular pore with static water film. $P = 50\ MPa$, $h = 12\ nm$, $r = 6\ nm$, $T = 350\ K$, $\phi = 0.09$, $h_w = 0.7\ nm$.

Figure 3-9 compares the gas flow velocity profiles in slit pore and circular pore, which verifies that the same water film thickness in equal-sized slit pore and circular pore generate different water saturation. Take 12 nm-sized slit pore and circular pore as an example, water occupies 11.67% and

21.97% pore volume separately. On this account, given the same total flow area, the reduction in the proportion of gas flow area leads to the decrease of gas flow velocity no matter whether the water molecules move or not.

3.5 Conclusions

This study examines the existence of a mobile high-viscosity water film as a potentially influencing factor in a gas transport model in shale nanopores. The proposed model has been validated through comparison with experimental data. In view of the results found, the following conclusions are drawn: (1) The mobility of the high-viscosity water film should be taken into account in simulating the gas flow pattern in actual shale formations. Ignoring the mobile high-viscosity water film tends to underestimate the gas velocity. The positive impacts of the mobile water film on the gas flow velocity are more significant in the case of a smaller pore size and higher pressure. (2) A gas apparent permeability enhancement factor has been calculated to reflect the gas transport capacity against the pore height and pressure. Similarly, the enhancement factor is more remarkable for a smaller pore and higher pressure. (3) Calculations with regard to a contact angle show that less hydrophilic pores possess a higher gas flow capacity. The influences from the contact angle are relatively more considerable under a smaller pore size and higher pressure. (4) For the same water film thickness, circular pores have smaller gas flow capacity compared with slit pores.

CHAPTER FOUR: GAS TRANSPORT WITH MOBILE HIGH-VISCOSITY WATER FILM AND MOBILE BULK WATER FILM

4.1 Introduction

The previous chapter assumes that all the water molecules exist in form of a high-viscosity water layer in the vicinity of the wall due to the molecular interaction such as electrostatic force and structural force between a solid substrate and water molecules. In fact, when the water saturation is relatively high (which is probably caused by relatively high initial water saturation and injected water during hydraulic fracturing), a certain number of water molecules tend to move directly in channels in the form of bulk water, staying away from the attraction of the solid wall. Liu et al. (2018) adopted MD simulation to explore the methane and water two phase flow in inorganic shale nanopores at different pressure conditions (30 MPa, 60 MPa and 90 MPa). A hydroxylated cristobalite surface was selected to construct the silica slit model, in which 2100 water molecules and 700 methane molecules were placed. During the pressure-driven simulation of methane-water flow at a constant pressure difference, water film-gas-water film structure was observed. Also, the occurrence of two peaks in water density profiles indicated the existence of two water layers near the wall. Both the number density and flow velocity were different for the two water layers. The first layer had a larger density peak and an almost zero velocity while the second layer moved relatively faster. Liu et al. (2018) concluded that the property alteration within the water zone was the result of electrostatic interaction and hydrogen bond between water and surface. Ho et al. (2015) constructed the simulation model with 1800 water molecules and 600 methane molecules in slit-shaped nanopores. They discovered similar structure in which water film was generated near the solid surface while gas molecules stayed in the center even though their experimental pore pressure was in the range of 75 MPa to 250 MPa. Besides, Wu et al. (2013) carried out stable gas-water

pressure-driven flow experiments in 100 nm depth nanotubes and captured optic images with a lab-on-a-chip device. Continuous gas annular flow in the center with a water film (of 0.9-1.6 nm thickness) at the wall had been found at a larger gas velocity. In this chapter, a mobile bulk water layer is thus introduced on the basis of the previously derived model considering a high-viscosity water film. The mobile bulk water film is assumed to distribute evenly between the high-viscosity water layer and gas flow zone. Understanding the structure and transport of bulk water molecules is crucial not only to determine gas-water flow behaviors for the whole range of water saturation, but also to figure out the gas-water relative permeability curves.

4.2 Model Establishment

A bulk water layer is added between a high-viscosity water layer and a gas layer based on the previous model as in Figure 4-1. Pressure driven flow equations and boundary conditions accounting for water true slip and gas slippage are still applicable.

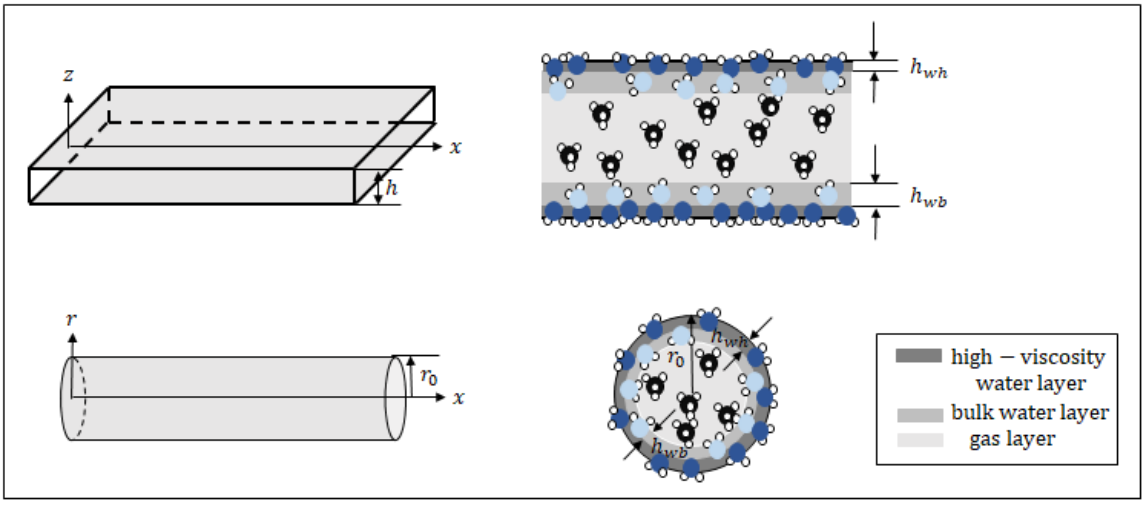

Figure 4-1 Schematic view of the model (bulk water film).

4.2.1 Slit Pores with Mobile High-Viscosity Water Film and Mobile Bulk Water

In the same way, ignoring the corrugation of water film during the flow process, equilibrium distribution of the water layer is divided into a high-viscosity water film with uniform thickness h_{wh} and a bulk water layer with uniform thickness h_{wb} at the inner surface of a slit pore with a height of h as shown in Figure 4-1, and the governing equations for the gas and water phases are modified as:

$$\begin{cases} \frac{\partial^2 v_g}{\partial z^2} = -\frac{\Delta P}{\mu_g L}, z \in [0, \frac{h}{2} - h_{wh} - h_{wb}] \\ \frac{\partial^2 v_{wb}}{\partial z^2} = -\frac{\Delta P}{\mu_{wb} L}, z \in [\frac{h}{2} - h_{wh} - h_{wb}, \frac{h}{2} - h_{wh}] \\ \frac{\partial^2 v_{wh}}{\partial z^2} = -\frac{\Delta P}{\mu_{wh} L}, z \in [\frac{h}{2} - h_{wh}, \frac{h}{2}] \end{cases} \tag{4-1}$$

where v_g is the gas velocity, m/s; v_{wb} is the bulk water velocity, m/s; v_{wh} is the high-viscosity water velocity, m/s; ΔP is an applied pressure difference between the entrance and exit, Pa; L is the length of the pore model, m; h is the height of a slit pore, m; h_{wb} is the thickness of the bulk water film, m; h_{wh} is the thickness of the high-viscosity water film, m.

Similarly, the true slip length l_{ls} and gas slip velocity v_{gs} (Equations (3-1) to (3-3)) are still brought in to account for the solid-liquid interfacial interactions and the liquid-gas interfacial interactions respectively. The specific non-slip boundary conditions in this case are then described as:

$$\begin{cases} \left(\frac{\partial v_g}{\partial z}\right)|_{z=0} = 0 \\ v_g|_{z=\frac{h}{2}-h_{wh}-h_{wb}} = v_{wb}|_{z=\frac{h}{2}-h_{wh}-h_{wb}} - v_{gs}|_{z=\frac{h}{2}-h_{wh}-h_{wb}} \\ \mu_g\left(\frac{\partial v_g}{\partial z}\right)|_{z=\frac{h}{2}-h_{wh}-h_{wb}} = \mu_{wb}\left(\frac{\partial v_{wb}}{\partial z}\right)|_{z=\frac{h}{2}-h_{wh}-h_{wb}} \\ v_{wb}|_{z=\frac{h}{2}-h_{wh}} = v_{wh}|_{z=\frac{h}{2}-h_{wh}} \\ \mu_{wb}\left(\frac{\partial v_{wb}}{\partial z}\right)|_{z=\frac{h}{2}-h_{wh}} = \mu_{wh}\left(\frac{\partial v_{wh}}{\partial z}\right)|_{z=\frac{h}{2}-h_{wh}} \\ v_{wh}|_{z=\frac{h}{2}} = -l_{ls}\frac{\partial v_{wh}}{\partial z}|_{z=\frac{h}{2}} \end{cases} \tag{4-2}$$

Solving Equation (4-1) under the requirements of Equation (4-2) delivers the following velocity profiles:

$$\begin{cases} v_g = -\frac{\Delta P}{\mu_g L}\frac{z^2}{2} + \frac{\Delta P}{\mu_g L}\left(\frac{h}{2} - h_{wh} - h_{wb}\right)\left[\frac{\left(\frac{h}{2}-h_{wh}-h_{wb}\right)}{2} + \frac{2-\sigma_v}{\sigma_v}\frac{\lambda}{1-b\lambda}\right] \\ \qquad + \frac{\Delta P}{2\mu_{wb}L}h_{wb}(h - 2h_{wh} - h_{wb}) + \frac{\Delta P}{2\mu_{wh}L}(hh_{wh} + hl_{ls} - {h_{wh}}^2) \\ v_{wb} = -\frac{\Delta p}{\mu_{wb}L}\frac{z^2}{2} + \frac{\Delta p}{\mu_{wb}L}\frac{\left(\frac{h}{2}-h_{wh}\right)^2}{2} + \frac{\Delta p}{2\mu_{wh}L}\left[hl_s + hh_{wh} - {h_{wh}}^2\right] \\ v_{wh} = -\frac{\Delta p}{\mu_{wh}L}\frac{z^2}{2} + l_{ls}\frac{\Delta p}{\mu_{wh}L}\frac{h}{2} + \frac{\Delta p}{\mu_{wh}L}\frac{h^2}{8} \end{cases} \tag{4-3}$$

Likewise, a gas flow rate equation is further integrated on the basis of the gas velocity equation along the z axis for the cross section of a channel:

$$Q_g = -\frac{\Delta PW}{3\mu_g L}\left(\frac{h}{2} - h_{wh} - h_{wb}\right)^3 + \frac{\Delta PW\left(\frac{h}{2}-h_{wh}-h_{wb}\right)^2}{\mu_g L}\left[\left(\frac{h}{2} - h_{wh} - h_{wb}\right) + \frac{2-\sigma_v}{\sigma_v}\frac{2\lambda}{1-b\lambda}\right] +$$

$$\frac{\Delta PW\left(\frac{h}{2}-h_{wh}-h_{wb}\right)}{\mu_{wb}L}h_{wb}(h - 2h_{wh} - h_{wb}) + \frac{\Delta PW\left(\frac{h}{2}-h_{wh}-h_{wb}\right)}{\mu_{wh}L}(hh_{wh} + hl_s - {h_{wh}}^2) \tag{4-4}$$

where Q_g is the volumetric rate of gas flow in nanopores, m^3/s; W is the width of a slit pore, m.

Similarly, the gas flow rate Q_{gd} arranged in the form of Darcy's equation is presented as:

$$Q_{gd} = \frac{K_g W h}{\mu_g (1-S_w)} \frac{\Delta P}{L} \tag{4-5}$$

where S_w is water saturation, dimensionless. S_w equals to $2(h_{wh} + h_{wb})/h$ for slit pores and $1 - [1 - (h_{wh} + h_{wb})/r]^2$ for circular pores.

Taking the influences of multiphase flow and pore tortuosity τ into account, Q_{gd} takes the following form instead:

$$Q_d = \frac{\phi_g}{\tau} Q_g \tag{4-6}$$

where ϕ_g is the porosity occupied by gas, taking $\phi(h - 2h_{wh} - 2h_{wb})/h$ for slit pores and $\phi(r_0 - h_{wh} - h_{wb})^2/{r_0}^2$ for circular pores, dimensionless.

Substitution of Equations (4-4) and (4-5) into Equation (4-6) obtains the following equation for the determination of gas apparent permeability:

$$K_g = \frac{\phi_g(1-S_w)}{\tau}\{\frac{2}{3h}\left(\frac{h}{2} - h_{wh} - h_{wb}\right)^3 + \frac{2-\sigma_v}{\sigma_v h}\frac{2\lambda}{1-b\lambda}\left(\frac{h}{2} - h_{wh} - h_{wb}\right)^2 + \frac{\mu_g}{\mu_{wb} h} h_{wb}\left(\frac{h}{2} - h_{wh} - h_{wb}\right)(h - 2h_{wh} - h_{wb}) + \frac{\mu_g}{\mu_{wh} h}\left(\frac{h}{2} - h_{wh} - h_{wb}\right)\left(h h_{wh} + h l_{ls} - {h_{wh}}^2\right)\} \tag{4-7}$$

where K_g is the gas apparent permeability in nanopores, m^2.

This research is conducted with special attention to the contribution of the mobile bulk water layer, which can be discussed through the comparison between gas apparent permeability with the bulk water layer K_g and the gas apparent permeability without the bulk water layer K_{gnb}. In this case, when the bulk water layer is not considered and water is reserved in the form of a high-viscosity

water layer, the solution of Equation (4-7) gives the following expression for the gas apparent permeability K_{gnb}:

$$K_{gnb} = \frac{\phi_g(1-S_w)}{\tau}\left[\frac{2}{3h}\left(\frac{h}{2}-h_{wh}\right)^3 + \frac{2-\sigma_v}{\sigma_v h}\frac{2\lambda}{1-b\lambda}\left(\frac{h}{2}-h_{wh}\right)^2 + \frac{\mu_g}{\mu_{wh}h}\left(\frac{h}{2}-h_{wh}\right)\left(l_s h - {h_{wh}}^2 + hh_{wh}\right)\right] \quad (4\text{-}8)$$

4.2.2 Circular Pores with Mobile High-Viscosity Water Film and Mobile Bulk Water

Gas and water transport behaviors are controlled by Equation (4-9) in a circular nanopore with the radius of r_0:

$$\begin{cases} \frac{\mu_g}{r}\frac{\partial}{\partial \mathrm{r}}\left(r\frac{\partial v_g}{\partial r}\right) = \frac{\partial P}{\partial x}, r \in [0, r_0 - h_{wh} - h_{wb}] \\ \frac{\mu_{wb}}{r}\frac{\partial}{\partial \mathrm{r}}\left(r\frac{\partial v_{wb}}{\partial r}\right) = \frac{\partial P}{\partial x}, r \in [r_0 - h_{wh} - h_{wb}, r_0 - h_{wh}] \\ \frac{\mu_{wh}}{r}\frac{\partial}{\partial \mathrm{r}}\left(r\frac{\partial v_{wh}}{\partial r}\right) = \frac{\partial P}{\partial x}, r \in [r_0 - h_{wh}, r_0], z \in [\frac{h}{2} - h_{wh}, \frac{h}{2}] \end{cases} \quad (4\text{-}9)$$

where r_0 is the pore radius, m.

Complied with the boundary conditions listed in Equation (4-10), the derivation of the gas velocity profile with regard to curved surfaces can be displayed in Equation (4-11):

$$\begin{cases} \left(\frac{\partial v_g}{\partial r}\right)|_{r=0} = 0 \\ \mu_g\left(\frac{\partial v_g}{\partial r}\right)|_{r=r_0-h_{wh}-h_{wb}} = \mu_{wb}\left(\frac{\partial v_{wb}}{\partial r}\right)|_{r=r_0-h_{wh}-h_{wb}} \\ v_g|_{r=r_0-h_{wh}-h_{wb}} = v_{wb}|_{r=r_0-h_{wh}-h_{wb}} - v_{gs}|_{r=r_0-h_{wh}-h_{wb}} \\ \mu_{wb}\left(\frac{\partial v_{wb}}{\partial r}\right)|_{r=r_0-h_{wh}} = \mu_{wh}\left(\frac{\partial v_{wh}}{\partial r}\right)|_{r=r_0-h_{wh}} \\ v_{wb}|_{r=r_0-h_{wh}} = v_{wh}|_{r=r_0-h_{wh}} \\ v_{wh}|_{r=r_0} = -l_{ls}\frac{\partial v_{wh}}{\partial z}|_{r=r_0} \end{cases} \quad (4\text{-}10)$$

$$v_g = -\frac{\Delta P}{4\mu_g L}r^2 + \frac{\Delta P}{4\mu_g L}(r_0 - h_{wh} - h_{wb})[(r_0 - h_{wh} - h_{wb}) + \frac{2-\sigma_v}{\sigma_v}\frac{2\lambda}{1-b\lambda}] + \frac{\Delta P}{4\mu_{wb}L}[h_{wb}(2r_0 - 2h_{wh} - h_{wb})] + \frac{\Delta P}{4\mu_{wh}L}(2r_0 l_{ls} - {h_{wh}}^2 + 2r_0 h_{wh}) \quad (4\text{-}11)$$

Integrating Equation (4-11) and the further substitution of Equation (4-6) yield the flow rate and gas apparent permeability equations:

$$Q_g = \frac{\pi\Delta P}{8\mu_g L}(r_0 - h_{wh} - h_{wb})^4 + \frac{2-\sigma_v}{\sigma_v}\frac{\lambda}{1-b\lambda}\frac{\pi\Delta P(r_0-h_{wh}-h_{wb})^3}{2\mu_g L} + \frac{\pi\Delta P(r_0-h_{wh}-h_{wb})^2}{4\mu_{wb}L}[h_{wb}(2r_0 - 2h_{wh} - h_{wb})] + \frac{\pi\Delta P(r_0-h_{wh}-h_{wb})^2}{4\mu_{wh}L}(2r_0 l_{ls} - {h_{wh}}^2 + 2r_0 h_{wh}) \quad (4\text{-}12)$$

$$K_g = \frac{\phi_g(1-S_w)}{\tau}\{\frac{1}{8{r_0}^2}(r_0 - h_{wh} - h_{wb})^4 + \frac{2-\sigma_v}{\sigma_v}\frac{\lambda}{1-b\lambda}\frac{(r_0-h_{wh}-h_{wb})^3}{2{r_0}^2} + \frac{\mu_g(r_0-h_{wh}-h_{wb})^2}{4\mu_{wb}{r_0}^2}[h_{wb}(2r_0 - 2h_{wh} - h_{wb})] + \frac{\mu_g(r_0-h_{wh}-h_{wb})^2}{4\mu_{wh}{r_0}^2}\left(2r_0 l_{ls} - {h_{wh}}^2 + 2r_0 h_{wh}\right)\} \quad (4\text{-}13)$$

Similarly, if the bulk water layer does not exist in circular pores, the gas apparent permeability K_{gnb} is expressed as below:

$$K_{gnb} = \frac{\phi_g(1-S_w)}{\tau}\{\frac{1}{8{r_0}^2}(r_0 - h_{wh})^4 + \frac{2-\sigma_v}{\sigma_v}\frac{\lambda}{1-b\lambda}\frac{(r_0-h_{wh})^3}{2{r_0}^2} + \frac{\mu_g(r_0-h_{wh})^2}{4\mu_{wh}{r_0}^2}\left(2r_0 l_{ls} - {h_{wh}}^2 + 2r_0 h_{wh}\right)\} \quad (4\text{-}14)$$

4.3 Model Validation

The proposed model is first validated with experimental data tested over a wide range of pressure and water saturation. Li et al. (2018) collected two tight-gas sandstone samples from the Yanchang gas field in Ordos Basin, China. X-ray diffraction analysis was conducted to determine the mineral composition, which was made up of a dominant amount of quartz and a small amount of clay

minerals. Mercury injection analysis, water adsorption analysis and gas permeability measurement were carried out to obtain the relationship between water saturation and gas apparent permeability. MICP was applied under pressure ranging from 0.1 MPa to 200 MPa to measure the samples porosity, which turned out to be approximately 8.92% to 10.73%. The gas apparent permeability of both dry and wet samples were calculated by the Darcy's law with the inlet pressure to be less than 2 MPa and outlet pressure to be 0.1 MPa. Also, water saturation was calculated according to the pore size distribution pattern. Finally, the relationship between water saturation and gas apparent permeability among a wide range of pressure and water saturation was obtained, which was used to validate the analytical model. Figure 4-2 presents good agreements between their results and the provided mathematical model above at different water saturation.

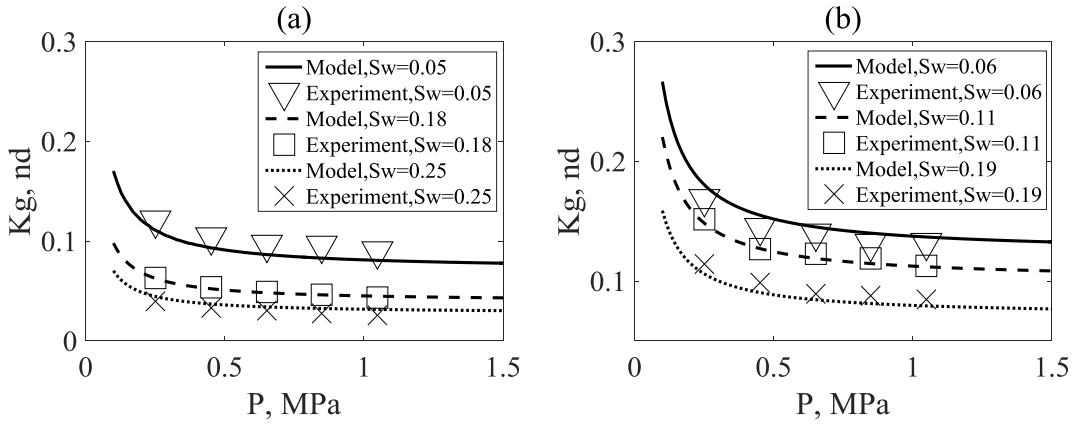

Figure 4-2 (a) Validation of gas apparent permeability with experimental data of shale sample 1 reported by Li et al. (2018), $L = 30\ mm$, $r = 105\ nm$, $T = 300\ K$, $\phi = 0.09$, $h_{wh} = 0.7\ nm$; (b) validation of gas apparent permeability with experimental data of wet shale sample 2 reported by Li et al. (2018), $L = 30\ mm$, $r = 115\ nm$, $T = 300\ K$, $\phi = 0.09$, $h_{wh} = 0.7\ nm$.

4.4 Results and Discussion

4.4.1 Gas Velocity Profile

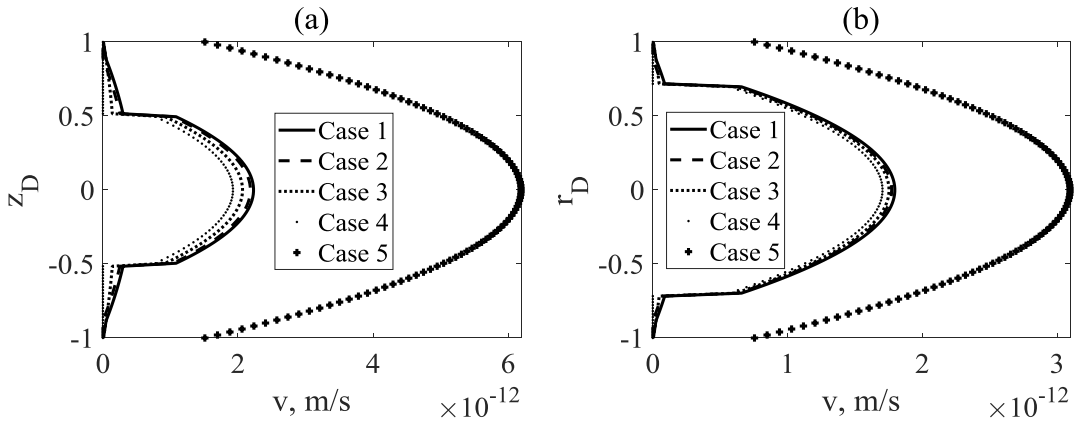

Figure 4-3 (a) Gas velocity profile in slit pore; (b) gas velocity profile in circular pore. $P = 20$ MPa, $S_w = 0.5$, $h = 12$ nm. T = 350 K, $\phi = 0.09$, $h_{wh} = 0.7$ nm. (Case 1: mobile water films; Case 2: static high-viscosity water film and mobile bulk water film; Case 3: mobile high-viscosity water film and no mobile bulk water film; Case 4: static water films; Case 5: single gas flow)

For clarity, the velocity profiles of water-gas confined in slit pore and circular pore with the same dimension are presented in Figure 4-3. Four different cases are compared to discover the impacts of the two water layers. Taking the case study in slit pore as an example, the mobility preservation of two water layers generates the largest gas flow velocity. Owing to the exemption of strong interactions between solid and water phase, the bulk water layer exhibit a larger velocity compare with the water film confined near the surface. Without the high-viscosity water film movement, the gas flow velocity decreases by 2.09% at the centerline. This phenomenon is in good agreement with the previous statements. If the bulk water flow is absent and all the water molecules are regarded as mobile high-viscosity water molecules, the gas velocity tends to be reduced by 7.31%.

Furthermore, once all water molecules are regarded as static, the gas velocity is likely to be underestimated by 13.67%. But if gas flows in a completely dry condition, the gas velocity is much larger due to the expansion of flow area. Therefore, the properties and movements of water molecules coexisting with gas should be treated properly and the influences of water molecules on gas permeability will be analyzed in detail.

4.4.2 Slip Ratio and Gas Apparent Permeability

Results for how gas apparent permeability changes at different pressure ranging from 0 MPa to 25 MPa are plotted in Figure 4-4. On one hand, besides the existence of the high-viscosity water film, the presence of the mobile bulk water layer further occupies the gas flow cross section. On the other hand, the mobile bulk water layer lies between the high-viscosity water layer and the gas zone, accepting the influences from high-viscosity water molecules and providing additional molecular interactions at the gas-liquid interface, thereby transferring the impacts of the high-viscosity water layer, modifying gas molecules momentum and bringing about effects on the gas apparent permeability in nanoscale tubes.

According to Figure 4-4(b), corresponding to the published relationship between gas apparent permeability and pressure (Figure 4-2), along with an increase in reservoir pressure, the gas apparent permeability considering the mobile bulk water layer exhibits an exponential decrease from 768.57 nD to 38.61 nD within the given pressure range. The reduction of gas flow capacity at a higher pressure is ascribed to the drop of a slip ratio, which accounts for the contribution of gas slippage to the total gas apparent permeability (Figure 4-4(a)). It is speculated that, compared with gas intermolecular collisions, gas–wall molecular collisions become dominant with a

decrease in pressure, generating a larger gas flow capacity as the gas flow velocity is improved at the boundary. For the case considering bulk water molecules movement, the proportion of gas slippage contribution reduces from 97.80% to 56.29% along with the increment of pressure.

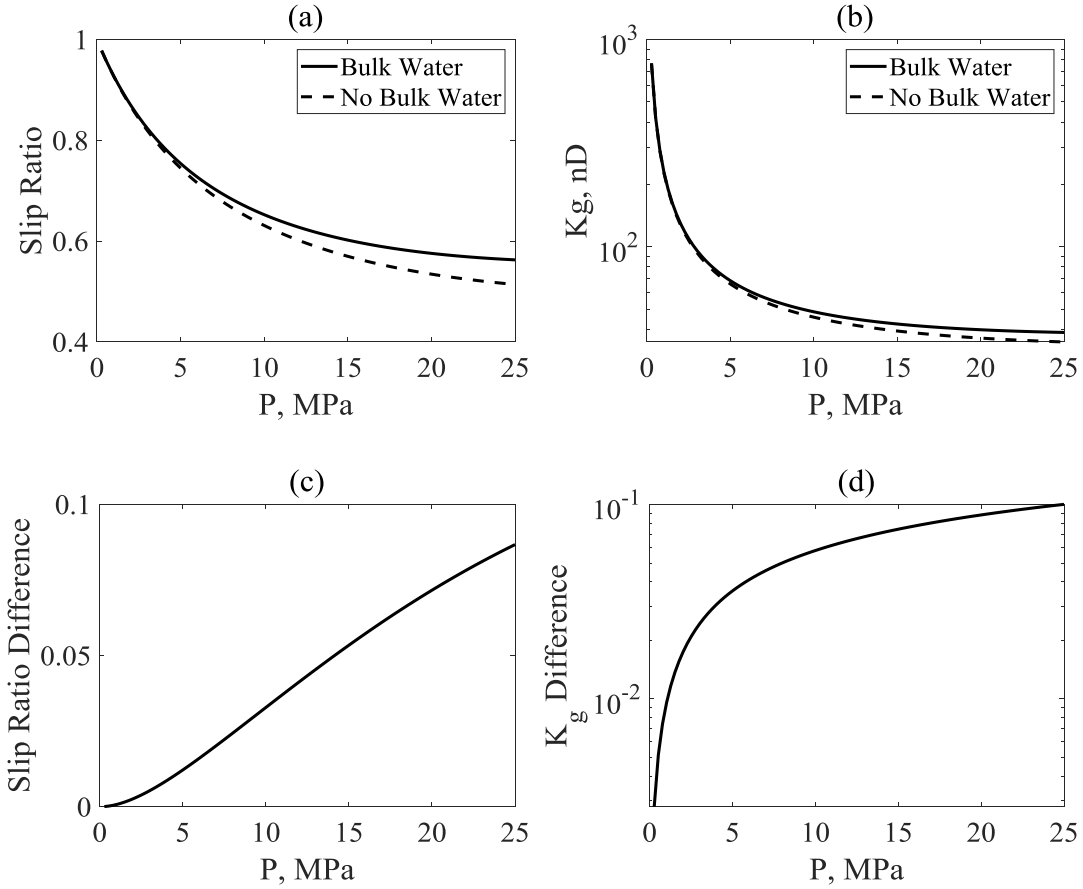

Figure 4-4 (a) Relationship between the slip ratio and pressure, $h = 12\ nm$, $S_w = 0.5$, $T = 350\ K$, $\theta = 30°$, $h_{wh} = 0.7\ nm$; (b) relationship between the gas apparent permeability and pressure, $h = 12\ nm, S_w = 0.5$, $T = 350\ K$, $\theta = 30°$, $h_{wh} = 0.7\ nm$; (c) relationship between slip ratio relative difference and pressure, $h = 12\ nm$, $S_w = 0.5$, $T = 350\ K$, $\theta = 30°$, $h_{wh} = 0.7\ nm$; (d) relationship between gas apparent permeability relative difference and pressure, $h = 12\ nm$, $S_w = 0.5$, $T = 350\ K$, $\theta = 30°$, $h_{wh} = 0.7\ nm$.

The effects of the mobile bulk water layer are investigated in the following section. Figure 4-4(b) reveals that the gas apparent permeability without a bulk water layer reduces with a slightly higher decreasing rate if a higher pressure is applied, following a similar pattern as in the solid line. The increase of pressure from 0 MPa to 25 MPa results in the drop of gas apparent permeability from 766.44 nD to 34.73 nD. Correspondingly, the slip ratio drops to a marked extent from 97.80% to 51.41%. It is quite obvious that the existence of a bulk water layer improves gas flow capacity slightly at a certain pressure. To clarify the discrepancy between the two cases, a slip ratio relative difference and a gas apparent permeability relative difference between the two displayed cases (with and without the mobile bulk water layer) are calculated (Figures 4-4(c) and 4-4(d)). Figure 4-4(d) demonstrates that the existence of the moblie bulk water layer always makes positive contributions to the gas flow capacity. It may be supposed that a higher gas velocity has been achieved due to the existence of the mobile bulk water layer as bulk water molecules are conducive to the generation of smaller water viscosity compared with high-viscosity water molecules. Also, the difference of gas flow capacity increases to 10.04% at the pressure of 25 MPa, confirming that the positive contributions of the mobile bulk water layer to gas flow behavior increases with an increase in pressure. The underlying reason lies in a higher gas viscosity generated by a higher pressure, with which gas flow tends to be more affected by the effects of bulk water flow.

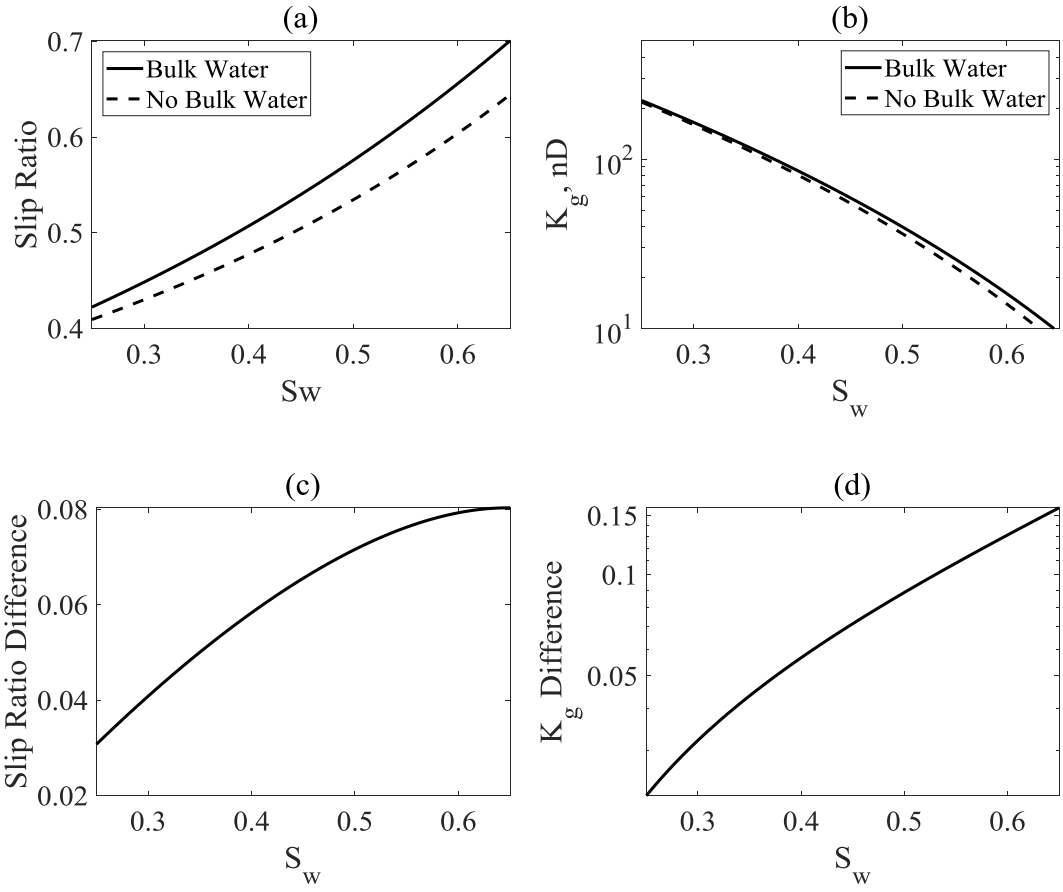

Figure 4-5 (a) Relationship between the slip ratio and water saturation, $h = 12\ nm$, $P = 20\ MPa, T = 350\ K$, $h_{wh} = 0.7\ nm$; (b) relationship between the gas apparent permeability and water saturation, $h = 12\ nm, P = 20\ MPa$, $T = 350\ K$, $h_{wh} = 0.7\ nm$; (c) relationship between slip ratio relative difference and water saturation, $h = 12\ nm, P = 20\ MPa$, $T = 350\ K$, $h_{wh} = 0.7\ nm$; (d) relationship between gas apparent permeability relative difference and water saturation, $h = 12\ nm, P = 20\ MPa$, $T = 350\ K$, $h_{wh} = 0.7\ nm$.

Figure 4-5 puts particular emphasis on the impacts of water saturation. Figure 4-5(b) depicts the relationship between water saturation and gas apparent permeability when the applied pressure is given. It is obvious that, even though the gas slip ratio increases with higher water saturation due to the deduction of gas flow area, the gas transport capacity tends to decay monotonically during

the accumulation of water molecules in nanoscale pores. For example, when the reservoir pressure is set to be 20 MPa, increasing water saturation from 0.25 to 0.65 in a slit pore measuring 12 nm results in a decrease in gas flow capacity by 95.73%. To the contrary, contribution of gas slippage increases from 42.24% to 70.07% (Figure 4-5(a)). It can be concluded that higher water saturation provides a higher gas rate at the water-gas boundary. However, water accumulation occupies more gas flow channel as the pore dimension is determined. The negative effect brought about by the water layer thickness cannot be offset by the positive effect of a higher gas velocity at the interface.

Similarly, the relationship between gas permeability and water saturation in the absence of the bulk water layer resembles the pattern of the solid line in Figure 4-5(b). Even though more water disturbs gas flow behavior, the mobile bulk water is speculated to have a positive effect on improving the gas apparent permeability when water saturation is given as a mobile bulk water layer works better to improve the boundary gas velocity (Figure 4-5(a)). This is owing to the low water viscosity and high movement velocity of bulk water molecules. Figures 4-5(c) and 4-5(d) reinforces this conclusion accurately and further reveals that the positive effect of mobile bulk water layer is more obvious along with an increase in water saturation. The gas apparent permeability relative difference increases to 15.83% and the gas slip ratio difference reaches 8.03% when the water saturation is set to be 0.65. Higher water saturation implies that bulk water molecules achieve a larger portion in the total amount of water molecules, which is conducive to improving the boundary gas velocity.

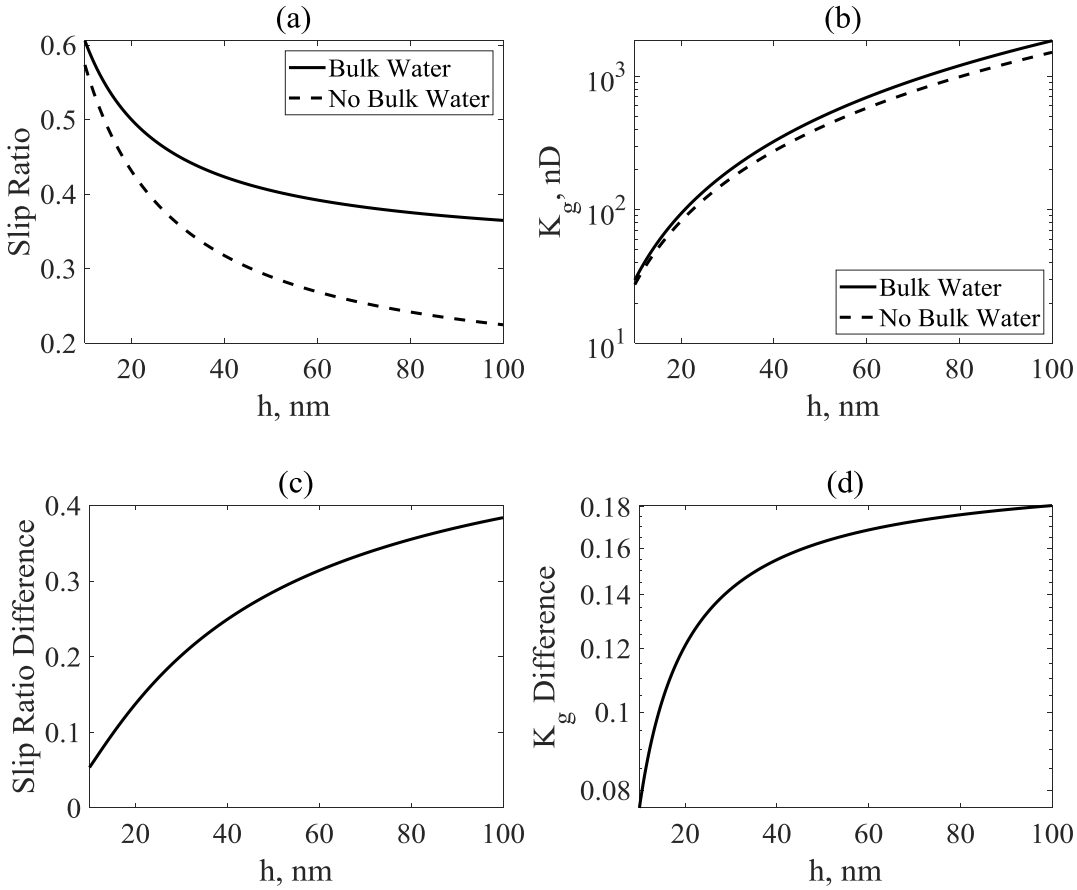

Figure 4-6 (a) Relationship between the slip ratio and pore size, $P = 20\ MPa, T = 350\ K$, $h_{wh} = 0.7\ nm$; (b) relationship between the gas apparent permeability and pore size, $P = 20\ MPa$, $T = 350\ K$, $h_{wh} = 0.7\ nm$;(c) relationship between slip ratio relative difference and pore size, $P = 20\ MPa, T = 350\ K$, $h_{wh} = 0.7\ nm$; (d) relationship between gas apparent permeability relative difference and pore size, $P = 20\ MPa, T = 350\ K$, $h_{wh} = 0.7\ nm$.

Figures 4-6(a) and 4-6(b) compare gas transport behaviors with and without the mobile bulk water film in slit pores ranging from 10 nm to 100 nm when water saturation is given. As illustrated in Figure 4-6, it proves that an increase in pore height is beneficial to gas transport but harmful to slip ratio. Obviously, the increase of the pore height provides a larger gas flow area, contributing to a larger gas apparent permeability. The gas apparent permeability is as large as 1,844.8 nD

inside a 100 nm slit pore. However, gas intermolecular collisions are dominant compared with gas-wall molecular collisions in a larger pore. Gas slippage dominated by gas-wall molecular collisions takes up only 36.48% in a 100 nm-sized pore while it accounts for 60.57% in a 10 nm-sized pore, demonstrating that the gas slip velocity has a less dominant role in determining the gas apparent permeability in a larger pore. On this occasion, the positive influences due to the increase of the gas flow area far outweigh the negative effect generated by the less dominant gas slippage. A large gas flow section makes up for the lost proportion of gas flow determined by gas slippage and improves bulk-gas flow capacity.

In view of the analysis above, no matter whether bulk water exists or not, gas flows much more easily in a larger pore according to the comparison of the solid line and dash line in Figure 4-6(b). For instance, increasing the pore size from 10 nm to 100 nm, the gas apparent permeability increases from 27.5 nD to 1511.5 nD. Figure 4-6(d) further confirms that, provided that water saturation is determined, the contribution of the mobile bulk water film to gas flow capacity increases with an increasing pore height. Bulk water flow works better to assist gas flow in a larger pore as more mobile water generates a larger gas velocity (Figure 4-6(c)). The gas permeability relative differences are 12.11%, 15.47%, 16.85%, 17.60%, 18.07% and the slip ratio relative differences are 13.77%, 24.95%, 31.41%, 35.55%, 38.40% when the pore diameters are 20 nm, 40 nm, 60 nm, 80 nm and 100 nm, respectively.

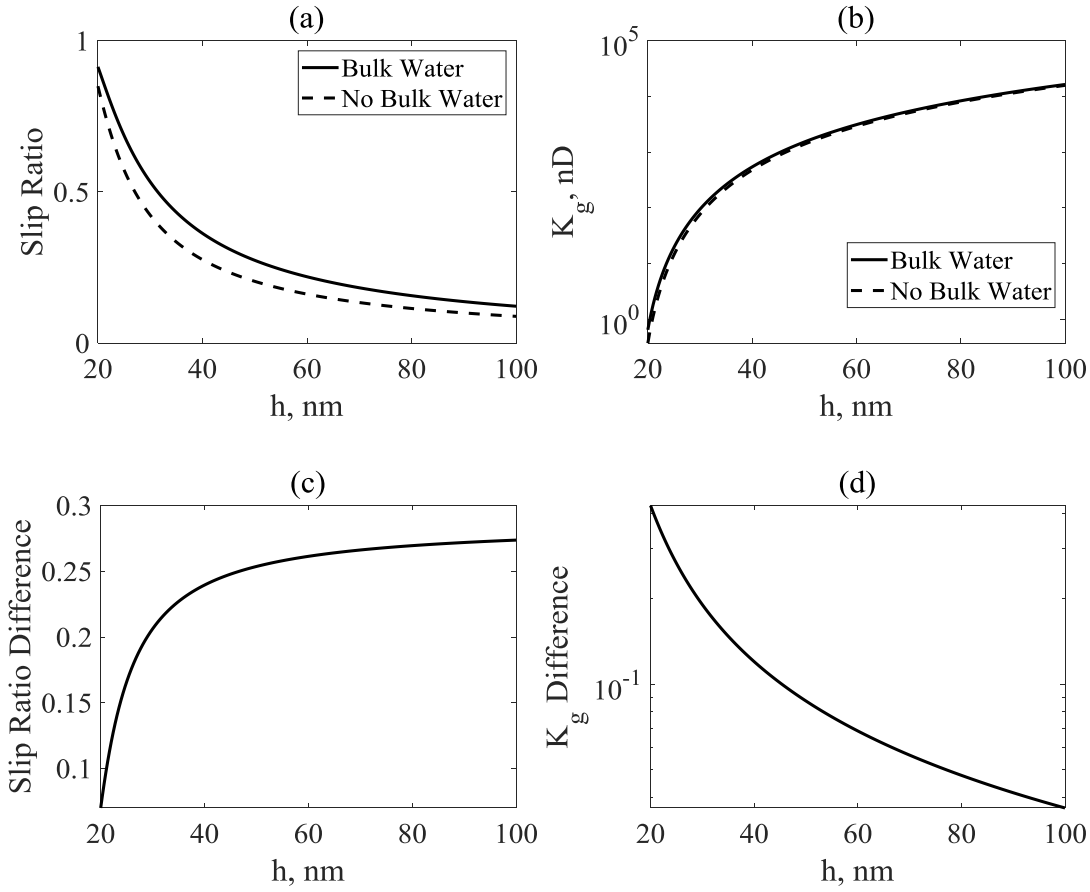

Figure 4-7 (a) Relationship between the slip ratio and pore size, $P = 20\ MPa, T = 350\ K$, $h_{wh} = 0.7\ nm$; (b) relationship between the gas apparent permeability and pore size, $P = 20\ MPa$, $T = 350\ K$, $h_{wh} = 0.7\ nm$;(c) relationship between slip ratio relative difference and pore size, $P = 20\ MPa, T = 350\ K$, $h_{wh} = 0.7\ nm$; (d) relationship between gas apparent permeability relative difference and pore size, $P = 20\ MPa, T = 350\ K$, $h_{wh} = 0.7\ nm$.

Figure 4-7 delivers the effects of pore dimension when water layer thickness is fixed. Figures 4-7(a) and 4-7(b) indicate that the gas transport efficiency is likely to be slightly underestimated without the mobile bulk water film. There is no doubt that gas flow much more easily in a larger pore no matter whether bulk water exists (Figure 4-7(b)). According to the solid line in Figure 4-7(b), when the pore size is assigned to 20 nm, 40 nm, 60 nm and 80 nm and 100 nm, the gas

apparent permeability turns out to be 1 nD, 542 nD, 3,121 nD, 8,354 nD and 16,427 nD respectively. Given a larger pore, gas flow capacity increases to a remarkable extent while the slip ratio declines from 91.38% to 12.22%, which is caused by the less dominant role of gas-solid interactions. With regard to the dash line, both the gas apparent permeability and slip ratio are slightly lower compared to the solid line. The root cause lies in a larger gas-liquid boundary velocity due to the existence of the bulk water layer.

Figures 4-7(c) and 4-7(d) provide more evidence to support the previous opinion that the contribution of the mobile water film on gas flow capacity is positive for the whole range of pore heights. However, Figure 4-7(d) also puts forward that, as long as the total water amount is determined, the positive effects from bulk water flow becomes less significant in a larger pore even though the slip ratio difference is a little larger (Figure 4-7(c)). The gas permeability relative differences are 42.59%, 12.02%, 6.85%, 4.78% and 3.67% and the slip ratio relative differences are 7.0%, 23.96%, 26.14%, 26.95%, 27.37% when the pore diameters are 20 nm, 40 nm, 60 nm, 80 nm and 100 nm, respectively. The contribution of the bulk water layer towards gas slippage becomes less significant in comparison with the contribution of a larger gas flow channel to the total gas flow capacity.

4.5 Special Cases

4.5.1 Water Bridge

Liu et al. (2018) declared that the structure of gas bubble separated by water bridge were also observed when the pressure difference was small in the high-pressure condition (60-90 MPa). However, the water bridge would be destroyed at a larger pressure difference when the gas phase

broke through. At this time, the water bridge thickness became smaller and smaller as water molecules left the water bridge and turned into the form of water film. Ho et al. (2015) also studied the water bridge and they concluded similarly that water bridge would collapse and turned into water layers once a larger acceleration was applied. Unlike Liu et al. (2018) and Ho et al. (2015) who investigated water structures during the pressure-driven flow, Li et al. (2017) described the change of water structure with the relative humidity. They claimed that the adsorbed water film initiate to become thicker and thicker with the increase of water vapor pressure. Once the critical relative humidity was achieved, the film became unstable and the water bridge was formed. The desorption of water molecules from the bridge also happened when the relative humidity was reduced. In this case, even though the water bridge structure is likely to be destroyed by the increase of acceleration and finally turns into water film, the impacts of water bridge structure on gas flow behavior will be studied in this section.

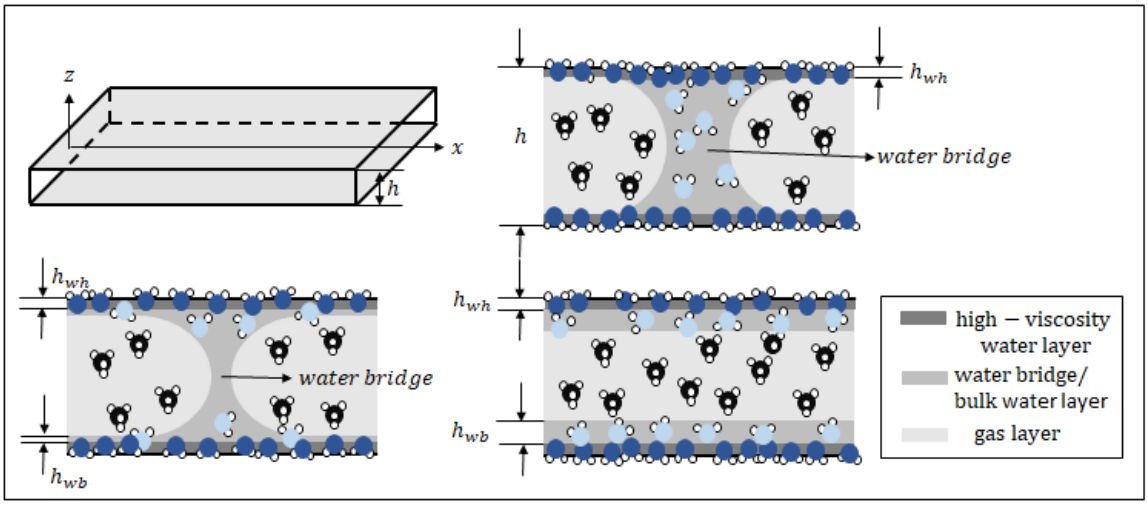

Figure 4-8 Schematic view of the model (water bridge).

The picture on the top right of Figure 4-8 describes the extreme situation when all the extra water molecules are reserved in form of water bridge, serving as a liquid slug to block the gas molecules

advancement. The structure of methane bubble wrapped in water bridge resembles the foam flow in the porous media. As is known, foam is composed of a continuous water phase and a continuous or discontinuous gas phase (Reme, 1999). On one hand, gas relative permeability is reduced by slow-moving bubbles trapping. On the other hand, the presence of water film resists bubbles from moving forward and leads to a larger gas apparent viscosity (Bernard and Holm, 1964). Previous research demonstrates that it is difficult to separate the effects of bubbles on gas relative permeability and viscosity. Accordingly, either the alteration of gas relative permeability or gas viscosity is chosen to account for the modification of gas mobility (Zhou and Rossen, 1995). A mathematical model predicting foam apparent viscosity in smooth capillaries is adopted to evaluate the influences of water bridge on gas flow in nanopore. Hirasaki and Lawson (1985) developed an analytical model (Equation (4-15)) to obtain bubble viscosity considering the contributions of liquid slug, wall slip and Marangoni effect due to surfactant concentration gradient. The calculated apparent viscosity was then introduced to modify the viscosity in Hagen-Poiseuille law which governing the relationship between flow rate and pressure drop. The calculation of parameters differs for bulk foam and individual lamella.

$$\mu_s/\mu_w = L_s n_t + 0.85 n_L r_{cap}/(r_c/r_{cap})\,(3\mu_w v_g/\sigma)^{-1/3}[1 + (r_c/r_{cap})^2] + n_t r_{cap}$$
$$(3\mu_w v_g/\sigma)^{-1/3}\sqrt{N_s}\,tanh(L_{BD}/2) \quad (4\text{-}15)$$

where μ_s is the foam apparent viscosity, cp; μ_w is the water viscosity, cp; L_s is the length of liquid slugs, cm; n_t is the foam texture, 1/cm; r_{cap} is the capillary radius, cm; r_c is the plateau border radius, cm; v_g is the gas velocity, cm/s; σ is the interfacial tension, dyne/cm; N_s and L_{BD} are dimensionless groups.

In this section, as the gas bubbles are different from the surfactant stabilized bubbles, only the contribution of liquid slug is incorporated to mimic the flow resistance of water bridge for gas flow. All extra water molecules are assumed in the form of water bridge except water molecules in the high-viscosity water film. The derived gas flow mathematical model (Equation (3-9)) in Chapter 3 is consequently taken as the base model, with which the gas viscosity is further modified to account for the impacts of water bridge on gas transport. Keeping the water saturation and pore size to be the same, the gas apparent permeabilities and the gas velocity profiles when water molecules are reserved in form of water bridge and bulk water film are compared in Figure 4-9. It shows that the existence of bulk water layer reduces gas apparent permeability to a larger extent, which is probably attributed to the reduction of gas flow dimension (Figure 4-9 (a)). However, the gas flow velocity is larger in the gas zone (when z_D lies in the range of -0.5 to 0.5) when bulk water film exists as the bubble generation blocks gas flow when water bridge exists (Figure 4-9 (b)). Also, the gas flow velocity is still parabolic-shaped. When z_D lies in the range of ±0.12 to ±0.5, the bulk water molecules velocity is smaller compared with bubble velocity (water bridge velocity). For this model, it can be concluded that the gas velocity is restricted by the water bridge while the water bridge velocity is larger than the bulk water velocity. Figures 4-9(c) and 4-9(d) present the gas apparent permeability and velocity profiles with less water molecules. The trends are quite similar to Figures 4-9(a) and 4-9(b) except that both gas apparent permeability and velocity increase as a result of thinner bulk water layer and liquid slug. The gas apparent permeability and gas flow profile of the transition case in which water molecules desorbed from water bridge turn into water film should lie between the solid line and dash line.

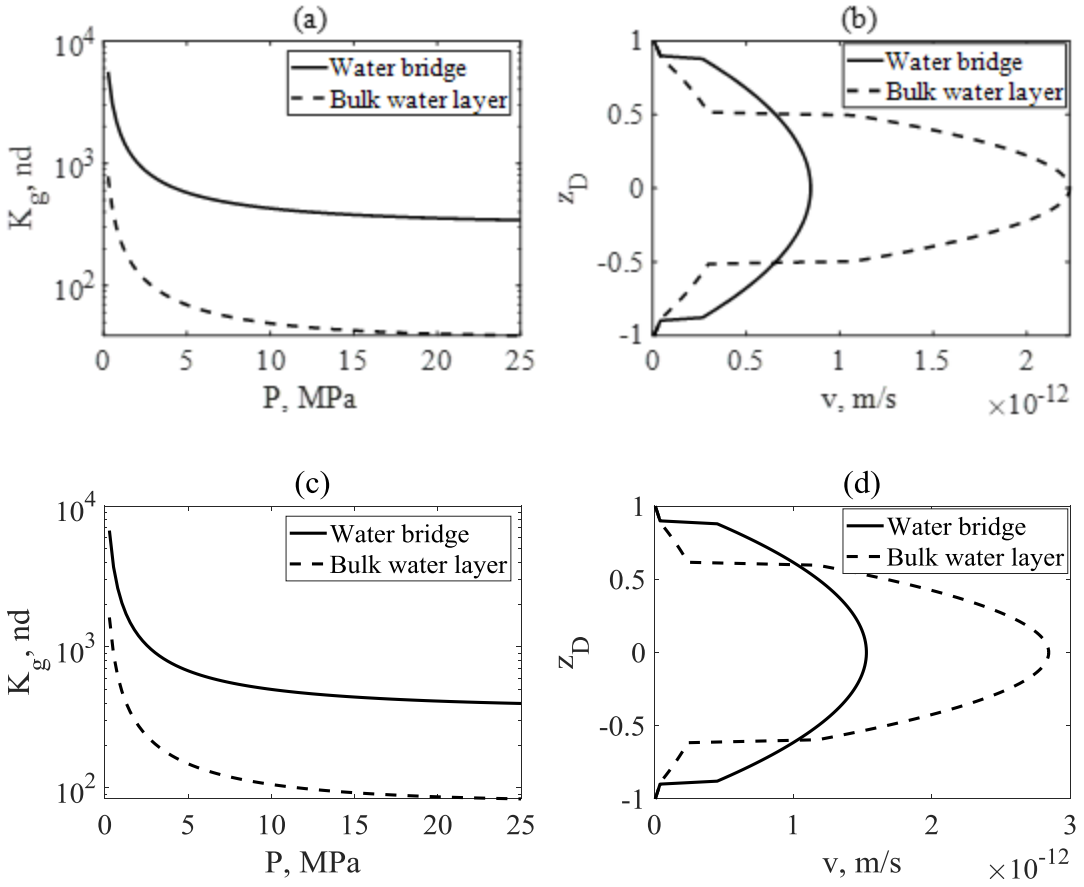

Figure 4-9 (a) Relationship between the gas apparent permeability and pressure, $h = 12\ nm, T = 350\ K$, $h_{wh} = 0.7\ nm$, $S_w = 0.5$; (b) velocity profile, $P = 20\ MPa$, $h = 12\ nm$, $T = 350\ K$, $h_{wh} = 0.7\ nm$, $S_w = 0.5$; (c) relationship between the gas apparent permeability and pressure, $h = 12\ nm, T = 350\ K$, $h_{wh} = 0.7\ nm$, $S_w = 0.4$; (d) velocity profile, $P = 20\ MPa$, $h = 12\ nm$, $T = 350\ K$, $h_{wh} = 0.7\ nm$, $S_w = 0.4$.

4.5.2 Wedged Pores

In the previous section, we mainly focus on two phase flow in two typical pores (slit pore and circular pore). Actually, wedged pore is also frequently discovered in shale rocks. Zhou et al. (2015) conducted a nitrogen adsorption/desorption analysis on shale samples from the Lower Cretaceous, Yingcheng Formation of the southern Songliao Basin and discovered that pore structures are

mainly composed of ink bottle pores, wedge shaped pores and tablet slit pores. Analyzing nitrogen adsorption curves of the Longmaxi shale samples, Zhang et al. (2017) speculated that wedge-shaped pores were the main pore type according to the appearance of hysteresis loops. Xue et al. (2016) classified pore types of marine shale, continental shale and marine-continental shale in China. Wedged pores were one of the main pore structures in marine shale and marine-continental transition shale. Yang et al. (2013) adopted the low-temperature nitrogen gas adsorption method to identify the structure of shale samples from the lower Cretaceous Naijiahe Formation, Liupanshan Basin, Ningxia. They observed that slit-like, inkbottle-like pores and amorphous pores were main pore geometries in shale samples. Numerous evidences suggest that wedged plate pores and tube pores are frequently developed in shale with SEM pictures and the wedging effects of shale pores on fluid transport behaviors are thus required to be examined (Shan et al., 2015; Nikolov, 2014; Slatt and O'Brien, 2017).

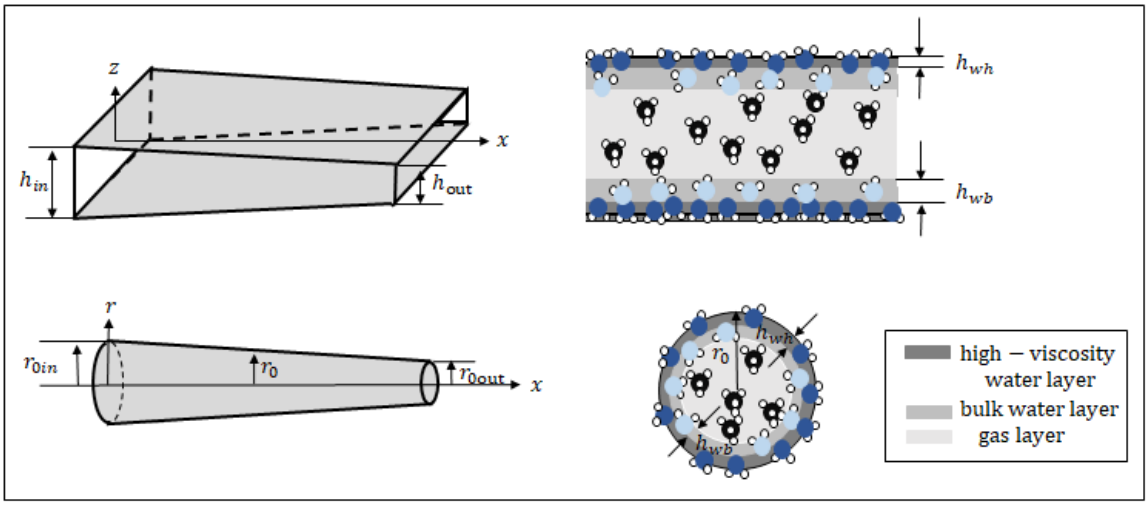

Figure 4-10 Schematic view of the model (wedging effect).

4.5.2.1 Slit Pores with Mobile Bulk Water Film

For actual shale rocks, wedged slit pores are commonly found and therefore a wedging effect should be added into mathematical models to describe its physical influences. As in Figure 4-10, we define the wedging coefficient ς as the ratio of entrance height h_{in} and exit height h_{out}. A larger wedging coefficient is indicative of a more irregular geometry characteristic and higher heterogeneity of a porous medium (Xu et al., 2017):

$$\varsigma = h_{in}/h_{out} \tag{4-16}$$

where ς is a wedging coefficient, dimensionless; h_{in} is a pore height at the gas flow entrance, m; h_{out} is a pore height at the gas flow exit, m.

It is assumed that the pore height decreases linearly along the pore length and therefore the wedging coefficient is always larger than 1. The assumption of linear transition enables the calculation of the pore height at an arbitrary location along the pore length (Xu et al., 2017):

$$\frac{dh}{dx} = \frac{h_{out}-h_{in}}{L} \tag{4-17}$$

Then the gas apparent permeability K_g and K_{gnb} with the consideration of a wedging effect are modified as:

$$K_g = \frac{-(1-S_w)ln\varsigma}{\int_{\frac{h_{in}}{2}-h_{wh}-h_{wb}}^{\frac{h_{out}}{2}-h_{wh}-h_{wb}} \frac{1}{\frac{1}{3}y^3+ay^2+dy}dy} \tag{4-18}$$

$$K_{gnb} = \frac{-(1-S_w)ln\varsigma}{\int_{\frac{h_{in}}{2}-h_{wh}-h_{wb}}^{\frac{h_{out}}{2}-h_{wh}-h_{wb}} \frac{1}{\frac{1}{3}y^3+fy^2+gy}dy} \tag{4-19}$$

where $a, d, f,$ and g are constants, $a = \frac{2-\sigma_v}{\sigma_v}\frac{\lambda}{1-b\lambda} + \frac{\mu_g h_{wb}}{\mu_{wb}} + \frac{\mu_g(h_{wh}+l_{ls})}{\mu_{wh}}$; $d = \frac{\mu_g {h_{wb}}^2}{2\mu_{wb}} + \frac{\mu_g {h_{wh}}^2}{2\mu_{wh}} + \frac{\mu_g h_{wh} h_{wb}}{\mu_{wh}} + \frac{\mu_g h_{wh} l_{ls}}{\mu_{wh}} + \frac{\mu_g h_{wb} l_{ls}}{\mu_{wh}}$; $f = \frac{2-\sigma_v}{\sigma_v}\frac{\lambda}{1-b\lambda} + \frac{\mu_g(h_{wh}+l_{ls})}{\mu_{wh}}$; $g = \frac{\mu_g {h_{wh}}^2}{2\mu_{wh}} + \frac{\mu_g h_{wh} l_{ls}}{\mu_{wh}}$.

4.5.2.2 Circular Pores with Mobile Bulk Water Film

As in Figure 4-10, if the wedging coefficient ς is further considered as the ratio between the entrance radius r_{0in} and the exit radius r_{0out} (Xu et al., 2017):

$$\varsigma = r_{0in}/r_{0out} \tag{4-20}$$

where ς is the wedging coefficient, dimensionless, r_{0in} is a pore radius at the gas flow entrance, m, and r_{0out} is the pore height at the gas flow exit, m, then the gas apparent permeability K_g and K_{gnb} are derived as (for the derivation of the gas apparent permeability of wedging pores, see Appendix B):

$$K_g = \frac{(1-S_w)(1-\varsigma)/(\varsigma r_{0out})}{\int_{r_{0in}-h_{wh}-h_{wb}}^{r_{0out}-h_{wh}-h_{wb}} \frac{1}{\frac{1}{8}y^4 + jy^3 + ny^2} dy} \tag{4-21}$$

$$K_{gnb} = \frac{(1-S_w)(1-\varsigma)/(\varsigma r_{0out})}{\int_{r_{0in}-h_{wh}-h_{wb}}^{r_{0out}-h_{wh}-h_{wb}} \frac{1}{\frac{1}{8}y^4 + py^3 + qy^2} dy} \tag{4-22}$$

where $j = \frac{m}{2} + \frac{\mu_g h_{wb}}{2\mu_{wb}} + \frac{\mu_g(l_{ls}+h_{wh})}{2\mu_{wh}}$; $n = \frac{\mu_g {h_{wb}}^2}{4\mu_{wb}} + \frac{\mu_g {h_{wh}}^2}{4\mu_{wh}} + \frac{\mu_g h_{wh} h_{wb}}{2\mu_{wh}} + \frac{\mu_g l_{ls} h_{wh}}{2\mu_{wh}} + \frac{\mu_g l_{ls} h_{wb}}{2\mu_{wh}}$, $p = \frac{m}{2} + \frac{\mu_g(l_{ls}+h_{wh})}{2\mu_{wh}}$, $q = \frac{\mu_g {h_{wh}}^2}{4\mu_{wh}} + \frac{\mu_g l_{ls} h_{wh}}{2\mu_{wh}}$.

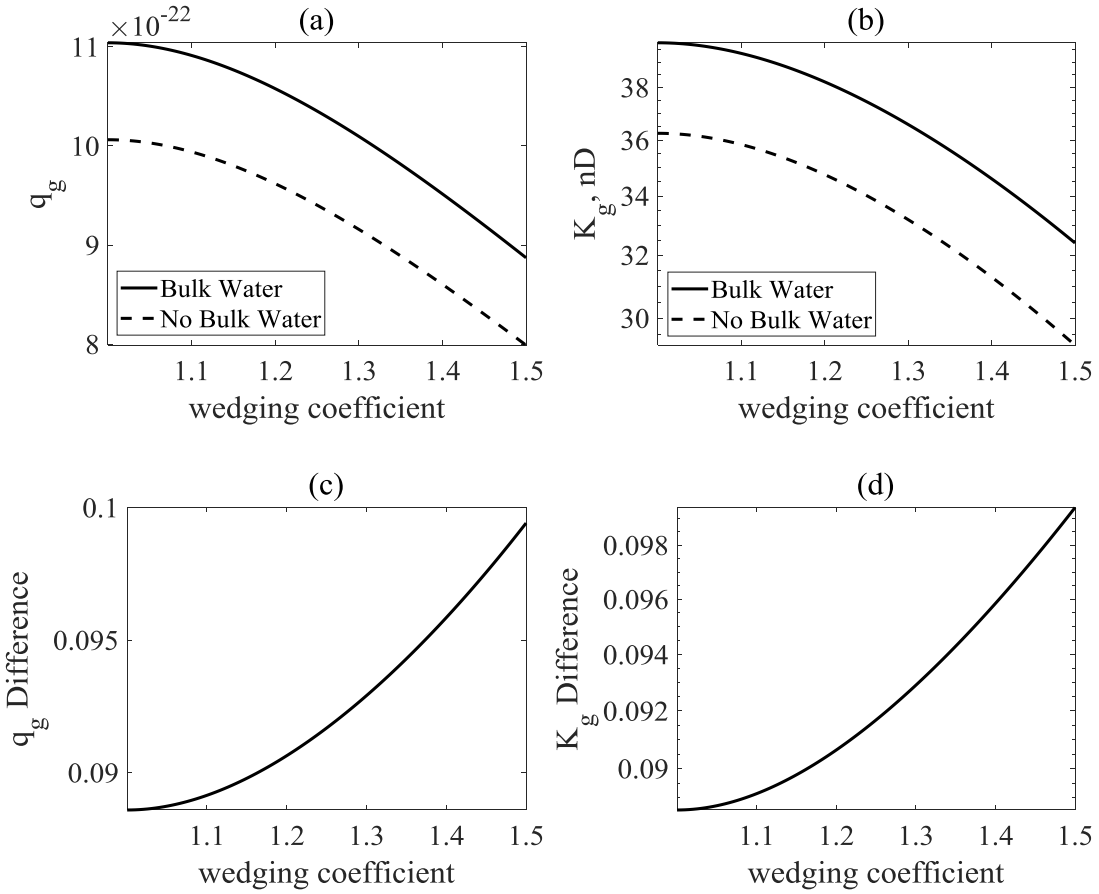

Figure 4-11 (a) Relationship between slip rate and wedging coefficient, $S_w = 0.5$, $P = 20\ MPa$, $h = 12\ nm$, $T = 350\ K$, $\theta = 30°$, $h_{wh} = 0.7\ nm$; (b) relationship between the gas apparent permeability and wedging coefficient, $S_w = 0.5$, $P = 20\ MPa$, $h = 12\ nm$, $T = 350\ K$, $\theta = 30°$, $h_{wh} = 0.7\ nm$; (c) relationship between slip rate relative difference and wedging coefficient, $S_w = 0.5$, $P = 20\ MPa$, $h = 12\ nm$, $T = 350\ K$, $\theta = 30°$, $h_{wh} = 0.7\ nm$; (d) relationship between gas apparent permeability relative difference and wedging coefficient, $S_w = 0.5$, $P = 20\ MPa$, $h = 12\ nm$, $T = 350\ K$, $\theta = 30°$, $h_{wh} = 0.7\ nm$.

As wedged plate pores and tube pores are frequently observed, the wedging effects of shale pores on fluid transport behaviors are discussed. In this section, applied pressure, water saturation and average pore height are set to be constants, and only the wedging coefficient ς is regarded as a

variable, ranging from 1.0 to 1.5. A larger wedging coefficient ς implies a larger entrance height and a smaller exit height. According to Figures 4-11(a) and 4-11(b), a wedging slit pore is liable to decrease gas flow capability as it reduces gas rate. The gas rate is calculated as the gas volumetric rate per unit pore width and per unit pressure gradient. The gas apparent permeability drops from 39.78 nD to 32.40 nD when the wedging coefficient is increased from 1.0 to 1.5. If the average pore height is fixed, a larger wedging coefficient generates a more heterogeneous flow channel, bringing about negative effects for gas transfer.

Figure 4-11(b) also assists to manifest that the negative influence is smaller in the presence of the bulk water layer as bulk water molecules help to recover the gas apparent permeability a little by generating a higher boundary gas velocity. Figure 4-11(d) further presents that the bulk water layer helps to recover gas flow capacity better when the wedging effect is more severe.

4.6 Conclusions

This chapter discusses the influences of a mobile bulk water layer to reflect the effects of water saturation on gas transport behavior. On the basis of the above detailed discussion, it can be concluded that: (1) The gas apparent permeability considering the mobile bulk water layer exhibits an exponential decrease along with an increase in reservoir pressure due to a drop in slip ratio. The presence of the mobile bulk water layer always makes positive contributions towards the gas flow capacity as a higher gas velocity is achieved. Also, the positive contributions of the mobile bulk water layer to gas flow behaviors increase with an increase in pressure. (2) Gas transport capacity decreases monotonically during the accumulation of water molecules in nanoscale pores. This is because the negative effect brought about by the water layer thickness cannot be cancelled by the

positive effect of a higher gas velocity. The positive effect of a mobile bulk water layer is more obvious along with an increase in water saturation. (3) An increase in the pore height is conducive to gas transport as a result of a larger gas flow area, but it hampers the slip ratio. Given that water saturation is determined, the contribution of the mobile bulk water film on gas flow capacity increases with an increasing pore height. If the water layer thickness is fixed, the conclusions are similar to the case with the fixed water saturation above except that the positive effects from bulk water flow become less significant in a larger pore. (4) The existence of bulk water layer reduces gas apparent permeability to a larger extent, but the gas flow velocity is larger at the center line when bulk water film exists as the bubble generation blocks gas flow. (5) A wedging effect is discussed under the assumption that applied pressure, water saturation and average pore height are the same. The results show that a larger wedging coefficient generates a more heterogeneous flow channel, resulting in negative effects for gas transfer. The negative influence is smaller in the presence of the bulk water layer as bulk water molecules help to recover the gas apparent permeability slightly by generating a higher gas velocity.

CHAPTER FIVE: ANALYTICAL MODEL OF GAS-WATER RELATIVE PERMEABILITY IN FRACTAL-LIKE TREE NETWORK

5.1 Introduction

According to experimental observations, shale matrix is usually composed of a wide range of pore size distributions. On the basis of previously derived analytical model, this chapter thus focuses on the two phase flow in shale matrix with a bundle of pores rather than single nanopores. Each pore size distribution has its distinct pore size distribution and pore connectivity, determining the fluid flow and hydrocarbon recovery as confirmed by experiments and simulation. With a specific pore distribution, gas-water relative permeability can be calculated accordingly, which is a necessity of shale gas simulation study.

The effects of a nanopore distribution on gas-water relative permeabilities have been investigated in the previously-mentioned research. Li et al. (2016) concluded that a larger nanotube radius led to higher relative permeabilities. They attributed the reasons to a decrease in an interfacial effect and flow resistance. In contrast, Zhang et al. (2017) introduced a log-normal distributed pore network and found that the water relative permeability reduced with a wider pore size distribution for a fixed mean radius. But the gas relative permeability decreased first and then went up a little along with an increase in water saturation. Also, they concluded that a larger mean radius was conducive to water flow but not beneficial to gas flow.

Besides an equal-sized pore distribution and a log-normal pore distribution, this study assesses the flow properties of gas-water two phases in a fractal-like tree network on the basis of a fractal theory. According to Yu (2008) and Feder (1988), the geometry structures with self-similarity over an

infinite range of length scales were fractals and their dimension was a fractal dimension. Regarding a certain amount of porous media as fractals with self-similar characteristics, Yu (2001) calculated pore statistical properties and flow path tortuosity with the fractal theory. Based on the theoretical background, he introduced fractal dimensions for both saturated and unsaturated porous media, with which two-phase relative permeabilities and flow rates can be obtained (Yu, 2004). In order to figure out how a fractal dimension determined fluid flow, Zhang et al. (2018) incorporated the fractal theory with their derived gas-water flow model. The increment in the fractal dimension or tortuosity fractal dimension tended to increase gas relative permeability but decrease water relative permeability. Based on the fractal theory, an analysis of permeability in a fractal-like tree pore system was proposed by Xu et al. (2006). The tree branched network was proposed by Murray (1926). Xu et al. (2006) managed to study the single-phase flow in a fractal-like tree network through a combination of parallel and series models. It has been shown that a diameter ratio, branching level and branching angle determined an effective permeability significantly. Due to the connectivity between adjacent tubes, a fractal-like tree network had larger gas transport capacity than a parallel network. Chen et al. (2007) also verified an increase in permeability in fractal-like tree networks compared with traditional parallel networks. Wang et al. (2015) adopted the fractal method to investigate a fractal tree-like fracture network and found that the fractal dimension for a fracture network influenced the reservoir connectivity significantly.

In this section, a shale pore network constituted by fractal tree-like distributed branches is presented. The gas-water flow behavior in each branch is governed by the analytical gas-water flow model in a single nanopore considering the presence of mobile water films. The gas-water relative permeabilities in a fractal-like tree network are examined after derivation and validation

against numerous experimental data. The effects of geometric parameters and water films on relative permeabilities are also analyzed.

5.2 Model Establishment

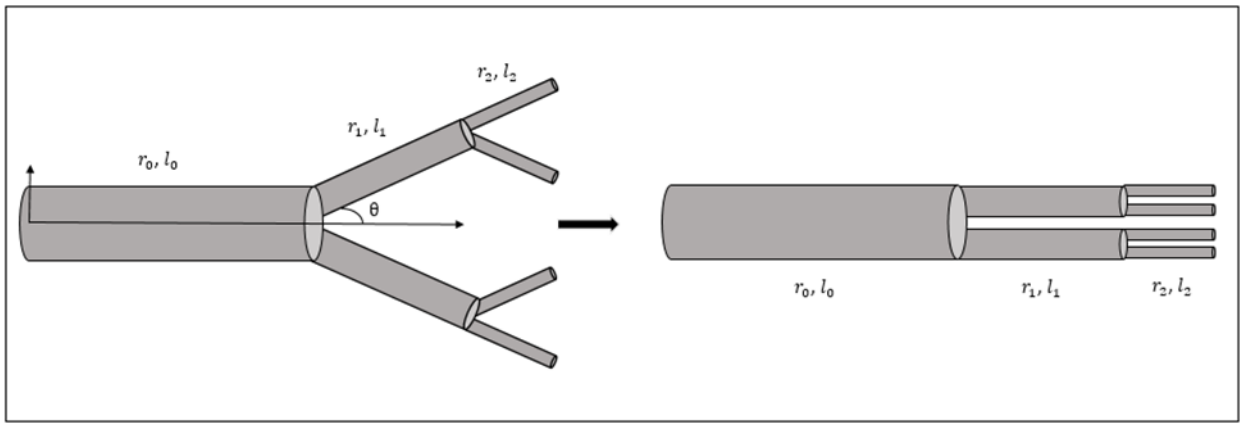

Figure 5-1 Schematic view of fractal-like tree network.

Fractal-like tree network is applied to describe the shale pore structure. Unlike the parallel pore networks, the capillaries of fractal-like tree network at each level connect with each other at a certain angle (Figure 5-1) (Xu et al., 2006). Following Xu et al. (2006), each capillary is divided into M branches and the total branch level is m. Note that for a certain branch level k (k=0, 1, 2…m), its length l_k and radius r_k are set to obey the scaling law:

$$\gamma = l_{k+1}/l_k,\ \beta = r_{k+1}/r_k \tag{5-1}$$

$$l_k = l_0\gamma^k,\ r_k = r_0\beta^k \tag{5-2}$$

As demonstrated by Xu et al. (2006) and Mandelbrot (1982), the branch number M is correlated with length ratio γ and radius ratio β as

$$M = \gamma^{-D_l} = \beta^{-D_d} \tag{5-3}$$

where D_l is the fractal dimension for capillary length distribution, dimensionless; D_d is the fractal dimension for capillary diameter distribution, dimensionless.

Then the derivation of two phase relative permeabilities follows the procedures of the deviation of single gas flow permeability by Xu et al. (2006).The derived model Equation (4-4) are employed to describe the gas flow rate Q_{gk} and water flow rate Q_{wk} in the kth level capillary:

$$Q_{gk} = \frac{\pi\Delta P_{gk}}{8\mu_g l_k}(r_k - h_{wh} - h_{wb})^4 + \frac{2-\sigma_v}{\sigma_v}\frac{\lambda}{1-b\lambda}\frac{\pi\Delta P_{gk}(r_k-h_{wh}-h_{wb})^3}{2\mu_g l_k} +$$

$$\frac{\pi\Delta P_{gk}(r_k-h_{wh}-h_{wb})^2}{4\mu_{wb} l_k}[h_{wb}(2r_k - 2h_{wh} - h_{wb})] + \frac{\pi\Delta P_{gk}(r_k-h_{wh}-h_{wb})^2}{4\mu_{wh} l_k}(2r_k l_{ls} - {h_{wh}}^2 + 2r_k h_{wh}) \quad (5\text{-}4)$$

$$Q_{wk} = \frac{\pi\Delta P_{wk}{h_{wb}}^2}{8\mu_{wb} l_k}(2r_k - 2h_{wh} - h_{wb})^2 + \frac{\pi\Delta P_{wk}(2r_k l_{ls} - {h_{wh}}^2 + 2r_k h_{wh})}{4\mu_{wh} l_k} h_{wb}(2r_k - 2h_{wh} - h_{wb}) +$$

$$\frac{\pi\Delta P_{wk} h_{wh}}{8\mu_{wh} l_k}(2r_k - h_{wh})(4r_k l_{ls} - {h_{wh}}^2 + 2r_k h_{wh}) \quad (5\text{-}5)$$

where Q_{gk} is gas flow rate in the kth level capillary, m^3/s; Q_{wk} is water flow rate in the kth level capillary, m^3/s; ΔP_{gk} and ΔP_{wk} are the pressure drop in the kth level capillary, Pa.

Likewise, in order to obtain the fluid apparent permeability, the flow rate equations complying with Darcy's law in the kth level capillary are written in form of Equations (5-6) and (5-7).

$$Q_{gkd} = \frac{K_{gk}\pi(r_k)^2}{\mu_g(1-S_{wk})}\frac{\Delta P_{gk}}{l_{gk}} \quad (5\text{-}6)$$

$$Q_{wkd} = \frac{K_{wk}\pi(r_k)^2}{\mu_{wb} S_{wk}}\frac{\Delta P_{wk}}{l_{wk}} \quad (5\text{-}7)$$

where $l_{gk} = l_{wk} = l_k$; S_{wk} is water saturation in the kth level capillary, dimensionless.

With the combination of Equations (5-4) to (5-7), the gas permeability K_{gk} and water permeability K_{wk} in the kth level capillary are derived as

$$K_{gk} = (1 - S_{wk})[\frac{1}{8{r_k}^2}(r_k - h_{wh} - h_{wb})^4 + \frac{2-\sigma_v}{\sigma_v}\frac{\lambda}{1-b\lambda}\frac{(r_k-h_{wh}-h_{wb})^3}{2{r_k}^2} +$$

$$\frac{\mu_g(r_k-h_{wh}-h_{wb})^2}{4\mu_{wb}{r_k}^2}h_{wb}(2r_k - 2h_{wh} - h_{wb}) + \frac{\mu_g(r_k-h_{wh}-h_{wb})^2}{4\mu_{wh}{r_k}^2}\left(2r_k l_{ls} - {h_{wh}}^2 + 2r_k h_{wh}\right)] \quad (5\text{-}8)$$

$$K_{wk} = S_{wk}[\frac{{h_{wb}}^2}{8{r_k}^2}(2r_k - 2h_{wh} - h_{wb})^2 + \frac{\mu_{wb}\left(2r_k l_{ls} - {h_{wh}}^2 + 2r_k h_{wh}\right)}{4\mu_{wh}{r_k}^2}h_{wb}(2r_k - 2h_{wh} - h_{wb}) +$$

$$\frac{\mu_{wb}h_{wh}}{8\mu_{wh}{r_k}^2}(2r_k - h_{wh})\left(4r_k l_{ls} - {h_{wh}}^2 + 2r_k h_{wh}\right)] \quad (5\text{-}9)$$

For a fractal tree-like network with kth level branches and M branch number, there are M^k parallel capillaries in total. The equivalent permeability K_{gek} and K_{wek} are averaged on the basis of the cross-sectional area:

$$K_{gek} = \frac{1}{A_{gek}}\sum_{i=0}^{\mathrm{M}^k} A_{gki}\,K_{gki} = (1 - S_{wk})\{\frac{1}{8{r_k}^2}(r_k - h_{wh} - h_{wb})^4 + \frac{2-\sigma_v}{\sigma_v}\frac{\lambda}{1-b\lambda}\frac{(r_k-h_{wh}-h_{wb})^3}{2{r_k}^2} +$$

$$\frac{\mu_g(r_k-h_{wh}-h_{wb})^2}{4\mu_{wb}{r_k}^2}[h_{wb}(2r_k - 2h_{wh} - h_{wb})] + \frac{\mu_g(r_k-h_{wh}-h_{wb})^2}{4\mu_{wh}{r_k}^2}\left(2r_k l_{ls} - {h_{wh}}^2 + 2r_k h_{wh}\right)\} \quad (5\text{-}10)$$

$$K_{wek} = \frac{1}{A_{wek}}\sum_{i=0}^{\mathrm{M}^k} A_{wki}\,K_{wki} = S_{wk}[\frac{{h_{wb}}^2}{8{r_k}^2}(2r_k - 2h_{wh} - h_{wb})^2 +$$

$$\frac{\mu_{wb}\left(2r_k l_{ls} - {h_{wh}}^2 + 2r_k h_{wh}\right)}{4\mu_{wh}{r_k}^2}h_{wb}(2r_k - 2h_{wh} - h_{wb}) + \frac{\mu_{wb}h_{wh}}{8\mu_{wh}{r_k}^2}(2r_k - h_{wh})\left(4r_k l_{ls} - {h_{wh}}^2 +\right.$$

$$\left.2r_k h_{wh}\right)] \quad (5\text{-}11)$$

where A_{gek} and A_{wek} are the equivalent gas and water cross-sectional area of the M^k parallel capillaries, which are calculated as

$$A_{gek} = \mathrm{M}^k\pi(r_k - h_{wh} - h_{wb})^2 \quad (5\text{-}12)$$

$$A_{wek} = \mathrm{M}^k\pi[{r_k}^2 - (r_k - h_{wh} - h_{wb})^2] \quad (5\text{-}13)$$

As illustrated by Xu et al. (2006), the whole fractal-like tree network is then regarded as m equivalent single channels connected end to end with gas permeability K_{gek}, cross-sectional area A_{gek} and length l_{gek}. The m equivalent single channels are further regarded as a single channel with gas permeability K_{ge}, cross-sectional area A_{ge} and length l_{ge}. Darcy equations are transformed into Equations (5-14) and (5-15) with the parameters of the equivalent single channel:

$$Q_g = \frac{K_{ge}}{\mu_g} A_{ge} \frac{\Delta P_g}{l_{ge}} \tag{5-14}$$

$$Q_w = \frac{K_{we}}{\mu_{wb}} A_{we} \frac{\Delta P_w}{l_{we}} \tag{5-15}$$

where ΔP_g and ΔP_w are the pressure drop of the whole network, Pa; l_{ge} and l_{we} are the equivalent capillary length of the whole network, which can be obtained as:

$$l_{ge} = l_{we} = \sum_{k=0}^{m} l_{gk} = l_0 \frac{1-\gamma^{m+1}}{1-\gamma} \tag{5-16}$$

Considering the effect of water saturation, the equations governing the two phase flow in the equivalent single channel are shown as:

$$Q_g = \frac{\pi \Delta P_g}{8\mu_g l_e}(r_e - h_{wh} - h_{wb})^4 + \frac{2-\sigma_v}{\sigma_v}\frac{\lambda}{1-b\lambda}\frac{\pi \Delta P_g (r_e - h_{wh} - h_{wb})^3}{2\mu_g l_e} + \frac{\pi \Delta P_g (r_e - h_{wh} - h_{wb})^2}{4\mu_{wb} l_e}[h_{wb}(2r_e - 2h_{wh} - h_{wb})] + \frac{\pi \Delta P_g (r_e - h_{wh} - h_{wb})^2}{4\mu_{wh} l_e}\left(2r_e l_{ls} - {h_{wh}}^2 + 2r_e h_{wh}\right) \tag{5-17}$$

$$Q_w = \frac{\pi \Delta P_w {h_{wb}}^2}{8\mu_{wb} l_e}(2r_e - 2h_{wh} - h_{wb})^2 + \frac{\pi \Delta P_w \left(2r_e l_{ls} - {h_{wh}}^2 + 2r_e h_{wh}\right)}{4\mu_{wh} l_e} h_{wb}(2r_e - 2h_{wh} - h_{wb}) + \frac{\pi \Delta P_w h_{wh}}{8\mu_{wh} l_e}(2r_e - h_{wh})(4r_e l_{ls} - {h_{wh}}^2 + 2r_e h_{wh}) \tag{5-18}$$

where r_e is the equivalent flow radius in the equivalent single channel, m.

The pressure drop ΔP_g and ΔP_w exhibit the following relationship (Xu et al., 2006):

$$\Delta P_g = \sum_{k=0}^{m} \Delta P_{gk} = \mu_g Q_g \sum_{k=0}^{m} \frac{l_{gk}}{K_{gek} A_{gek}} \tag{5-19}$$

$$\Delta P_w = \sum_{k=0}^{m} \Delta P_{wk} = \mu_{wb} Q_w \sum_{k=0}^{m} \frac{l_{wk}}{K_{wek} A_{wek}} \tag{5-20}$$

Substituting Equations (5-19) and (5-20) into Equations (5-17) and (5-18) to get the following equation in order to solve the equivalent radius r_e and equivalent cross-sectional area A_{ge} and A_{we}:

$$\sum_{k=0}^{m} \frac{l_{gk}}{K_{gek} A_{gek}} \left\{ \frac{\pi}{8 l_{ge}} (r_e - h_{wh} - h_{wb})^4 + \frac{2-\sigma_v}{\sigma_v} \frac{\lambda}{1-b\lambda} \frac{\pi (r_e - h_{wh} - h_{wb})^3}{2 l_{ge}} + \frac{\pi \mu_g (r_e - h_{wh} - h_{wb})^2}{4 \mu_{wb} l_{ge}} [h_{wb}(2r_e - 2h_{wh} - h_{wb})] + \frac{\pi \mu_g (r_e - h_{wh} - h_{wb})^2}{4 \mu_{wh} l_{ge}} \left(2 r_e l_{ls} - {h_{wh}}^2 + 2 r_e h_{wh}\right) \right\} = 1 \tag{5-21}$$

$$\sum_{k=0}^{m} \frac{l_{wk}}{K_{wek} A_{wek}} \left[\frac{\pi {h_{wb}}^2}{8 l_e} (2r_e - 2h_{wh} - h_{wb})^2 + \frac{\pi \mu_{wb} \left(2 r_e l_{ls} - {h_{wh}}^2 + 2 r_e h_{wh}\right)}{4 \mu_{wh} l_e} h_{wb}(2r_e - 2h_{wh} - h_{wb}) + \frac{\pi \mu_{wb} h_{wh}}{8 \mu_{wh} l_e} (2r_e - h_{wh}) \left(4 r_e l_{ls} - {h_{wh}}^2 + 2 r_e h_{wh}\right) \right] = 1 \tag{5-22}$$

The combination of Equations (5-14) and (5-15) and Equations (5-21) and (5-22) deliver the gas permeability K_{ge} and the water permeability K_{we} (Xu et al., 2006):

$$K_{ge} = l_{ge} / \left(A_{ge} \sum_{k=0}^{m} \frac{l_{gk}}{K_{gek} A_{gek}}\right) \tag{5-23}$$

$$K_{we} = l_{we} / \left(A_{we} \sum_{k=0}^{m} \frac{l_{wk}}{K_{wek} A_{wek}}\right) \tag{5-24}$$

In actual, the branches are inclined with an angle ζ. To manifest the function of ζ, Xu et al. (2016) introduced the tortuosity τ represented with Equation (5-25).

$$\tau = \frac{L_t}{L_0} = \frac{l_0 \frac{1-\gamma^{m+1}}{1-\gamma}}{l_0 (1 + \gamma \frac{1-\gamma^m}{1-\gamma} cos\zeta)} \tag{5-25}$$

where L_t is actual path length, m; L_0 is the straight-line distance, m.

After the correction of connect angle ζ, the gas permeability $K_{ge\tau}$ and water permeability $K_{we\tau}$ are modified as (Xu et al., 2006):

$$K_{ge\tau} = l_{ge}/(A_{ge}\tau \sum_{k=0}^{m} \frac{l_{gk}}{K_{gek}A_{gek}}) \quad (5\text{-}26)$$

$$K_{we\tau} = l_{we}/(A_{we}\tau \sum_{k=0}^{m} \frac{l_{wk}}{K_{wek}A_{wek}}) \quad (5\text{-}27)$$

The absolute permeability $K_{e\tau}$ can be achieved when the shale rock is filled with single gas phase according to the process above by defining $h_{wh} = h_{wb} = 0$. The relative permeabilities are then finally worked out:

$$k_{rg} = K_{ge\tau}/K_{e\tau} \quad (5\text{-}28)$$

$$k_{rw} = K_{we\tau}/K_{e\tau} \quad (5\text{-}29)$$

5.3 Model Validation

The derived model is then validated with published relative permeability experimental data. Jerauld and Salter (1990) measured relative permeability with strongly-wetting Berea sandstone. The porosity was 23.9% and the brine permeability was 1000 mD. Piquemal (1994) conducted experiments to obtain steam-water relative permeability of unconsolidated porous media at 150 and 180 ^{o}C. The 250 mm long sample was mainly packed with sand whose granularity was smaller than 75 μm. Berea sandstone with the permeability of 1280 mD and the porosity of 23.4% was used to measure two phase relative permeability by a steady-state method. Brine (1% NaCl) was liquid phase and nitrogen was gas phase in the first experiment carried out at 20 ^{o}C. The gas phase adopted steam for the second experiment (Li and Horne, 2004). Sampath and Keighin (1982) tested gas relative permeability with a tight sandstone core of which the porosity was 7.7%. Nitrogen was

used as gas phase and 2% KCl and 1% NaCl liquid solution were selected to create different water saturation. Wang et al. (2012) adopted tight gas samples from Wyoming and North Sea. The Klinkenberg permeability ranged from 0.0006 mD and 0.3 mD. The porosity was measured to vary between 3% and 12%. Cluff and Byrnes (2010) collected gas relative permeability data according to the tight gas sandstones samples of which the in-situ Klinkenberg permeability from 0.05 to 0.1 mD.

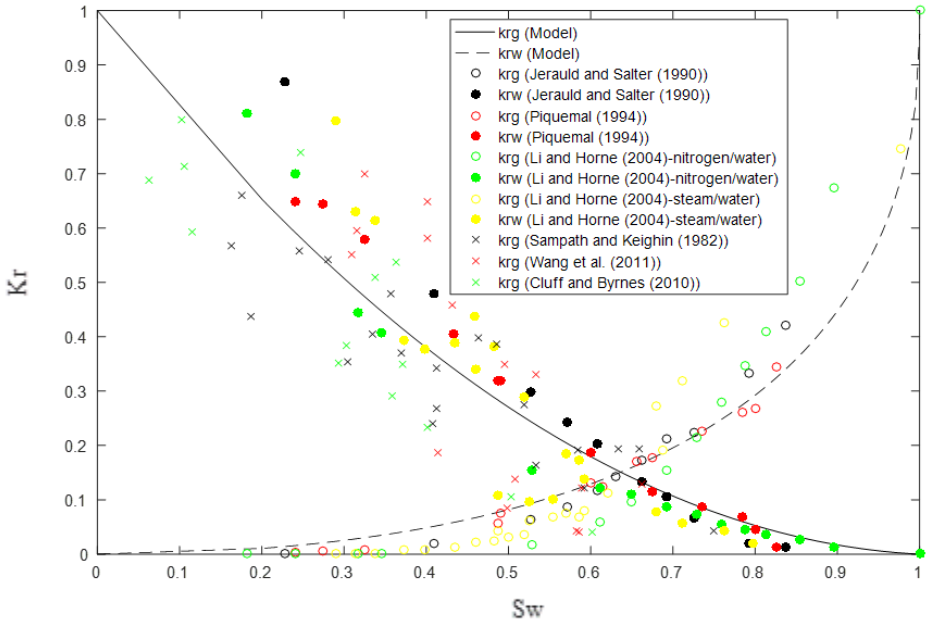

Figure 5-2 Relative permeability comparison between proposed model and experimental data.

5.4 Results and Discussion

This section summarizes the effects of geometric structure (length ratio γ, radius ratio β and branch level m) and mobile water films on the estimated relative permeability curves.

5.4.1 Geometric Structure

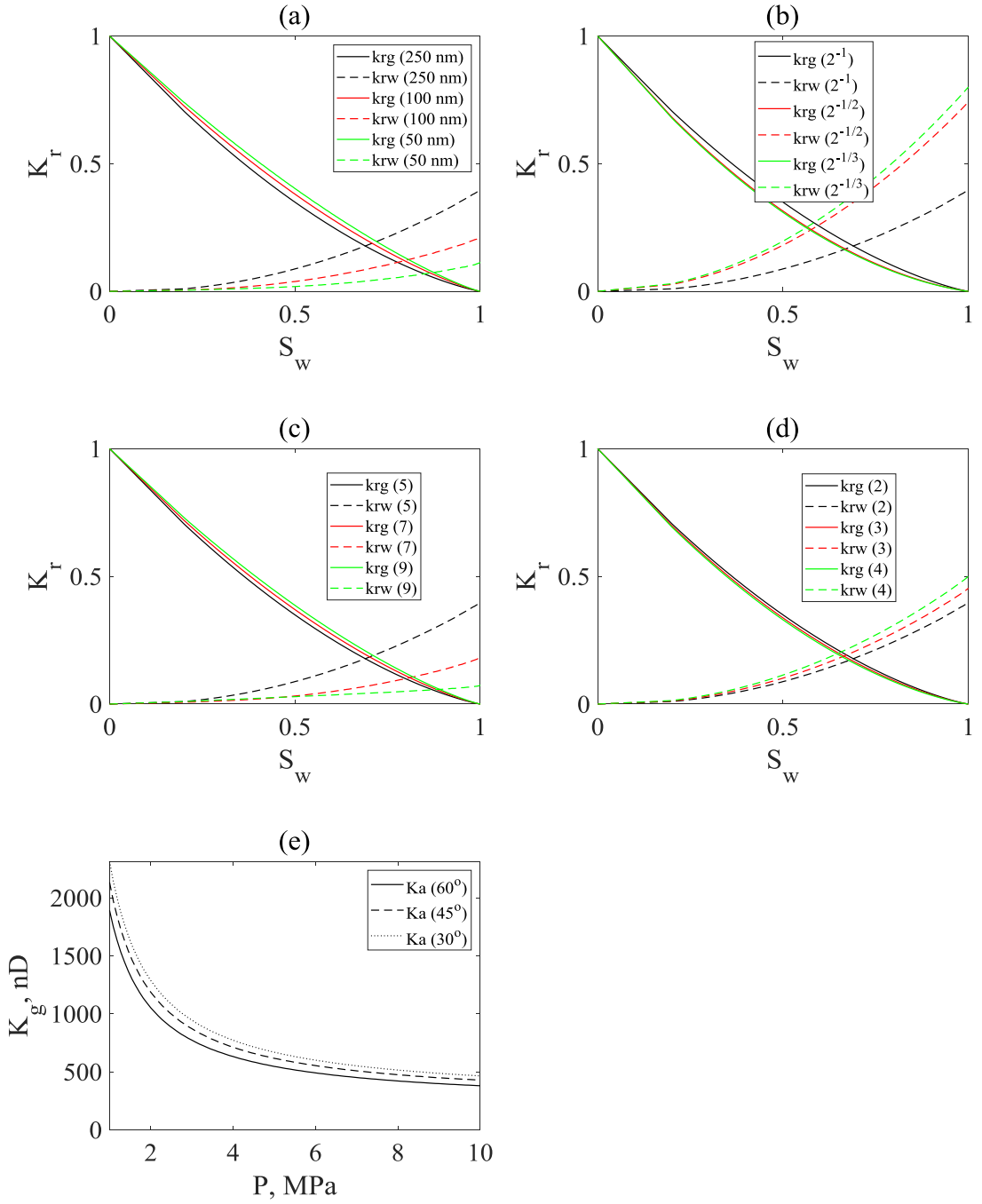

Figure 5-3 (a) Relative permeability with different maximum pore radius. (β=0.5, γ=0.5, m=5, ζ=45°, M=2); (b) Relative permeability with different pore radius ratio for a given maximum radius. (r_0=250 nm, γ=0.5, m=5, ζ=45°, M=2); (c) Relative permeability with different level for a

given maximum radius. (r_0=250 nm, β=0.5, γ=0.5, ζ=45°, M=2); (d) Relative permeability with different branch number for a given maximum radius. (r_0=250 nm, β=0.5, γ=0.5, m=5, ζ=45°); (e) Gas effective permeability with different branch angle for a given maximum radius. (r_0=50 nm, β=0.5, γ=0.5, m=5, M=2).

Figure 5-3 compares the relative permeabilities of gas and water subject to various geometric structures (e.g. different maximum radii and radius ratios), of which the size and connectivity control the fluid flow. Figure 5-3(a) displays the two phase flow capacities in tubes with the maximum radii to be 250 nm, 100 nm and 50 nm separately. In turn, the corresponding equivalent flow radii of the three fractal-like tree networks are averaged to be 83.39 nm, 35.82 nm and 18.66 nm. It is obvious that, for a given water saturation, gas transport relatively more easily in the network with a smaller mean gas flow radius. For example, when the water saturation equals to 0.5, the gas relative permeabilities reach 0.35, 0.38 and 0.40 for the three network dimensions correspondingly. In addition, the equal permeability points, appearing to be 0.69, 0.80 and 0.87 in turn, move towards higher water saturation provided with a smaller flow dimension. This observation indicates that the gas phase flow capacity becomes more dominant in smaller pores, which is qualitatively consistent with the previous results. Likewise, the smaller distance traveled by a moving gas molecule between two walls in a smaller pore network is speculated to explain it. The dominant position of gas-wall molecular collisions and gas slippage brings about the larger gas relative permeability and smaller water relative permeability. In contrast, Figure 5-3(b) reflects the effects of radius ratio β on gas-water transport. A higher radius ratio, standing for a larger equivalent flow radius provided for a given maximum radius and smaller pore radii deviation, enables the water phase to gain an increasing relative flow capacity. In particular, the fractal-like

tree network with a radius ratio of 1 resembles a straight tube with a radius equaling to the maximum radius. According to Figure 5-3(b), the mean equivalent flow radius increases from 83.39 nm to 203.80 nm and 237.80 nm when the radius ratio takes the value of 2^{-1}, $2^{-1/2}$ and $2^{-1/3}$. With the branch level to be 5, 7 and 9, the gas relative permeabilities are 0.39, 0.37 and 0.35 in turn if water saturation remains to be 0.5 (Figure 5-3(c)). Similarly, for a fixed size of the first-level tube, a larger branch level indicates that smaller tubes dominate the pore system, which is beneficial for gas molecules transport. Figure 5-3(d) shows that the gas relative permeability decreases with the increase of branching number. The increase of branching number brings about the drop of mathematic mean radius but an increase in the equivalent flow radius. The influence of branch angle ζ on relative permeabilities is insignificant while ζ is a controlling parameter to determine the gas apparent permeability (Figure 5-3(e)). There is no doubt that a larger branch angle ζ reduces the effective tube length used for gas transport in the flow direction (Figure 5-3(e)) (Xu et al., 2006). More precisely, this phenomenon can be verified with Figure 5-3(e) as the gas apparent permeabilities are calculated to be 379.65 nD, 428 nD and 464 nD at the pressure of 10 MPa.

5.4.2 Water Films

Figure 5-4 illustrates the contributions of the high-viscosity water film and the bulk water film during the determination of gas-water relative transport abilities. Curves in Figure 5-4(a) represent the gas–water flow capacities with mobile high-viscosity water film and bulk water film, with mobile bulk water film only, with static high-viscosity water film and bulk water film, with static high-viscosity water film and bulk water film respectively. Comparing the black curve with the red curve confirms the fact that the high-viscosity water molecules increases water relative flow

resistance compared with bulk water film and a higher water saturation widens this gap. The water relative permeabilities in these two situations reach 0.40 and 0.42 supposed that the pore network is filled with single water phase. Also, the equal permeability points are reported to be 0.09 and 0.11 respectively. The relative difference between black curve and red curve are as large as 5.00% and 22.22% when water saturations are 1 and 0.5, which proves the importance of mobile high-viscosity water film during the calculation of multiphase relative flow capacities. Besides, if the high-viscosity water film loses its mobility, water relative permeability drops slightly as a result of a higher wall attraction, which can be observed through the comparison between the black curve and green curve. Compared with the largest water relative permeability (0.40) of Case 1, the water relative permeability endpoint falls to 0.38 when high-viscosity water molecules stay static. Another feature observed from the comparison between Case 3 and Case 4 is the acceleration of gas molecules movements with the help of mobile water molecules enhances gas relative permeability ultimately. For example, when water saturation equals to 0.5, the gas relative permeability is 0.35 for the green line while it drops to 0.33 for the blue line.

To which degree the water films mobility can exert impacts on relative permeablities is significantly concerned with the geometric structure. Figure 5-4(b) presents the illustrated four cases in a pore network with the maximum radius to be 50 nm. The water relative permeability endpoints are 0.11, 0.16 and 0.08 for the first three situations in turn. Ignoring the existence of mobile high-viscosity water film overestimates the water flow capacity by 45.45%, which leads to the conclusion that the solid-water interaction is more significant in smaller pores as the high-viscosity water film thickness is regarded as a constant. Also, if the high-viscosity water film is

regarded as static, the water phase flow tends to be underestimated by 27.27%, proving higher importance of high-viscosity water film mobility on water flow in smaller tubes.

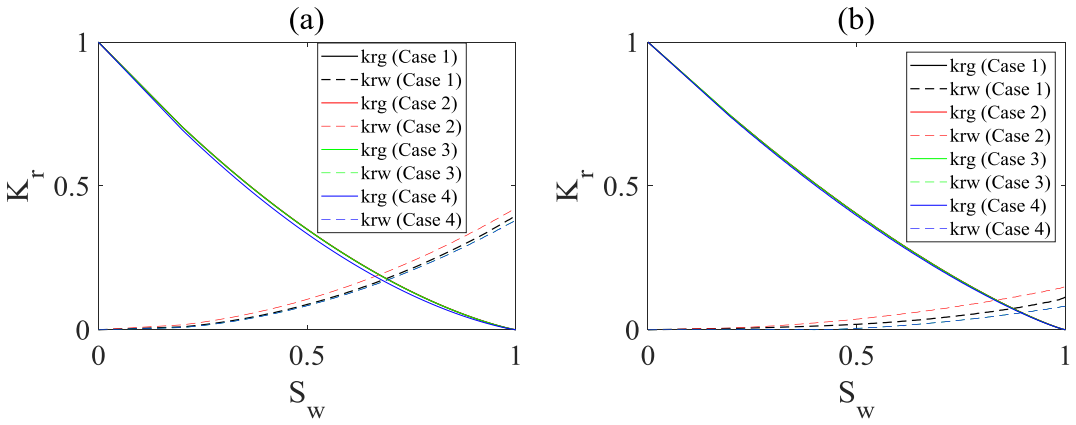

Figure 5-4 (a) Relative permeability with different water films mobility for a given maximum radius. (r_0=250 nm, β=0.5, γ=0.5, m=5, ζ=45°, M=2,); (b) Relative permeability with different water films mobility for a given maximum radius. (r_0=50 nm, β=0.5, γ=0.5, m=5, ζ=45°, M=2) (Case 1: mobile high viscosity water film and bulk water film; Case 2: mobile bulk water film; Case 3: static high viscosity water film and mobile bulk water film; Case 4: static high viscosity water film and static bulk water film).

5.5 Pore Size Distribution

Here are the relative permeability curves calculated on the basis of log-normal distribution and gamma distribution, which ignore the pore connectivity and assume pores to be parallel. These two pore size distributions are frequently discovered in shale rocks as illustrated in Chapter 2. Log-normal pore size distribution of Eagle Ford Shale was detected by Ghanbarian and Javadpour (2017) and Wang et al. (2017). Gamma distribution for the Barnett shale sample was proposed by Moghaddam and Jamiolahmad (2016) and Tian et al. (2017). Integrating flow rate equations in

single nanopores from the minimum radius $r_{0_{min}}$ to the maximum radius $r_{0_{max}}$ generates the total gas flow rate and total water rate:

$$Q_{gl} = N\int_{r_{0_{min}}}^{r_{0_{max}}}\left\{\frac{\pi\Delta P}{8\mu_g L}(r_0 - h_{wh} - h_{wb})^4 + \frac{2-\beta}{\beta}\frac{\ell}{1-b\ell}\frac{\pi\Delta P(r_0-h_{wh}-h_{wb})^3}{2\mu_g L} + \frac{\pi\Delta P(r_0-h_{wh}-h_{wb})^2}{4\mu_{wb}L}[h_{wb}(2r_0 - 2h_{wh} - h_{wb})] + \frac{\pi\Delta P(r_0-h_{wh}-h_{wb})^2}{4\mu_{wh}L}\left(2r_0 l_{ts} - {h_{wh}}^2 + 2r_0 h_{wh}\right)\right\}\frac{1}{r_0\sqrt{2\pi{\sigma_{r_0}}^2}}\exp\left[-\frac{\left(lnr_0-\varsigma_{r_0}\right)^2}{2{\sigma_{r_0}}^2}\right]dr_0 \quad (5\text{-}30)$$

$$Q_{gg} = N\int_{r_{0_{min}}}^{r_{0_{max}}}\left\{\frac{\pi\Delta P}{8\mu_g L}(r_0 - h_{wh} - h_{wb})^4 + \frac{2-\beta}{\beta}\frac{\ell}{1-b\ell}\frac{\pi\Delta P(r_0-h_{wh}-h_{wb})^3}{2\mu_g L} + \frac{\pi\Delta P(r_0-h_{wh}-h_{wb})^2}{4\mu_{wb}L}[h_{wb}(2r_0 - 2h_{wh} - h_{wb})] + \frac{\pi\Delta P(r_0-h_{wh}-h_{wb})^2}{4\mu_{wh}L}\left(2r_0 l_{ts} - {h_{wh}}^2 + 2r_0 h_{wh}\right)\right\}\frac{F^E}{\Gamma(E)}{r_0}^{E-1}\exp(-Fr_0)dr_0 \quad (5\text{-}31)$$

$$Q_{wl} = N\int_{r_{0_{min}}}^{r_{0_{max}}}\left\{\frac{\pi\Delta p{h_{wb}}^2}{8\mu_{wb}L}(2r_0 - 2h_{wh} - h_{wb})^2 + \frac{\pi\Delta p\left(2r_0 l_s - {h_{wh}}^2 + 2r_0 h_{wh}\right)}{4\mu_{wh}L}h_{wb}(2r_0 - 2h_{wh} - h_{wb}) + \frac{\pi\Delta p h_{wh}}{8\mu_{wh}L}(2r_0 - h_{wh})(4r_0 l_s - {h_{wh}}^2 + 2r_0 h_{wh})\right\}\frac{1}{r_0\sqrt{2\pi{\sigma_{r_0}}^2}}\exp\left[-\frac{\left(lnr_0-\varsigma_{r_0}\right)^2}{2{\sigma_{r_0}}^2}\right] \quad (5\text{-}32)$$

$$Q_{wg} = N\int_{r_{0_{min}}}^{r_{0_{max}}}\left\{\frac{\pi\Delta p{h_{wb}}^2}{8\mu_{wb}L}(2r_0 - 2h_{wh} - h_{wb})^2 + \frac{\pi\Delta p\left(2r_0 l_s - {h_{wh}}^2 + 2r_0 h_{wh}\right)}{4\mu_{wh}L}h_{wb}(2r_0 - 2h_{wh} - h_{wb}) + \frac{\pi\Delta p h_{wh}}{8\mu_{wh}L}(2r_0 - h_{wh})(4r_0 l_s - {h_{wh}}^2 + 2r_0 h_{wh})\right\}\frac{F^E}{\Gamma(E)}{r_0}^{E-1}\exp(-Fr_0)dr_0 \quad (5\text{-}33)$$

where Q_{gl} and Q_{gg} are gas flow rate area in log-normal distribution network and gamma distribution network, m^3/s; Q_{wl} and Q_{wg} are water flow rate area in log-normal distribution network and gamma distribution network, m^3/s.

Combining Equations (5-30) to (5-33) with Equation (4-6) obtains Equations (5-34) and (5-37):

$$K_{gl} = N\frac{(1-S_w)}{\mathrm{A}}\mu_g \int_{r_{0min}}^{r_{0max}} \left\{ \frac{\pi}{8\mu_g}(r_0 - h_{wh} - h_{wb})^4 + \frac{2-\beta}{\beta}\frac{\ell}{1-b\ell}\frac{\pi(r_0-h_{wh}-h_{wb})^3}{2\mu_g} + \right.$$

$$\frac{\pi(r_0-h_{wh}-h_{wb})^2}{4\mu_{wb}}[h_{wb}(2r_0 - 2h_{wh} - h_{wb})] + \frac{\pi(r_0-h_{wh}-h_{wb})^2}{4\mu_{wh}}\left(2r_0 l_{ts} - {h_{wh}}^2 + \right.$$

$$\left.\left. 2r_0 h_{wh}\right)\right\} \frac{1}{r_0\sqrt{2\pi{\sigma_{r_0}}^2}} \exp\left[-\frac{(lnr_0-\varsigma_{r_0})^2}{2{\sigma_{r_0}}^2}\right] dr_0 \quad (5\text{-}34)$$

$$K_{gg} = N\frac{(1-S_w)}{\mathrm{A}}\mu_g \int_{r_{0min}}^{r_{0max}} \left\{ \frac{\pi}{8\mu_g}(r_0 - h_{wh} - h_{wb})^4 + \frac{2-\beta}{\beta}\frac{\ell}{1-b\ell}\frac{\pi(r_0-h_{wh}-h_{wb})^3}{2\mu_g} + \right.$$

$$\frac{\pi(r_0-h_{wh}-h_{wb})^2}{4\mu_{wb}}[h_{wb}(2r_0 - 2h_{wh} - h_{wb})] + \frac{\pi(r_0-h_{wh}-h_{wb})^2}{4\mu_{wh}}\left(2r_0 l_{ts} - {h_{wh}}^2 + \right.$$

$$\left.\left. 2r_0 h_{wh}\right)\right\} \frac{F^E}{\Gamma(E)} {r_0}^{E-1} \exp(-Fr_0)\, dr_0 \quad (5\text{-}35)$$

$$K_{wl} = N\frac{(S_w)}{\mathrm{A}}\mu_w \int_{r_{0min}}^{r_{0max}} \left\{ \frac{\pi{h_{wb}}^2}{8\mu_{wb}}(2r_0 - 2h_{wh} - h_{wb})^2 + \frac{\pi\left(2r_0 l_s - {h_{wh}}^2 + 2r_0 h_{wh}\right)}{4\mu_{wh}} h_{wb}(2r_0 - 2h_{wh} - \right.$$

$$\left. h_{wb}) + \frac{\pi h_{wh}}{8\mu_{wh}}(2r_0 - h_{wh})(4r_0 l_s - {h_{wh}}^2 + 2r_0 h_{wh})\right\} \frac{1}{r_0\sqrt{2\pi{\sigma_{r_0}}^2}} \exp\left[-\frac{(lnr_0-\varsigma_{r_0})^2}{2{\sigma_{r_0}}^2}\right] dr_0 \quad (5\text{-}36)$$

$$K_{wg} = N\frac{(S_w)}{\mathrm{A}}\mu_w \int_{r_{0min}}^{r_{0max}} \left\{ \frac{\pi{h_{wb}}^2}{8\mu_{wb}}(2r_0 - 2h_{wh} - h_{wb})^2 + \frac{\pi\left(2r_0 l_s - {h_{wh}}^2 + 2r_0 h_{wh}\right)}{4\mu_{wh}} h_{wb}(2r_0 - 2h_{wh} - \right.$$

$$\left. h_{wb}) + \frac{\pi h_{wh}}{8\mu_{wh}}(2r_0 - h_{wh})(4r_0 l_s - {h_{wh}}^2 + 2r_0 h_{wh})\right\} \frac{F^E}{\Gamma(E)} {r_0}^{E-1} \exp(-Fr_0)\, dr_0 \quad (5\text{-}37)$$

where K_{gl} and K_{gg} are gas apparent permeability in log-normal distribution network and gamma distribution network, m^2; K_{gl} and K_{gg} are water permeability in log-normal distribution network and gamma distribution network, m^2.

Finally, assigning 100 nm to the largest radius and 1 nm to the smallest radius, the relative permeability curves can be plotted as in Figure 5-5. Both the pore size and pore connection exert tremendous influences to the phase flow capacities.

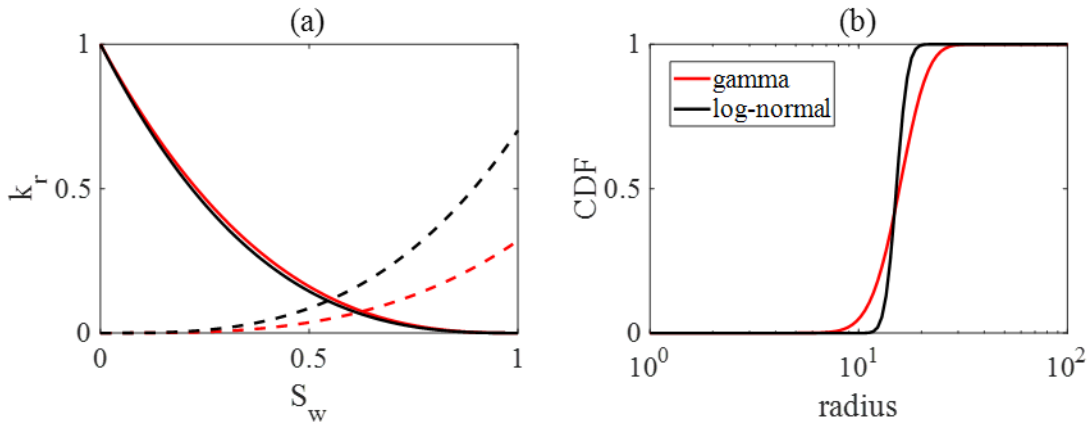

Figure 5-5 (a) Comparison of gas apparent permeability relative permeability curves between log-normal distribution and gamma distribution (r_{0max}=100 nm, r_{0min}=1 nm, ς_{r_0}=2.718 nm, σ_{r_0}=0.1 nm, E=16, F=1); (b) comparison of cumulative distribution functions between log-normal distribution and gamma distribution (r_{0max}=100 nm, r_{0min}=1 nm, ς_{r_0}=2.718 nm, σ_{r_0}=0.1 nm, E=16, F=1).

5.6 Conclusions

This chapter evaluates the gas-water flow capacities in a fractal-like tree pore network instead of single nanopores. The proposed model has been validated through comparison with experimental data. In view of the discussed results, the following conclusions are obtained: (1) Gas relative permeability is larger in the network with a smaller mean gas flow radius due to more dominant gas-wall molecular collisions and the consequent larger gas slippage. The equal permeability points move towards a higher water saturation along with a decrease in flow dimension. (2) A larger radius ratio signifies a smaller pore radii deviation provided with a fixed equivalent flow radius, leading to a reduction in gas relative permeability. (3) A larger branch level indicates that smaller tubes in the pore system for a fixed first-level pore size are beneficial for gas molecules transport. (4) Gas relative permeability decreases with the increase of branching number as a result

of a larger gas flow radius. (5) The gas apparent permeability is smaller with a larger branch angle as a larger branch angle results in the reduction of effective tube length used for gas transport in the flow direction. (6) Ignoring the high-viscosity water molecules reduces the water flow resistance as the water viscosity is increased while it poses negligible influence on gas relative flow capacity. This phenomenon is more significant in smaller tubes. (7) If the high-viscosity water film loses its mobility, water relative permeability drops slightly as a result of a higher wall attraction. (8) The mobile bulk water film increases the gas molecules movements as it provides a larger gas velocity at the water-gas boundary. (9) Different pore network has different relative permeability curves, which significantly depending on the pore radius distribution.

CHAPTER SIX SHALE GAS SIMULATION MODELING

6.1 Introduction

The research focus will be switched from the pore scale to the reservoir scale in this chapter. Reservoir simulation is conducted with incorporation of the previously derived gas apparent permeability model and the gas-water relative permeability curves. Accurate estimation of cumulative gas production and gas rate can be finally achieved.

Shale gas simulation is different from the simulation of conventional reservoir due to its tight rock and complex composition. Given its specific geological structure, a too small grid size will definitely lead to convergence problem in CMG. In this case, fractures are given a larger fracture width with lower effective permeability, which is different from intrinsic permeability. To avoid misunderstanding, fracture conductivity rather than fracture permeability is adopted to reflect the flow capacity of fractures in CMG. Fracture conductivity is defined as the product of intrinsic permeability and fracture width, which also equals to the product of effective permeability and grid size. Generally, fracture conductivity measures the fluid flow capacity through a fracture and the fluid flow rate is a function of fracture conductivity (CMG, 2016). Also, due to the great variety in geometry and flow transport mechanisms of matrix and fractures, shale gas reservoir numerical modelling is mainly conducted with dual porosity model and dual permeability model in CMG. For dual porosity model, the high permeable fracture is the primary continuum for fluid flow. In contrast, the disconnected matrix serves as fluid storage area, providing fluid for the fracture network. In this case, each grid block has two properties assigning for matrix and fracture separately. The fluid flows between fractures and from matrix to fracture. The latter is controlled by shape factor, which is closely related to fracture spacing and matrix permeability. In the case

of dual permeability model, matrix also works as flow path and matrix to matrix flow is allowed (Novlesky et al., 2011). LS-LR-DK method is put forward to save the run times by modeling fracture network explicitly with local grid refinement for dual permeability model. Different from even gridding, local refinement generates more grids near the fracture to capture the phenomenon more accurately with relative high efficiency (CMG, 2016; Novlesky et al., 2011).

In this section, with the derived gas apparent permeability and relative permeabilities models, a dual permeability model is selected to simulate the two phase flow in shale gas reservoir with CMG GEM according to the actual geological properties and production history data. The objective is to accurately capture the nanoscale dynamic flow properties of methane in the wet condition and develop a reservoir simulation model for shale gas production forecast.

6.2 Model Establishment

Li et al. (2011) constructed simulation models to match the production data from a Barnett shale gas well. According to Li et al. (2011), a base simulation model with a grid size of 25 m x 100 m x 1 m is built with the calculated properties. In total, there are 25 x 10 x 90 grids, covering an area of 625 m x 1000 m with the net pay to be 90 m. The initial pressure is 20 MPa and the top depth is 2133.6 m. For the hydraulic fractures, the fracture conductivity is set to be 1.1 mD·m with the half-length to be 50 m. Number of refinements near the fracture is 5 x 5 x 1 and there are 10 fracturing stages in total. Due to the use of dual permeability model, two sets of properties representing different storage capacity and transport ability are defined for matrix and fracture. The matrix porosity is set to be 0.04 and gas apparent permeability is calculated with the previously derived analytical model according to the reservoir pressure and the determined pore size. The

initial water saturation is 0.1. Also, gas-water relative permeability curves are calculated with the fractal-like tree pore distribution at the given pressure. The details of the base model properties are listed in Figures 6-1 and 6-2 and Table 6-1.

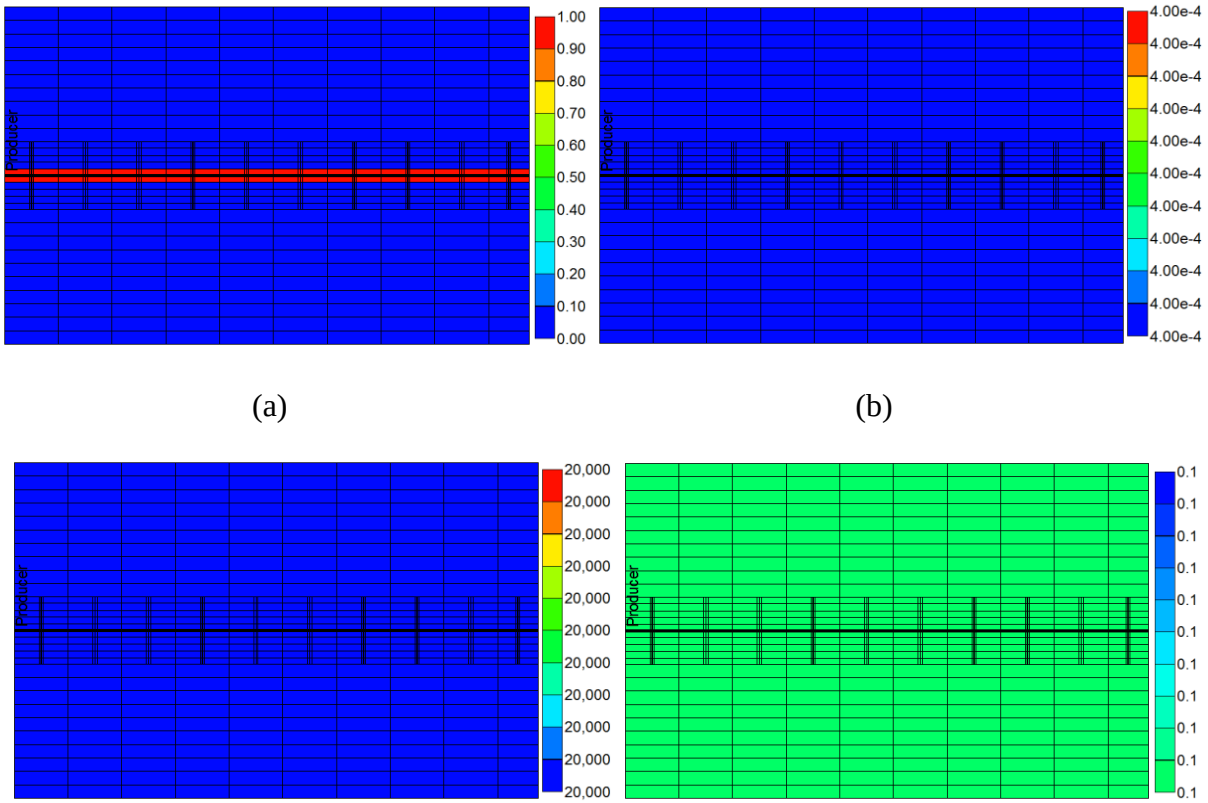

Figure 6-1 Properties for base Barnett shale gas well model ((a) fracture permeability distribution (mD); (b) fracture porosity distribution (dimensionless); (c) fracture pressure distribution (KPa); (d) fracture water saturation distribution (dimensionless)).

Table 6-1 Parameters for base Barnett shale gas well model

Parameter	Value	Parameter	Value
Number of grids in x direction	25	Initial Pressure, MPa	20
Number of grids in y direction	10	Depth, m	2,133.6
Number of grids in z direction	90	Thickness, m	90
Grid size, x, m	25	Number of fracturing stages	10
Grid size, y, m	100	Fracture half length, m	50
Grid size, z, m	1	Fracture conductivity, $md \cdot m$	1.1

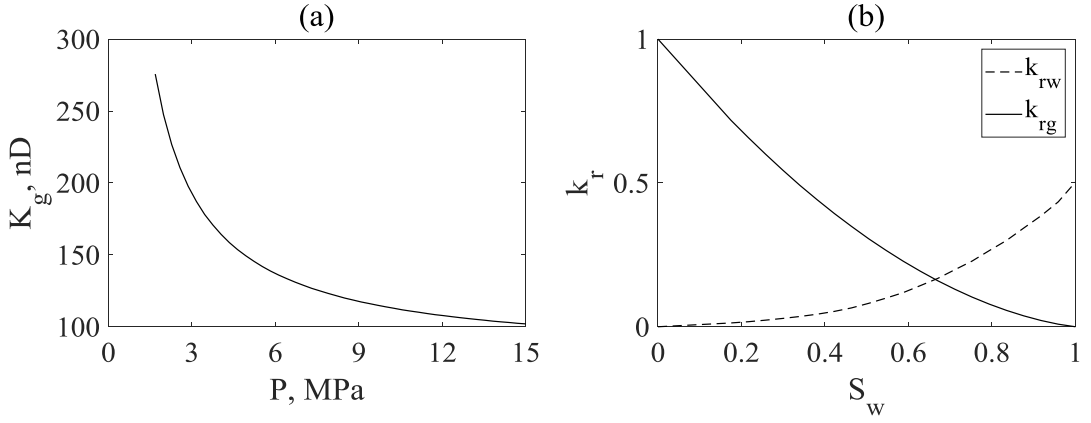

Figure 6-2 Properties for base Barnett shale gas well model ((a) gas apparent permeability and pressure relationship; (b) relative permeability curves.

6.3 Model Validation

To conduct history match between the base simulation model and the given Barnett shale gas well, the well bottom-hole pressure is set according to the production history (Figure 6-3(c)) (Li et al., 2011). The model has been validated with the input parameters in Table 6-1 and Figures 6-1 and 6-2. The comparisons of gas production rate and water production rate between history data and simulation results are displayed in Figures 6-3(a) and 6-3(b). Both the gas production rate and water production rate exhibit exponential decrease for the whole production period. Figures 6-3(a) records that the gas rate roars to the highest level (40,000-50,000 m^3/day) and experiences a steep

decline to 15,000 m^3/day immediately, which is a typical shale gas production case. Water rate also falls promptly after instant increase at the initial production stage (Figures 6-3(b)).

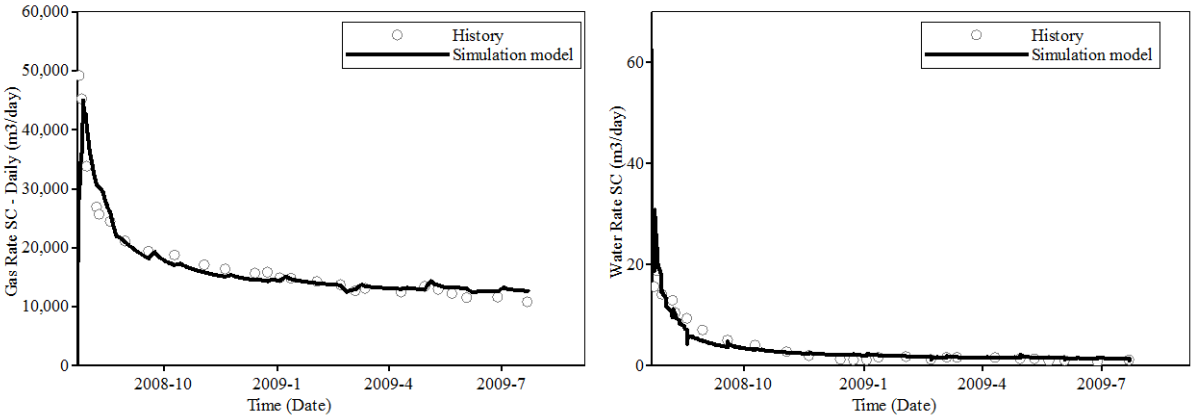

(a)

(b)

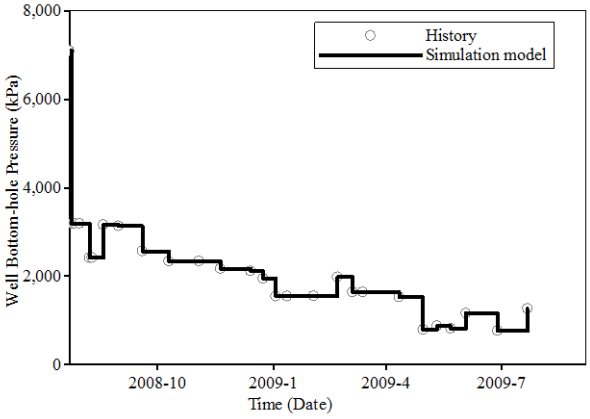

(c)

Figure 6-3 History match of base Barnett shale gas well model ((a) gas production rate of production history and simulation model; (b) water production rate of production history and simulation model; (c) well bottom-hole pressure of production history and simulation model).

6.4 Results and Discussion

6.4.1 Pore Size Distribution Effects

Figure 6-4 presents the gas apparent permeability and relative permeability curves of fractal-like tree pore systems with different pore radius separately. The largest pore radii are designed to be 450 nm, 500 nm and 550 nm in turn. Statistically, the mean values are 72.6 nm, 80.6 nm and 88.7 nm and the corresponding standard variances are 86.0 nm, 95.5 nm, 105.1 nm respectively. As with the aforementioned results, the pore system with larger pore radius owns a larger gas apparent permeability (Figure 6-4(a)) and relatively lower gas relative permeability (Figure 6-4(b)). For instance, if the radius increases from 450 nm to 550 nm, the apparent permeability increases from 3,922.4 nD to 5,774.2 nD, and the maximum relative water permeability increase from 0.904 to 0.912. This phenomenon is, once again, attributed to the larger gas flow path and the less dominant role of gas slippage. The improved fluid flow cross sectional area explains the increments of gas production and water production as reported in Figures 6-5(a) and 6-5(b), in which the cumulative gas production goes up to 14.7×10^6 m^3, 16.0×10^6 m^3, 17.2×10^6 m^3 separately and the cumulative water production changes from 2,242.0 m^3 to 2,448.8 m^3 and 2,651.4 m^3. The slight improvement in relative water permeability is the cause of a decreased gas-water ratio from 6,548.8 to 6,486.0 (Figure 6-6). Figure 6-7 captures the water drainage area within the pore networks of varying sizes. Owing to the decreased pervasion resistance from pores and the increased water relative flow capacity, water drainage area is gradually widened, which is identical to the descending trend of gas-water ratio in Figure 6-6. Figure 6-8 provides the pressure field profiles, assisting to verify the augment of fluid flow abilities in larger pores.

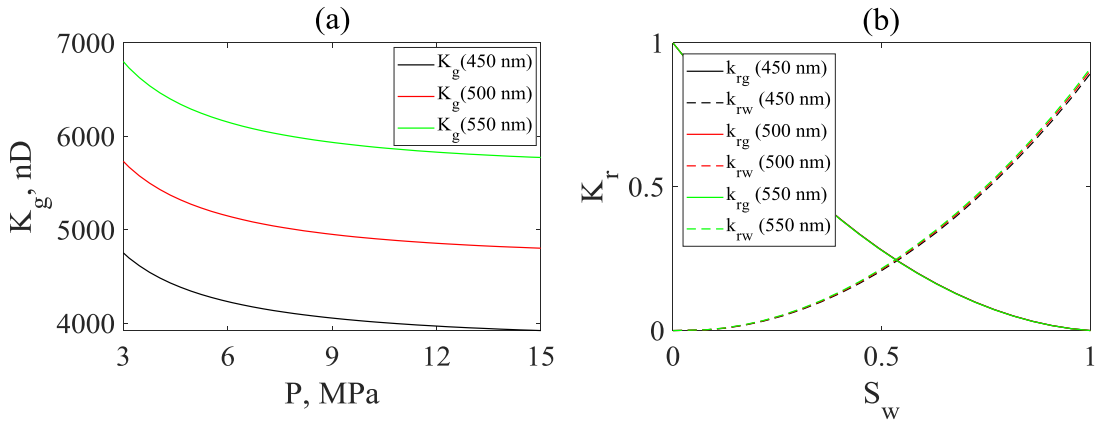

Figure 6-4 (a) Relationship between gas apparent permeability and pore radius; (b) relationship between relative permeability and pore radius.

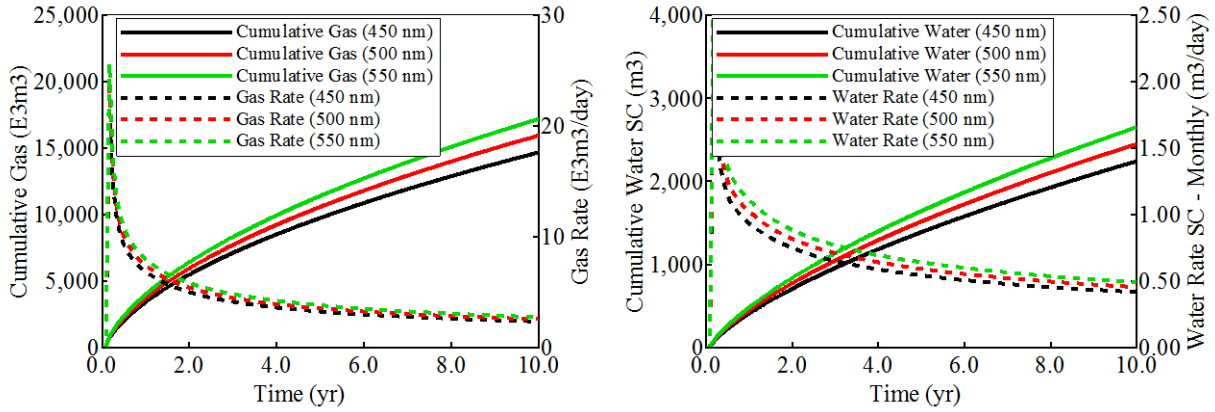

(a) (b)

Figure 6-5 (a) Relationship between cumulative gas production, gas rate and pore radius; (b) relationship between cumulative water production, water rate and pore radius.

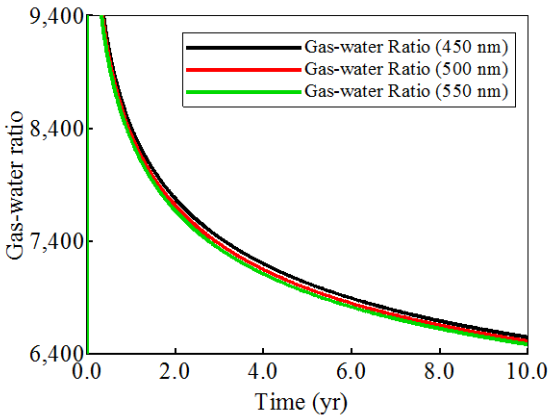

Figure 6-6 Gas-water ratios under different pore radius.

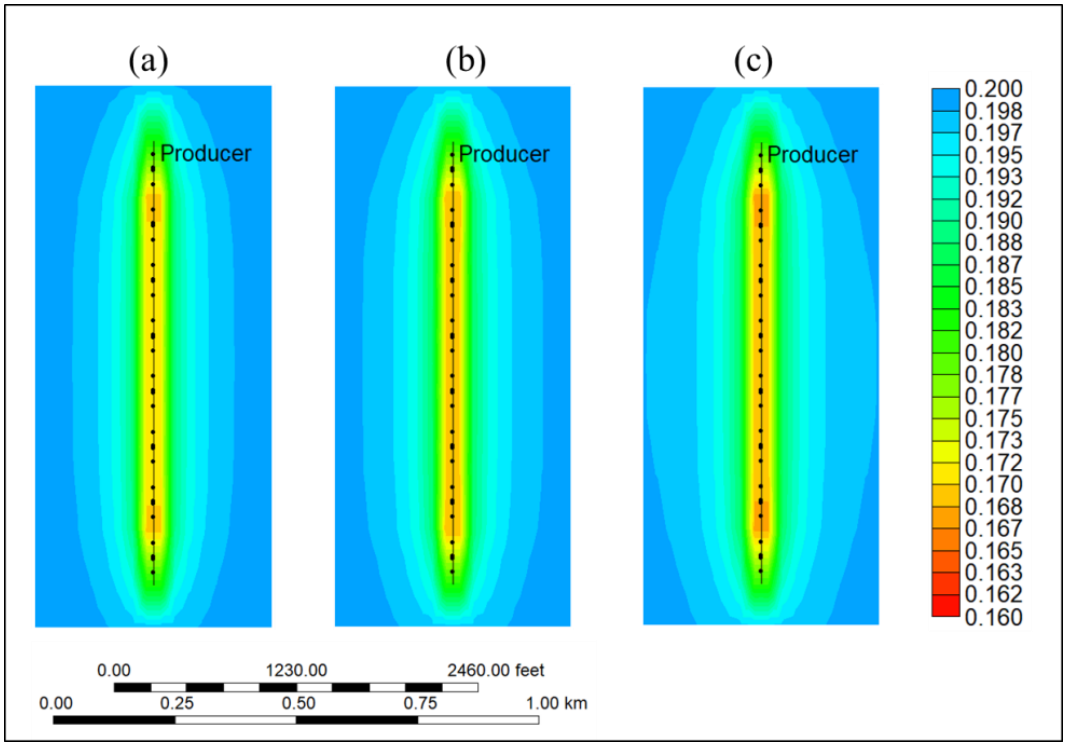

Figure 6-7 Maps of water distribution after 10 years: (a) 450 nm; (b) 500 nm; (c) 550 nm.

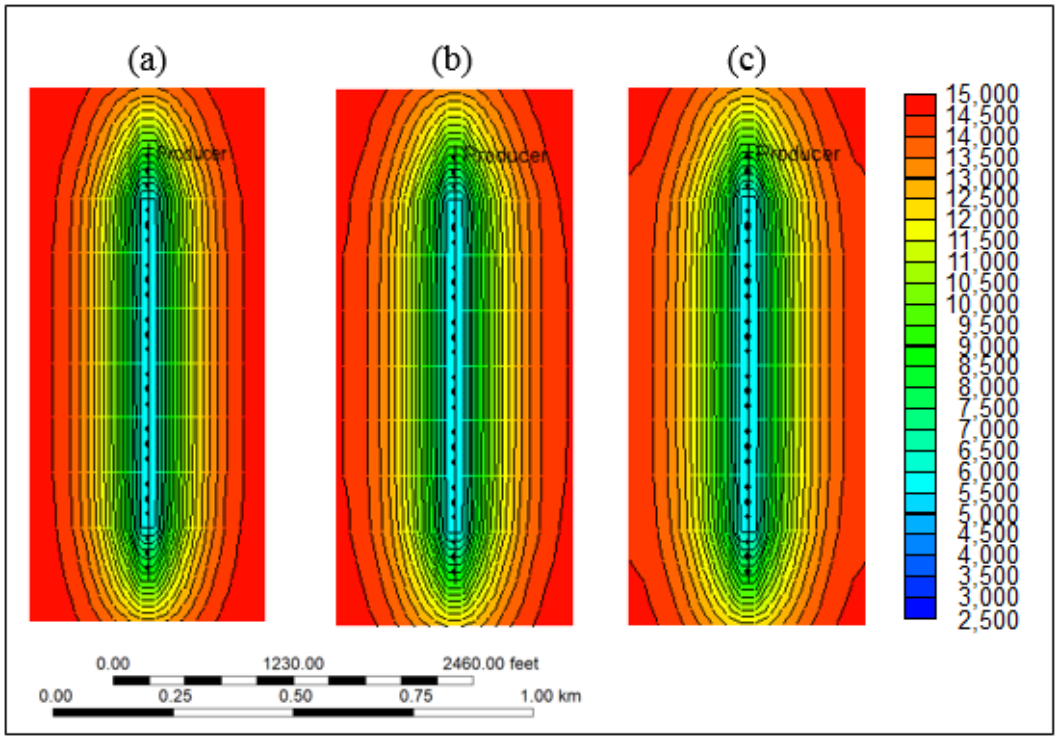

Figure 6-8 Maps of pressure after 5 years: (a) 450 nm; (b) 500 nm; (c) 550 nm.

Next is the examination of how pore radius deviation exerts impacts on gas production. Changing radius ratio from 0.5 to 0.9 obtains the mathematic mean values and standard variances reported in Figures 6-9(a) and 6-9(b). The mean value increases with the increase of radius ratio while the variance drops, representing a less complex and discrete pore network. In this case, with the increment of radius ratio from 0.5 to 0.9, the mean increases from 80.6 nm to 360.0 nm, and the standard deviation decreases from 95.5 nm to 44.2 nm. Figure 6-10 indicates a less discrete and complex pore network, represented by a lower radius ratio with the same maximum pore radius, tends to have a higher apparent permeability and water relative permeability. To be specific, the gas apparent permeability goes up to 65,394 nD from 4,925.9 nD. Simultaneously, the maximum water relative permeability is enlarged from 0.904 to 0.987 while the gas relative permeability is in almost constant level. This conclusion also agrees with the results in last chapter, the gas

permeability is slightly enhanced while the water relative permeability is significantly increased. Figures 6-11(a) and 6-11(b) demonstrate that both gas and water production are greatly increased in a less complex and discrete reservoir due to the expansion of flow path characterized by a higher apparent permeability. In this example, 22.0 $\times 10^6$ m^3 more gas and 3,700 m^3 more water have been recovered due to the alteration of pore structure. The gas-water ratio declines steadily from 6,548.8 to 6,195.6 at the beginning and then reaches a plateau at around 6,200 when the radius ratio goes up to 0.85 (Figure 6-11(c)), implying the downward trend of gas-water ratio provided with a less complex and discrete reservoir. The root cause lies in the variation rule of gas relative permeability along with the increase of the radius ratio, in which the gas relative permeability remains steady after an initial fall.

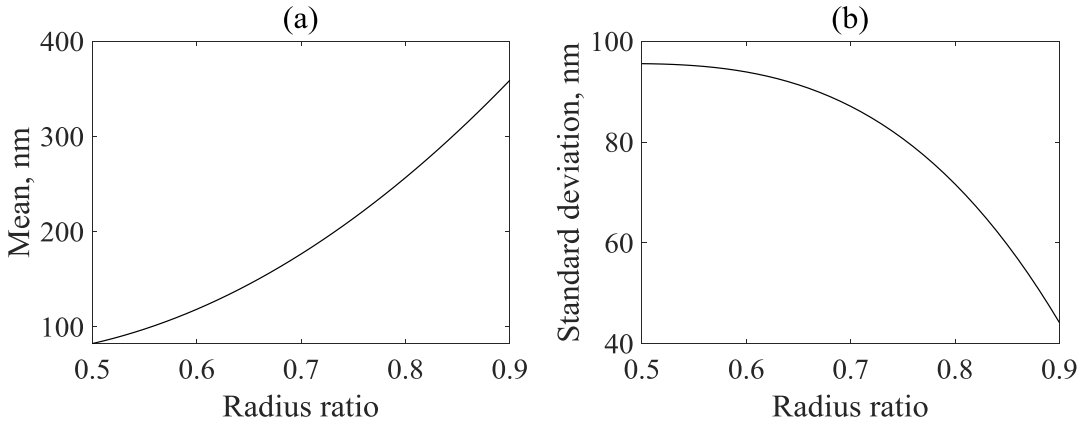

Figure 6-9 (a) Relationship between radius ratio and mean radius; (b) relationship between radius ratio and standard deviation.

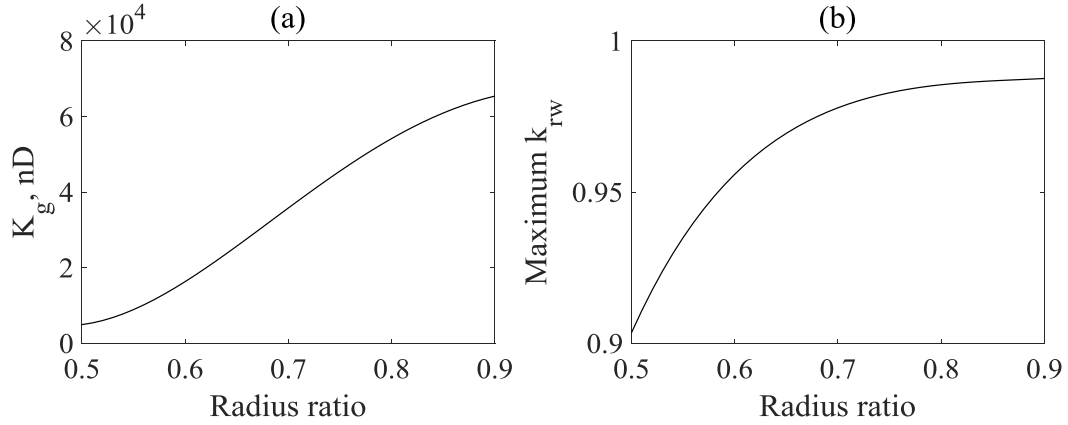

Figure 6-10 (a) Relationship between apparent permeability (15 MPa) and radius ratio; (b) relationship between maximum water relative permeability and radius ratio.

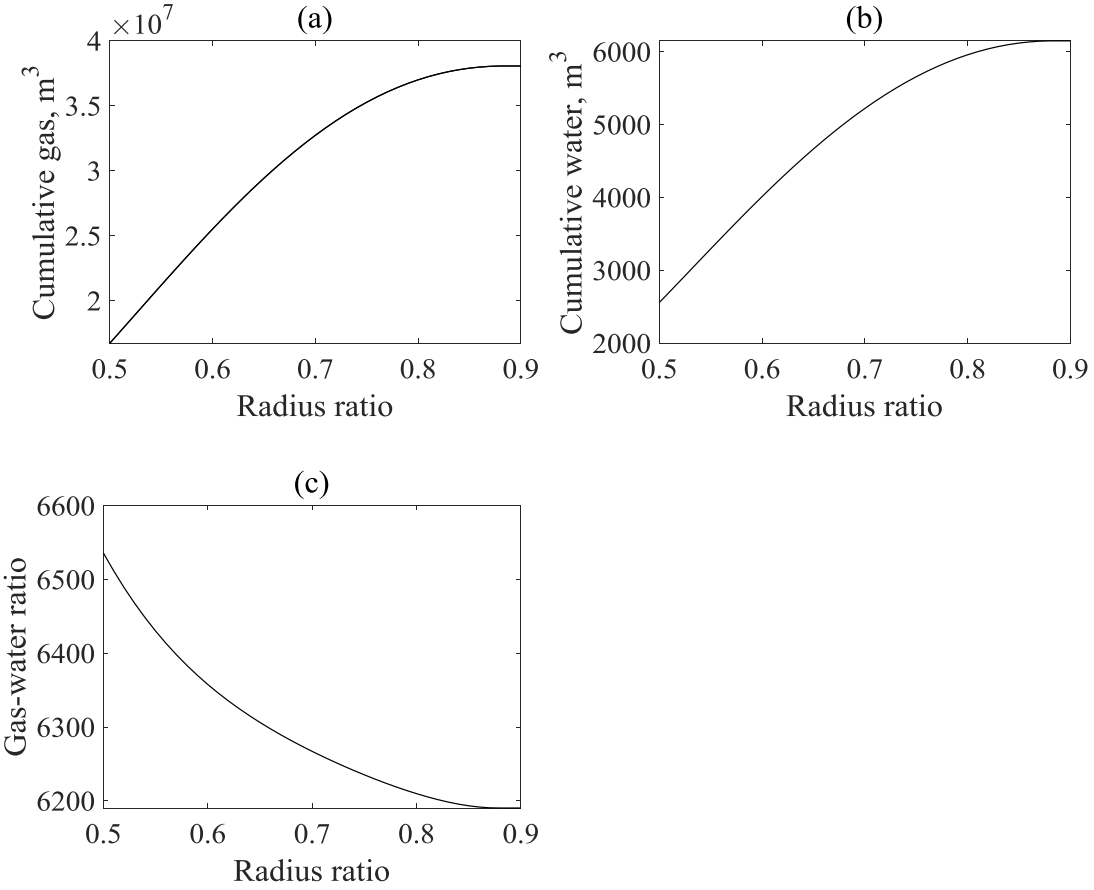

Figure 6-11 (a): Relationship between cumulative gas production and radius ratio; (b): relationship

between cumulative water production and radius ratio; (c): relationship between gas-water ratio and radius ratio.

6.4.2 Reservoir Properties Effects

Porosity is the intrinsic property of shale, which characterizes the storage capacity of fluids inside the pores. Initial water saturation decides the amount of water molecules working to disturb the gas flow behaviors. Figure 6-12 indicates the positive effect of a larger porosity and the negative effect of a higher water saturation on the gas apparent permeability. With the porosity of 0.12 and the water saturation of 0.1, the gas phase possesses an apparent permeability of 14,360.0 nD, far exceeding that (3,001.7 nD) of a reservoir with the porosity to be 0.04 and the water saturation to be 0.3 (Figure 6-12(a)). On one hand, a larger porosity offers more space for gas and water flow transport. On the other hand, for a specified space, a lower humidity provides more space for gas molecules movement. Figure 6-13 puts forward that the gas-water ratio is mainly controlled by water saturation while almost unaffected by the porosity. If say water saturation takes the value of 0.1, the gas-water ratios relative difference generated by the increase of porosity from 0.04 to 0.12 is only 0.06%. In order to better measure the impacts of water saturation and porosity on gas-water ratio, the main effect plot is presented in Figure 6-14. Obviously, water saturation plays a more important role in the determination of gas-water ratio. If the porosity changes from 0.04 to 0.12 the mean gas-water ratio remains almost unchanged. However, if the water saturation increases from 0.1 to 0.3, the average gas water ratio decreases by 4.4 times. However, both porosity and water saturation impacts the production rate to a significant extent. Holding the water saturation to be 0.1 and assigning 0.06, 0.08 and 0.10 to reservoir porosity obtains gas outputs of 24.4×10^6 m^3, 31.8×10^6 m^3 and 39.1×10^6 m^3 respectively (Figure 6-15). Keeping porosity as a constant

(0.1), raising the water saturation from 0.1 to 0.2 cuts down the gas output by 23.3% and improves the water production by 83.5% (Figure 6-16).

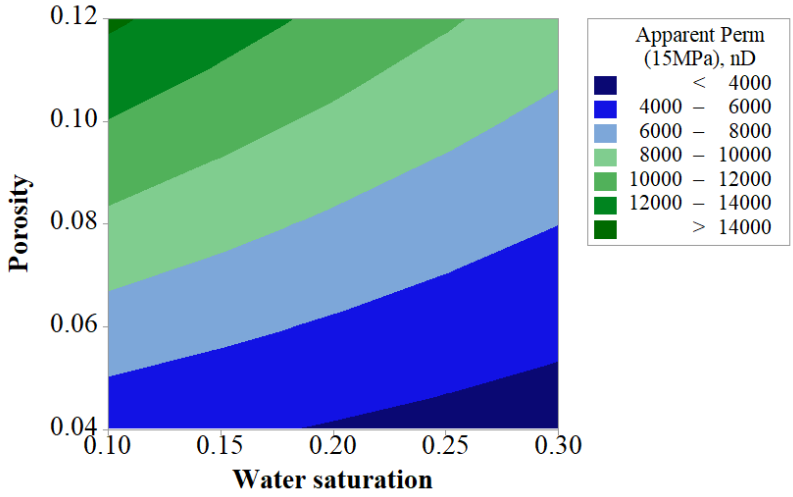

Figure 6-12 Contour-line map of apparent permeability (15 MPa) under different porosities and water saturations.

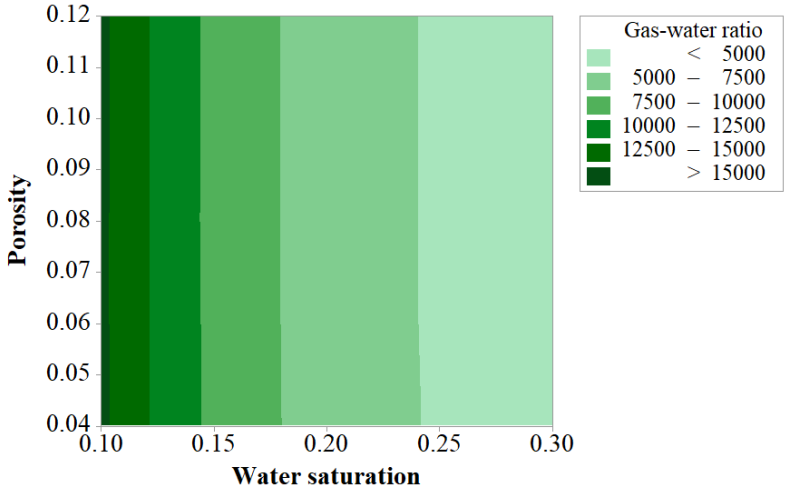

Figure 6-13 Contour-line map of gas-water ratio under different porosities and water saturations.

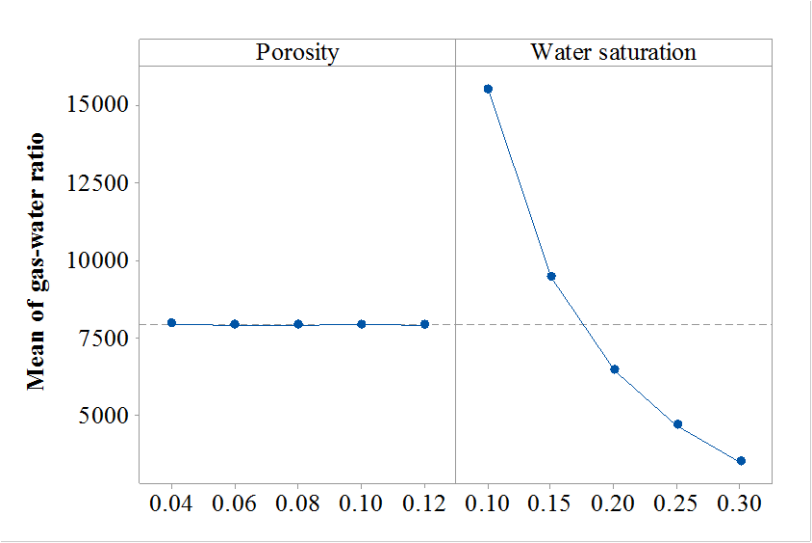

Figure 6-14 Main effect analysis of gas-water ratio.

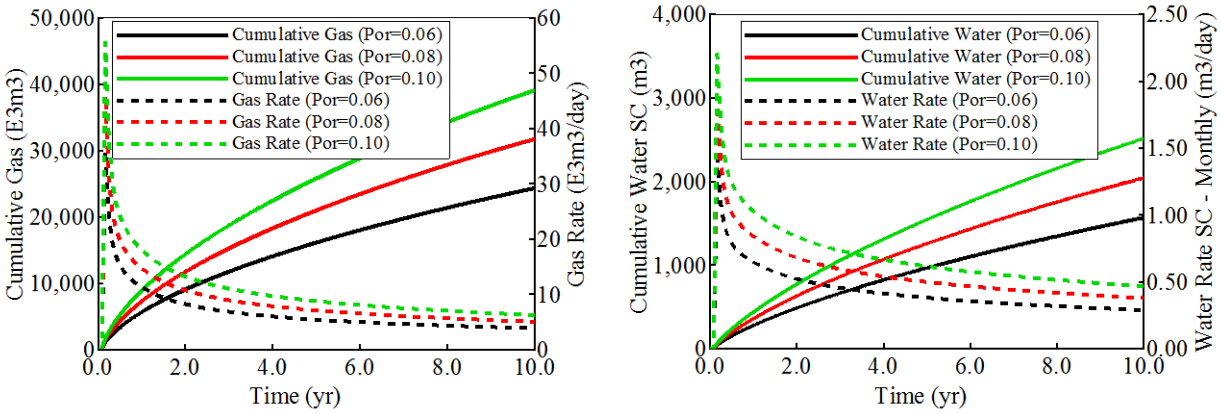

(a) (b)

Figure 6-15 (a) Cumulative gas production and gas rate under various porosity with the water saturation of 0.1; (b) cumulative water production and water rate under various porosity with the water saturation of 0.1.

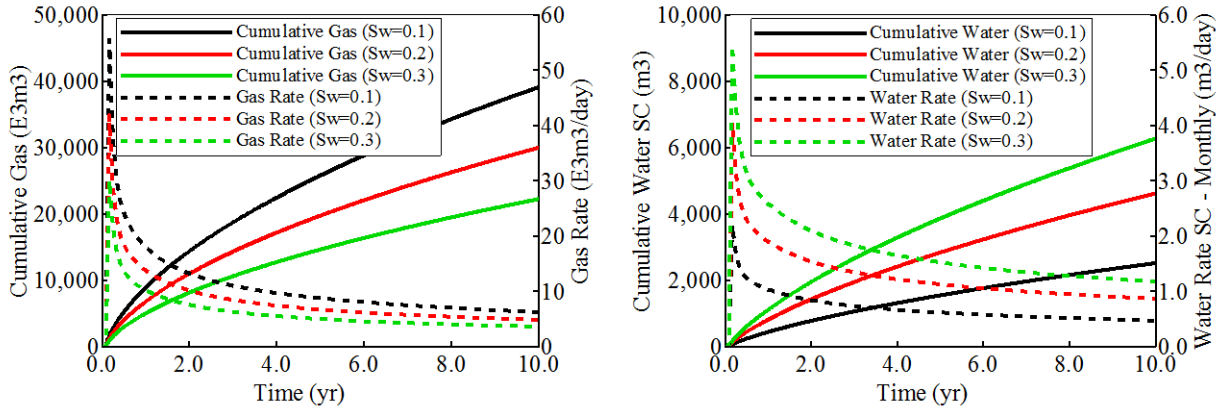

(a) (b)

Figure 6-16 (a) Cumulative gas production and gas rate under various water saturations with the porosity of 0.1; (b) cumulative water production and water rate under various water saturations with the porosity of 0.1.

6.4.3 Fracture Properties Effects

In order to study the nanoscale gas-water flow with different fracture properties, sensitivity analysis is performed towards a variety of fracture half-length and conductivities. Two sets of cases are designed: the first one considers all the mentioned mechanisms in this study, while the other one adopts the current relative permeability curves without the consideration of the apparent permeability enhancement during the production process. The relative differences between these two cases are calculated in terms of cumulative water production, cumulative gas production and gas-water ratio. Figure 6-17(a) calculates the water output relative differences between scenarios with different fracture half-lengths and fracture conductivities. Larger fracture half-length and fracture conductivity always make positive contributions to reduce the gap. Provided that the fracture conductivity stays at 1.650 mD·m, increasing fracture length from 25 m to 100 m bring down the relative difference of cumulative water production from 19.4% to 18.9%. It is speculated

that the fracture gradually dominates the water flow and the role of matrix becomes weaker during this process. The impact of fracture half-length and conductivities on gas output resembles their influences on water production. For smaller fracture half-length and conductivities, the relative difference of cumulative gas production is likely to be enhanced. For instance, if the fracture conductivity increases from 0.550 mD·m to 1.650 mD·m when the fracture half-length is fixed to be 75 m, the relative difference of cumulative gas decreases from 16.1% to 14.6%. Besides, it is noticeable that, under a small fracture half-length, the effect of fracture conductivity on the relative difference of cumulative gas production is rather small as a shorter fracture produces a smaller gas drainage area. Despite the similar tendencies of Figures 6-17(a) and 6-17(b), relative difference of gas-water ratio undergoes a rise when there is an increase in fracture half-length and conductivity (Figure 6-17(c)). For instance, the relative difference when the fracture half-length of 25 m and conductivity of 0.550 mD·m is 2.9%, and the relative difference under fracture half-length of 100 m and conductivity of 1.650 mD·m is 3.7% in comparison. The role of the relative permeability curve in the matrix gradually becomes weaker as the fracture gradually dominates the flow. As the relative difference of gas-water ratio is less than 5%, it is concluded that whether to consider apparent permeability alteration has minimal effect on gas-water ratio.

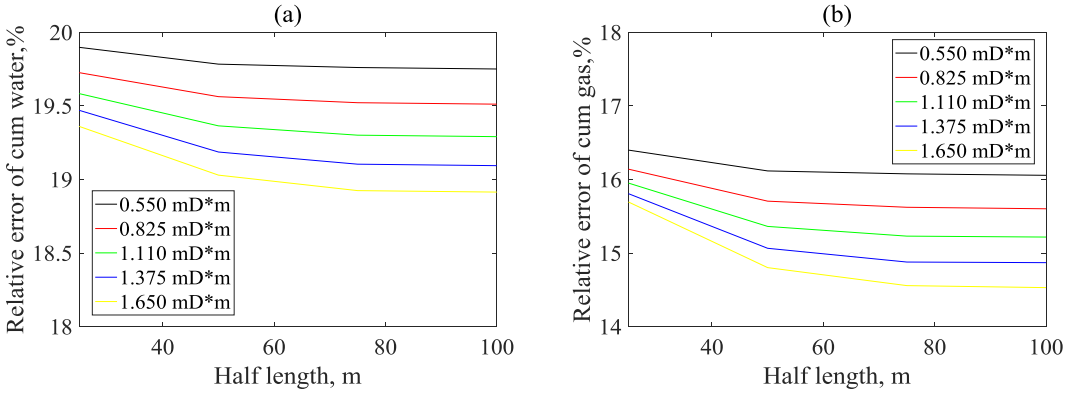

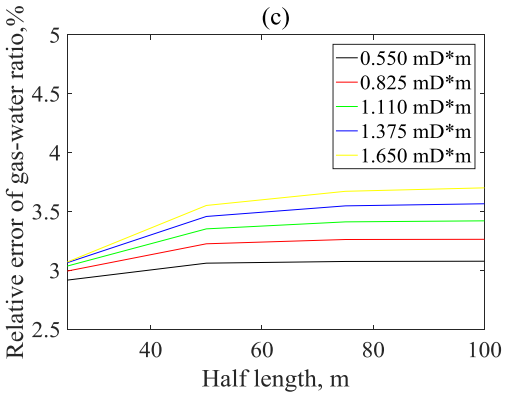

Figure 6-17 (a): Relationship between relative difference of cumulative water production and half-length under various fracture conductivities; (b) relationship between relative difference of cumulative gas production and half-length under various fracture conductivities; (c) relationship between relative difference of gas-water ratio and half-length.

6.5 Conclusions

Simulation study has been conducted with the derived gas apparent permeability model and the gas-water relative permeability curves after the history match with the production data. The following conclusions are obtained: (1) Because of the decreased pervasion resistance from larger pores, both gas output and water output are enhanced. Also, the consequent increased water relative flow capacity accounts for the decreased gas-water ratio. (2) A less complex and discrete reservoir owns larger gas production and water production but smaller gas-water ratio due to the enhanced water relative flow ability compared with the gas phase. (3) Increasing reservoir porosity and decreasing water saturation give rise to a larger gas production. The gas-water ratio is mainly controlled by water saturation while almost unaffected by porosity. (4) The role of matrix gradually becomes weaker as the fracture gradually dominates the flow when the fracture conductivity is increased.

CHAPTER SEVEN: CONCLUSIONS AND FUTURE WORK

Due to the initial water saturation and fracturing fluid injection, shale gas flow in shale nanopores is likely to be disturbed by the existence of water molecules. How the gas molecules transport with the existence of water molecules in nanoscale pores are detailed investigated in this study.

With the incorporation of water slippage and gas slippage, an analytical pressure-driven gas flow model in a single nanopore is put forward with the existence of water films. For low water saturation, the positive impacts of mobile high-viscosity water film on the gas flow capacity is enhanced given a smaller pore dimension and a larger reservoir pressure. Also, a hydrophobic surface provides larger water slippage and smaller water viscosity, contributing to a larger gas flow velocity. If there are extra water molecules, mobile bulk water layer is assumed to further affect gas transport behaviors, which is related to pore type, reservoir conditions and water saturation. A larger water saturation increases gas slip ratio due to the reduction of gas flow area, which also generates a drop of gas flow capacity. There is also a possibility that extra water molecules exist in form of a water bridge. In this case, the gas bubble movement can be predicted with the modified foam apparent viscosity. Next, the research focuses on the two phase flow in shale matrix with a bundle of pores rather than single nanopores. Gas-water relative permeability can be calculated according to the specific pore structure, with which shale gas reservoir simulation can be finally conducted. The increment of pore size lead to the increase of gas output and water output due to the expansion of flow area. The increased water relative flow capacity, which is generated by the drop of gas slip ratio, accounts for the decreased gas-water ratio. Likewise, a less complex and discrete reservoir owns larger gas production and water production but smaller gas-water ratio. Also, provided with a larger porosity and lower water saturation improves gas

production. But the gas-water ratio is mainly controlled by water saturation while almost unaffected by the porosity. Besides, the role of the relative permeability curve in the matrix gradually becomes weaker as the fracture gradually dominates the flow when the fracture conductivity is enhanced.

This study mainly employs analytical model and reservoir simulation to investigate the pressure-driven gas-water flow behaviors in hydrophilic shale nanopores. Molecular dynamic simulation can be used to further validate the results. Without the assumption of uniform water layer thickness, the variable water molecule distribution under different conditions can also be discussed. Also, the gas-water transport pattern in hydrophobic can be quite different, which can be studied in the short future to get a more comprehensive understanding of two phase flow in shale rocks. Simultaneously, instead of pure water, the effects of brine ions on the shale gas production requires to be analyzed.

APPENDIX A: CALCULATION OF CONTACT ANGLE

Physical forces are analyzed to obtain the disjoining pressure in shale pores, which is required to calculate the contact angle. The components of disjoining pressure are Van de Waals force, electrostatic force and structural force (Starov, 2007; Deryaguin, et al., 1987).

Van de Waals acts between all molecules at a relatively large distance and its interaction energy is inversely proportional to the distance. The molecular component of disjoining pressure can be obtained through the introduction of Hamaker constant (Equation (A-1)) (Starov, 2007; Deryaguin, et al., 1987):

$$\Pi_m(h_f) = \frac{A}{{h_f}^3} \tag{A-1}$$

where h_f is the film thickness, m; $\Pi_m(h_f)$ is the molecular component of disjoining pressure, Pa; A is the Hamaker constant, J. The Hamaker constant is highly related to a refractive index, a dielectric constant and adsorption frequencies (Israelachvili, 2011; Hirasaki, 1991):

$$A = \frac{3}{4k_BT}\left[\frac{\epsilon_1-\epsilon_3}{\epsilon_1+\epsilon_3}\right]\left[\frac{\epsilon_2-\epsilon_3}{\epsilon_2+\epsilon_3}\right] + \frac{3P_l v_e}{8\sqrt{2}} \frac{(n_1^2-n_3^2)(n_2^2-n_3^2)}{(n_1^2+n_3^2)^{1/2}(n_2^2+n_3^2)^{1/2}\left[\left(n_1^2+n_3^2\right)^{\frac{1}{2}}+\left(n_2^2+n_3^2\right)^{\frac{1}{2}}\right]} \tag{A-2}$$

where ϵ_i is the zero-frequency dielectric constant of material i, dimensinless; k_B is Boltzmann constant, 1.381×10^{-23} J/K; P_l is Planck constant, 6.626×10^{-34} J·s; T is temperature, K; n_i is the refractive index of material i, dimensionless, v_e is electronic adsortpion frequency, Hz. The first term stands for the effect of Keesom and Debye force while the second term describes the contribution of dispersion force.

Due to the surface group dissociation and unequal adsorption of anion and cation, the solid surface in an aqueous electrolyte solution is easily charged and an electric double layer tends to be

generated in the vicinity of a wall. If the electron clouds of two charged surfaces overlap with each other, electrostatic repulsion starts to act within a small distance. Its value is highly related to the electric potential. Electrostatic contribution adopts the following formation (Equation (A-3)) (Starov, 2007; Deryaguin et al., 1987):

$$\Pi_e(h_f) = \frac{\varepsilon\varepsilon_0(\xi_1-\xi_2)^2}{8\pi {h_f}^2} \quad \text{(A-3)}$$

where $\Pi_e(h_f)$ is the electrostatic component of disjoining pressure, Pa; ε is relative dielectric permittivity, dimensionless; ε_0 is an electric constant in vacuum, F/m; ξ is an electric potential at the interface, V.

As a polar liquid, the orientation structure of water molecules at a solid surface generates structural force, the value of which changes exponentially with the distance. In this case, empirical constants k_s and λ_{cl} representing the characteristic length of molecules are put forward to calculate the structual component (Equation (A-4)) (Starov, 2007; Deryaguin et al., 1987):

$$\Pi_s(h_f) = k_s e^{-\frac{h_f}{\lambda_{cl}}} \quad \text{(A-4)}$$

where $\Pi_s(h)$ is the structural component of disjoining pressure, Pa; k_s is a coefficient for structural force, N/m^2; λ_{cl} is the characteristic length of water molecules, m.

The stable water film thickness h_e on the inner surface of a slit pore can be calculated with disjoining pressure isotherms according to Tuller et al. (1999) and Li et al. (2016a).

$$\Pi_{slit}(h_e) = \Pi_1(h_e) + \Pi_2(h_e) + \Pi_3(h_e) \quad \text{(A-5)}$$

$$\Pi_1(h_e) = \frac{A_{gws}}{{h_e}^3} + \frac{\varepsilon\varepsilon_0(\xi_1-\xi_2)^2}{8\pi {h_e}^2} + k_s e^{-\frac{h_e}{\lambda_{cl}}} \quad \text{(A-6)}$$

$$\Pi_2(h_e) = \frac{A_{gws}}{(h-h_e)^3} + \frac{\varepsilon\varepsilon_0(\xi_1-\xi_2)^2}{8\pi(h-h_e)^2} + k_s e^{-\frac{(h-h_e)}{\lambda_{cl}}} \quad \text{(A-7)}$$

$$\Pi_3(h_e) = \frac{A_{wgw}}{(h-2h_e)^3} \quad \text{(A-8)}$$

where h_e is the water layer thickness, m; h is the pore height, m; $\Pi_{slit}(h_e)$ is the disjoining pressure in a slit pore, Pa; $\Pi_1(h_e)$ represents the force between the water film and its absorbed surface, Pa; $\Pi_2(h_e)$ represents the force between the water film and the opposite surface, Pa; $\Pi_3(h_e)$ represents the force between two water films, Pa; A_{gws} is the Hamaker constant of a gas-water-solid system, J; A_{wgw} is the Hamaker constant of a water-gas-water system, J; l is the characteristic wavelength, m; ε is relative dielectric permittivity of water, dimensionless; ε_0 is an electric constant in vacuum, F/m; ξ_1 is an electric potential at the solid-water interface, V; ξ_2 is an electric potential at the water-gas interface, V; k_s is a coefficient for the structural force, N/m^2; λ_{cl} is the characteristic length of water molecules, m.

The relationship between relative humidity and disjoining pressure is as follows and the stable water thickness h_e can be calculated with the combination of Equations (A-5) to (A-8) (Tuller et al., 1999):

$$\Pi_{slit}(h_e)V_m = -RTln\frac{P_v}{P_0} \quad \text{(A-9)}$$

where V_m is the water molar volume, m^3/mol; R is the gas constant, J/(mol▪K); T is temperature, K; P_v is the vapor partial pressure, Pa; P_0 is the saturated vapor pressure, Pa.

In terms of circular pores, the existence of surface curvature leads to modification of the disjoining pressure equation (Mattia, 2012) and h_e is deduced according to Equations (A-10) and (A-11).

The expressions for disjoining pressure and the relationship between relative humidity and the disjoining pressure for circular pore geometry are listed below:

$$\Pi_{circular}(h_e) = \frac{r}{r-h_e}\Pi_{flat}(h_e) + \frac{\gamma}{r-h_e} \quad \text{(A-10)}$$

$$\Pi_{circular}(h_e)V_m = -RTln\frac{P_v}{P_0} \quad \text{(A-11)}$$

where $\Pi_{flat}(h_e)$ is the disjoining pressure at flat surface, Pa, which takes the same form as $\Pi_1(h_e)$; r is the pore radius, m; $\Pi_{circular}(h_e)$ is the disjoining pressure in circular pores, Pa; γ is the gas-water surface tension, N/m.

Then a contact angle is calculated with isotherms of disjoining pressure to obtain the water rheological properties and boundary conditions in an interfacial region. According to Churaev (1995), following Equation (A-12) of Frumkin (1938) and Derjaguin (1940), when molecular force, electrostatic force and structural force are all considered the contact angle between a flat solid substrate and a fluid can be calculated as:

$$\cos\theta = 1 + \frac{1}{\gamma}\int_{h_e}^{\infty}\Pi_{flat}(h)dh \quad \text{(A-12)}$$

where θ is the contact angle, degree.

Mattia et al. (2012) analyzed the effects of nanoscale confinement on the film stability and the contact angle at the outer surface and inner surface of a capillary by the derivation of excess free energy and effective disjoining pressure. The contact angle at a curved substrate is obtained as Equation (A-13).

$$\cos\theta = \frac{1}{1-\frac{h_e}{r}} + \frac{1}{(1-\frac{h_e}{r})^2}\frac{1}{\gamma}\int_{he}^{\infty}\Pi_{flat}(h)dh \quad \text{(A-13)}$$

APPENDIX B: GAS APPARENT PERMEABILITY OF WEDGING PORES

B.1 Slit Pores with Mobile Bulk Water Film

The derivation process of the gas apparent permeability K_g with the consideration of a wedging effect is presented in this section. Equation (4-4) is modified as follows:

$$Q_g = [\frac{2}{3}\left(\frac{h}{2} - h_{wh} - h_{wb}\right)^3 + \frac{2-\sigma_v}{\sigma_v}\frac{2\lambda}{1-b\lambda}\left(\frac{h}{2} - h_{wh} - h_{wb}\right)^2 + \frac{\mu_g\left(\frac{h}{2}-h_{wh}-h_{wb}\right)}{\mu_{wb}}h_{wb}(h - 2h_{wh} - h_{wb}) + \frac{\mu_g\left(\frac{h}{2}-h_{wh}-h_{wb}\right)}{\mu_{wh}}(hh_{wh} + hl_{ls} - {h_{wh}}^2)](-\frac{\beta w}{\mu_g}\frac{dP}{dh}) \quad \text{(B-1)}$$

where $\frac{dP}{dh} = (\frac{dP}{dx})/(\frac{dh}{dx})$; $\frac{dP}{dx}$ is the pressure gradient, Pa/m, equaling to $-\frac{\Delta P}{L}$; $\Delta P = P_{in} - P_{out}$ is the pressure difference between the inlet pressure and the outlet pressure, Pa; $\beta = \frac{dh}{dx}$, which is a height decreasing rate along the flow direction, equaling to $-\frac{h_{in}-h_{out}}{L}$; h_{in} is a pore entrance height, m; h_{out} is a pore exit height, m; the wedging coefficient ς is the ratio of the pore entrance height and pore exit height.

To simplify the solving process, $y = \frac{h}{2} - h_{wh} - h_{wb}$ is introduced into Equation (B-1):

$$Q_g = \frac{-\left(\frac{h_{in}-h_{out}}{\mu_g}\right)}{\int_{\frac{h_{in}}{2}-h_{wh}-h_{wb}}^{\frac{h_{out}}{2}-h_{wh}-h_{wb}} \frac{1}{\frac{1}{3}y^3+ay^2+dy}dy}(\frac{\Delta PW}{L}) \quad \text{(B-2)}$$

where $a, d, f,$ and g are constants, $a = \frac{2-\sigma_v}{\sigma_v}\frac{\lambda}{1-b\lambda} + \frac{\mu_g h_{wb}}{\mu_{wb}} + \frac{\mu_g(h_{wh}+l_{ls})}{\mu_{wh}}$; $d = \frac{\mu_g {h_{wb}}^2}{2\mu_{wb}} + \frac{\mu_g {h_{wh}}^2}{2\mu_{wh}} + \frac{\mu_g h_{wh} h_{wb}}{\mu_{wh}} + \frac{\mu_g h_{wh} l_{ls}}{\mu_{wh}} + \frac{\mu_g h_{wb} l_{ls}}{\mu_{wh}}$; $f = \frac{2-\sigma_v}{\sigma_v}\frac{\lambda}{1-b\lambda} + \frac{\mu_g(h_{wh}+l_{ls})}{\mu_{wh}}$; $g = \frac{\mu_g {h_{wh}}^2}{2\mu_{wh}} + \frac{\mu_g h_{wh} l_{ls}}{\mu_{wh}}$.

In the case of Darcy's equation, the gas flow rate Q_{gd} takes the following form:

$$Q_{gd} = -\frac{K_g W h \beta}{\mu_g (1-S_w)} \frac{dP}{dh} \tag{B-3}$$

If the wedging coefficient is incorporated into (B-3), one obtains:

$$Q_g = \frac{K_g W}{\mu_g (1-S_w) ln\varsigma} \left(\frac{\Delta p}{L}\right) (h_{in} - h_{out}) \tag{B-4}$$

(B-2) and (B-4) are combined to get the gas apparent permeability K_g (Equation (4-18)).

B.2 Circular Pores with Mobile Bulk Water Film

Similarly, Equation (4-12) is modified below if the wedging coefficient is taken into account:

$$Q_g = \{\frac{1}{8}(r_0 - h_{wh} - h_{wb})^4 + \frac{2-\sigma_v}{\sigma_v} \frac{\lambda}{1-b\lambda} \frac{(r_0 - h_{wh} - h_{wb})^3}{2} + \frac{\mu_g (r_0 - h_{wh} - h_{wb})^2}{4\mu_{wb}} [h_{wb}(2r_0 - 2h_{wh} - h_{wb})] + \frac{\mu_g (r_0 - h_{wh} - h_{wb})^2}{4\mu_{wh}} (2r_0 l_{ls} - {h_{wh}}^2 + 2r_0 h_{wh})\}(-\beta \frac{\pi}{\mu_g} \frac{dP}{dr_0}) \tag{B-5}$$

where $\frac{dP}{dr_0} = (\frac{dP}{dx})/(\frac{dr_0}{dx})$; $\frac{dP}{dx}$ is the pressure gradient, Pa/m, equaling to $-\frac{\Delta p}{L}$; $\Delta P = P_{in} - P_{out}$ is the pressure difference between the inlet pressure and the outlet pressure, Pa; $\beta = \frac{dr_0}{dx}$, which is a radius decreasing rate along the flow direction, equaling to $-\frac{r_{0in} - r_{0out}}{L}$; r_{0in} is the pore entrance radius, m; r_{0out} is the pore exit radius, m; the wedging coefficient ς is the ratio of the pore entrance height and pore exit height.

To simplify the solving process, $y = r_0 - h_{wh} - h_{wb}$ is introduced into Equation (B-5):

$$Q_g = \frac{-(\frac{\pi}{\mu_g})(r_{0in} - r_{0out})}{\int_{r_{0in} - h_{wh} - h_{wb}}^{r_{0out} - h_{wh} - h_{wb}} \frac{1}{\frac{1}{8}y^4 + fy^3 + gy^2} dy} (\frac{\Delta p}{L}) \tag{B-6}$$

where $j = \frac{m}{2} + \frac{\mu_g h_{wb}}{2\mu_{wb}} + \frac{\mu_g (l_{ls}+h_{wh})}{2\mu_{wh}}$; $n = \frac{\mu_g {h_{wb}}^2}{4\mu_{wb}} + \frac{\mu_g {h_{wh}}^2}{4\mu_{wh}} + \frac{\mu_g h_{wh} h_{wb}}{2\mu_{wh}} + \frac{\mu_g l_{ls} h_{wh}}{2\mu_{wh}} + \frac{\mu_g l_{ls} h_{wb}}{2\mu_{wh}}$, $p = \frac{m}{2} + \frac{\mu_g (l_{ls}+h_{wh})}{2\mu_{wh}}$, $q = \frac{\mu_g {h_{wh}}^2}{4\mu_{wh}} + \frac{\mu_g l_{ls} h_{wh}}{2\mu_{wh}}$.

In the case of Darcy's equation, the gas flow rate Q_{gd} takes the following form:

$$Q_{gd} = -\frac{K_g \pi {r_0}^2 \beta}{\mu_g (1-S_w)} \frac{dP}{dr_0} \tag{B-7}$$

Taking the wedging coefficient into (B-7), one obtains:

$$Q_g = -\frac{K_g \pi (r_{0in} - r_{0out}) \varsigma r_{0out}}{\mu_g (1-S_w)(1-\varsigma)} \left(\frac{\Delta P}{L}\right) \tag{B-8}$$

(B-6) and (B-8) are incorporated to obtain the gas apparent permeability K_g (Equation (4-21)).

APPENDIX C: COPYRIGHT FORMS

RightsLink®

Home | Account Info | Help

Title:	Gas Transport in Shale Nanopores with Mobile High-Viscosity Water Film
Author:	Ran Li, Keliu Wu, Jing Li, et al
Publication:	Industrial & Engineering Chemistry Research
Publisher:	American Chemical Society
Date:	Aug 1, 2018

Logged in as:
Ran Li
LOGOUT

PERMISSION/LICENSE IS GRANTED FOR YOUR ORDER AT NO CHARGE

This type of permission/license, instead of the standard Terms & Conditions, is sent to you because no fee is being charged for your order. Please note the following:

- Permission is granted for your request in both print and electronic formats, and translations.
- If figures and/or tables were requested, they may be adapted or used in part.
- Please print this page for your records and send a copy of it to your publisher/graduate school.
- Appropriate credit for the requested material should be given as follows: "Reprinted (adapted) with permission from (COMPLETE REFERENCE CITATION). Copyright (YEAR) American Chemical Society." Insert appropriate information in place of the capitalized words.
- One-time permission is granted only for the use specified in your request. No additional uses are granted (such as derivative works or other editions). For any other uses, please submit a new request.

BACK | CLOSE WINDOW

REFERENCES

Adefidipe, O. A., Dehghanpour, H., & Virues, C. J. (2014, April). Immediate gas production from shale gas wells: a two-phase flowback model. In SPE Unconventional Resources Conference. Society of Petroleum Engineers.

Afsharpoor, A., & Javadpour, F. (2016). Liquid slip flow in a network of shale noncircular nanopores. Fuel, 180, 580-590.

Ali, T. A., & Sheng, J. J. (2015, October). Evaluation of the effect of stress-dependent permeability on production performance in shale gas reservoirs. In SPE eastern regional meeting. Society of Petroleum Engineers.

Atkins, P., & De Paula, J. (2006). Atkins' physical chemistry. New York, 77.

Baierlein, R. (2001). The elusive chemical potential. American Journal of Physics, 69(4), 423-434.

Bernard, G. G., & Holm, L. W. (1964). Effect of foam on permeability of porous media to gas. Society of Petroleum Engineers Journal, 4(03), 267-274.

Beskok, A., & Karniadakis, G. E. (1999). Report: a model for flows in channels, pipes, and ducts at micro and nano scales. Microscale Thermophysical Engineering, 3(1), 43-77.

Blake, T. D. (1990). Slip between a liquid and a solid: DM Tolstoi's (1952) theory reconsidered. Colloids and surfaces, 47, 135-145.

Blatt, H. (1982). Sedimentary petrology.

Blatt, H.; Robert, J. T. *Petrology: igneous, sedimentary, and metamorphic*; W.H. Freeman: New York, 1996, pp 281-292.

Bonaccurso, E., Butt, H. J., & Craig, V. S. (2003). Surface roughness and hydrodynamic boundary slip of a Newtonian fluid in a completely wetting system. Physical review letters, 90(14), 144501.

Borysenko, A., Clennell, B., Sedev, R., Burgar, I., Ralston, J., Raven, M., ... & Liu, K. (2009). Experimental investigations of the wettability of clays and shales. Journal of Geophysical Research: Solid Earth, 114(B7).

Brown, G. P., DiNardo, A., Cheng, G. K., & Sherwood, T. K. (1946). The flow of gases in pipes at low pressures. Journal of Applied Physics, 17(10), 802-813.

Bruus, H. (2008). Theoretical microfluidics (Vol. 18, p. 346). Oxford: Oxford university press.

Cao, P. (2017). Impact of multiphysics interactions on the gas flow performances in shale gas reservoirs.

Carey, J. M. (2012). Surprise side effect of shale gas boom: a plunge in us greenhouse gas emissions. Forbes Magazine.

Chalmers, G. R., Bustin, R. M., & Power, I. M. (2012). Characterization of gas shale pore systems by porosimetry, pycnometry, surface area, and field emission scanning electron microscopy/transmission electron microscopy image analyses: Examples from the Barnett, Woodford, Haynesville, Marcellus, and Doig units. AAPG bulletin, 96(6), 1099-1119.

Chen, J., Yu, B., Xu, P., & Li, Y. (2007). Fractal-like tree networks increasing the permeability. Physical Review E, 75(5), 056301.

Chen, S., & Doolen, G. D. (1998). Lattice Boltzmann method for fluid flows. Annual review of fluid mechanics, 30(1), 329-364.

Chen, X., Cao, G., Han, A., Punyamurtula, V. K., Liu, L., Culligan, P. J., ... & Qiao, Y. (2008). Nanoscale fluid transport: size and rate effects. Nano letters, 8(9), 2988-2992.

Chen, Y. D., & Yang, R. T. (1991). Concentration dependence of surface diffusion and zeolitic diffusion. AIChE journal, 37(10), 1579-1582.

Churaev, N. V. (1995). Contact angles and surface forces. Advances in Colloid and Interface Science, 58(2-3), 87-118.

Civan, F., & Donaldson, E. C. (1989). Relative permeability from unsteady-state displacements with capillary pressure included. SPE Formation Evaluation, 4(02), 189-193.

Clarkson, C. R., Solano, N., Bustin, R. M., Bustin, A. M. M., Chalmers, G. R. L., He, L., ... & Blach, T. P. (2013). Pore structure characterization of North American shale gas reservoirs using USANS/SANS, gas adsorption, and mercury intrusion. Fuel, 103, 606-616.

Cluff, R. M., & Byrnes, A. P. (2010, June). Relative permeability in tight gas sandstone reservoirs-the" Permeability Jail" model. In SPWLA 51st Annual Logging Symposium. Society of Petrophysicists and Well-Log Analysts.

CMG Reservoir Simulation Manual. (2016).

Curtis, M. E., Sondergeld, C. H., Ambrose, R. J., & Rai, C. S. (2012). Microstructural investigation of gas shales in two and three dimensions using nanometer-scale resolution imagingMicrostructure of Gas Shales. AAPG bulletin, 96(4), 665-677.

Darabi, H., Ettehad, A., Javadpour, F., & Sepehrnoori, K. (2012). Gas flow in ultra-tight shale strata. Journal of Fluid Mechanics, 710, 641-658.

Dehghanpour, H., Lan, Q., Saeed, Y., Fei, H., & Qi, Z. (2013). Spontaneous imbibition of brine and oil in gas shales: Effect of water adsorption and resulting microfractures. Energy & Fuels, 27(6), 3039-3049.

Derjaguin, B. V. (1940). Theory of capillary condensation and related capillary effects. Calculation of spreading action of polymolecular liquid films. Zh. Fiz. Khim, 14(2), 137.

Derjaguin, B. V., Churaev, N. V., & Muller, V. M. (1987). Wetting films. In Surface Forces (pp. 327-367). Springer, Boston, MA.

Engelder, T., Cathles, L. M., & Bryndzia, L. T. (2014). The fate of residual treatment water in gas shale. Journal of Unconventional Oil and Gas Resources, 7, 33-48.

Fan, D., & Ettehadtavakkol, A. (2017). Analytical model of gas transport in heterogeneous hydraulically-fractured organic-rich shale media. Fuel, 207, 625-640.

Feder, J. (1988). Fractals plenum. New York, 9.

Feng, D., Li, X., Wang, X., Li, J., Sun, F., Sun, Z., ... & Zhang, X. (2018). Water adsorption and its impact on the pore structure characteristics of shale clay. Applied Clay Science, 155, 126-138.

Fertl, W. H., & Rieke III, H. H. (1980). Gamma ray spectral evaluation techniques identify fractured shale reservoirs and source-rock characteristics. Journal of Petroleum Technology, 32(11), 2-053.

Frantz, J. H., Sawyer, W. K., MacDonald, R. J., Williamson, J. R., Johnston, D., & Waters, G. (2005, January). Evaluating barnett shale production performance-using an integrated approach. In SPE Annual Technical Conference and Exhibition. Society of Petroleum Engineers.

Frumkin, A. (1938). Phenomena of wetting and adhesion of bubbles. I. Zh. Fiz. Khim, 12(337), 337-45.

Ghanbarian, B., & Javadpour, F. (2017). Upscaling pore pressure‐dependent gas permeability in shales. Journal of Geophysical Research: Solid Earth, 122(4), 2541-2552.

Gilliland, E. R., Baddour, R. F., & Russell, J. L. (1958). Rates of flow through microporous solids. AIChE Journal, 4(1), 90-96.

Henderson, G. D., Danesh, A., Tehrani, D. H., Al-Shaidi, S., & Peden, J. M. (1998). Measurement and correlation of gas condensate relative permeability by the steady-state method. SPE Reservoir Evaluation & Engineering, 1(02), 134-140.

Higashi, K., Ito, H., & Oishi, J. (1963). Surface diffusion phenomena in gaseous diffusion. I.

Surface diffusion of pure gas. Nippon Genshiryoku Gakkaishi (Japan), 5.

Hirasaki, G. J. (1991). Wettability: fundamentals and surface forces. SPE Formation Evaluation, 6(02), 217-226.

Hirasaki, G. J., & Lawson, J. B. (1985). Mechanisms of foam flow in porous media: apparent viscosity in smooth capillaries. Society of Petroleum Engineers Journal, 25(02), 176-190.

Ho, T. A., & Striolo, A. (2015). Water and methane in shale rocks: Flow pattern effects on fluid transport and pore structure. AIChE Journal, 61(9), 2993-2999.

Hocking, L. M. (1976). A moving fluid interface on a rough surface. Journal of Fluid Mechanics, 76(4), 801-817.

Holt, J. K., Park, H. G., Wang, Y., Stadermann, M., Artyukhin, A. B., Grigoropoulos, C. P., ... & Bakajin, O. (2006). Fast mass transport through sub-2-nanometer carbon nanotubes. Science, 312(5776), 1034-1037.

Hu, Q., Zhang, Y., Meng, X., Li, Z., Xie, Z., & Li, M. (2017). Characterization of micro-nano pore networks in shale oil reservoirs of Paleogene Shahejie Formation in Dongying Sag of Bohai Bay Basin, East China. Petroleum Exploration and Development, 44(5), 720-730.

Huang, D. M., Sendner, C., Horinek, D., Netz, R. R., & Bocquet, L. (2008). Water slippage versus contact angle: A quasiuniversal relationship. Physical review letters, 101(22), 226101.

Huebner, W. F., & Barfield, W. D. (2016). Opacity. Springer.

Israelachvili, J. N. (2011). Intermolecular and surface forces. Academic press.

Jarrahian, A., & Heidaryan, E. (2014). A simple correlation to estimate natural gas viscosity. Journal of Natural Gas Science and Engineering, 20, 50-57.

Javadpour, F. (2009). Nanopores and apparent permeability of gas flow in mudrocks (shales and siltstone). Journal of Canadian Petroleum Technology, 48(08), 16-21.

Jerauld, G. R., & Salter, S. J. (1990). The effect of pore-structure on hysteresis in relative permeability and capillary pressure: pore-level modeling. Transport in porous media, 5(2), 103-151.

Jin, Z., & Firoozabadi, A. (2014). Effect of water on methane and carbon dioxide sorption in clay minerals by Monte Carlo simulations. Fluid Phase Equilibria, 382, 10-20.

Job, G., & Herrmann, F. (2006). Chemical potential—a quantity in search of recognition. European journal of physics, 27(2), 353.

Jung, C. M., Zhou, J., Chenevert, M. E., & Sharma, M. M. (2013, September). The impact of shale preservation on the petrophysical properties of organic-rich shales. In SPE Annual Technical Conference and Exhibition. Society of Petroleum Engineers.

Kapoor, A., Yang, R. T., & Wong, C. (1989). Surface diffusion. Catalysis Reviews—Science and Engineering, 31(1-2), 129-214.

Karniadakis, G. E. M., Beskok, A., & Gad-el-Hak, M. (2002). Micro flows: fundamentals and simulation. Applied Mechanics Reviews, 55, B76.

Klinkenberg, L. J. (1941, January). The permeability of porous media to liquids and gases. In Drilling and production practice. American Petroleum Institute.

Krohn, C. E. (1988). Fractal measurements of sandstones, shales, and carbonates. Journal of Geophysical Research: Solid Earth, 93(B4), 3297-3305.

Langlois, W. E., & Deville, M. O. (1964). Slow viscous flow (Vol. 105). New York: Macmillan.

Li, K., & Horne, R. N. (2004). Experimental study of gas slippage in two-phase flow. SPE Reservoir Evaluation & Engineering, 7(06), 409-415.

Li, J., Yin, J., Zhang, Y., Lu, S., Wang, W., Li, J., ... & Meng, Y. (2015). A comparison of experimental methods for describing shale pore features—a case study in the Bohai Bay Basin of eastern China. International Journal of Coal Geology, 152, 39-49.

Li, J., Du, C., & Zhang, X. (2011, January). Critical evaluations of shale gas reservoir simulation approaches: single porosity and dual porosity modeling. In SPE middle east unconventional gas conference and exhibition. Society of Petroleum Engineers.

Li, J., Li, X., Wang, X., Li, Y., Wu, K., Shi, J., ... & Yu, P. (2016a). Water distribution characteristic and effect on methane adsorption capacity in shale clay. International Journal of Coal Geology, 159, 135-154.

Li, J., Li, X., Wu, K., Wang, X., Shi, J., Yang, L., ... & Feng, D. (2016b). Water sorption and distribution characteristics in clay and shale: effect of surface force. Energy & Fuels, 30(11), 8863-8874.

Li, J., Li, X., Wu, K., Feng, D., Zhang, T., & Zhang, Y. (2017). Thickness and stability of water film confined inside nanoslits and nanocapillaries of shale and clay. International Journal of Coal Geology, 179, 253-268.

Li, J., Chen, Z., Wu, K., Li, R., Xu, J., Liu, Q., ... & Li, X. (2018). Effect of water saturation on gas slippage in tight rocks. Fuel, 225, 519-532.

Li, T., Song, H., Wang, J., Wang, Y., & Killough, J. (2016). An analytical method for modeling and analysis gas-water relative permeability in nanoscale pores with interfacial effects. International Journal of Coal Geology, 159, 71-81.

Liu, B., Qi, C., Zhao, X., Teng, G., Zhao, L., Zheng, H., ... & Shi, J. (2018). Nanoscale Two-Phase Flow of Methane and Water in Shale Inorganic Matrix. The Journal of Physical Chemistry C, 122(46), 26671-26679.

Liu, K., Sun, J., Zhang, H., Liu, H., & Chen, X. (2018). A new method for calculation of water saturation in shale gas reservoirs using VP-to-VS ratio and porosity. Journal of Geophysics and Engineering, 15(1), 224-233.

Liu, Y., & Zhu, Y. (2016). Comparison of pore characteristics in the coal and shale reservoirs of Taiyuan Formation, Qinshui Basin, China. International Journal of Coal Science & Technology, 3(3), 330-338.

Loucks, R. G., Reed, R. M., Ruppel, S. C., & Jarvie, D. M. (2009). Morphology, genesis, and distribution of nanometer-scale pores in siliceous mudstones of the Mississippian Barnett Shale. Journal of sedimentary research, 79(12), 848-861.

Ma, B., Shi, L., Huang, C., & Xu, Q. (2018). Effects of nanoscale pore structure on permeability and relative permeability loss analyzed by GPU enhanced Multiple-Relaxation-Time LBM. International Journal of Heat and Mass Transfer, 117, 584-594.

Majumder, M., Chopra, N., Andrews, R., & Hinds, B. J. (2005). Nanoscale hydrodynamics: enhanced flow in carbon nanotubes. Nature, 438(7064), 44.

Mandelbrot, B. B. (1983). The fractal geometry of nature (Vol. 173, p. 51). New York: WH freeman.

Mashl, R. J., Joseph, S., Aluru, N. R., & Jakobsson, E. (2003). Anomalously immobilized water: a new water phase induced by confinement in nanotubes. Nano Letters, 3(5), 589-592.

Mattia, D., & Calabrò, F. (2012). Explaining high flow rate of water in carbon nanotubes via solid–liquid molecular interactions. Microfluidics and Nanofluidics, 13(1), 125-130.

Moghaddam, R. N., & Jamiolahmady, M. (2016). Slip flow in porous media. Fuel, 173, 298-310.

Moncrieff J. (2009). Microstructure of shale. In SPWLA Annual Meeting, Houston, Texas.

Murray, C. D. (1926). The physiological principle of minimum work: I. The vascular system and the cost of blood volume. Proceedings of the National Academy of Sciences of the United States of America, 12(3), 207.

Myers, T. G. (2011). Why are slip lengths so large in carbon nanotubes?. Microfluidics and nanofluidics, 10(5), 1141-1145.

Navier, C. L. M. H. (1823). Mémoire sur les lois du mouvement des fluides. Mémoires de l'Académie Royale des Sciences de l'Institut de France, 6(1823), 389-440.

Neek-Amal, M., Peeters, F. M., Grigorieva, I. V., & Geim, A. K. (2016). Commensurability effects in viscosity of nanoconfined water. ACS nano, 10(3), 3685-3692.

Neto, C., Evans, D. R., Bonaccurso, E., Butt, H. J., & Craig, V. S. (2005). Boundary slip in Newtonian liquids: a review of experimental studies. Reports on Progress in Physics, 68(12), 2859.

Nikolov, K. (2014). Shale Gas and Snake Oil–Geological Characteristics of Continuous Petroleum Resources and Resource Abundance Evaluation Assessment Methodology for Shale Gas/Oil in Some European Countries

Novlesky, A., Kumar, A., & Merkle, S. (2011, January). Shale Gas Modeling Workflow: From Microseismic to Simulation--A Horn River Case Study. In Canadian Unconventional Resources Conference. Society of Petroleum Engineers.

Pan, C., Hilpert, M., & Miller, C. T. (2001). Pore-scale modeling of saturated permeabilities in random sphere packings. Physical Review E, 64(6), 066702.

Piquemal, J. (1994). Saturated steam relative permeabilities of unconsolidated porous media. Transport in Porous Media, 17(2), 105-120.

Qin, Z., & Buehler, M. J. (2015). Nonlinear viscous water at nanoporous two-dimensional interfaces resists high-speed flow through cooperativity. Nano letters, 15(6), 3939-3944.

Reme, A. B. (1999). Parameter Fitting and Calibration Study with a Commercial Foam Simulator. Diploma Thesis. Faculty of Applied Earth Sciences, Norwegian University of Sciences and Technology.

Roshan, H., Ehsani, S., Marjo, C. E., Andersen, M. S., & Acworth, R. I. (2015). Mechanisms of water adsorption into partially saturated fractured shales: An experimental study. Fuel, 159, 628-637.

Ross, D. J., & Bustin, R. M. (2009). The importance of shale composition and pore structure upon gas storage potential of shale gas reservoirs. Marine and petroleum Geology, 26(6), 916-927.

Ruckenstein, E., & Rajora, P. (1983). On the no-slip boundary condition of hydrodynamics. Journal of colloid and interface science, 96(2), 488-491.

Rushing, J. A., Newsham, K. E., & Van Fraassen, K. C. (2003, January). Measurement of the two-phase gas slippage phenomenon and its effect on gas relative permeability in tight gas sands. In SPE Annual Technical Conference and Exhibition. Society of Petroleum Engineers.

Rutter, E. H., Mecklenburgh, J., McKernan, R., & Taylor, R. (2015, September). Pressure-dependent Permeability of Shales. In Fourth International Conference on Fault and Top Seals.

Sakhaee-Pour, A., & Bryant, S. (2012). Gas permeability of shale. SPE Reservoir Evaluation & Engineering, 15(04), 401-409.

Sampath, K., & Keighin, C. W. (1982). Factors affecting gas slippage in tight sandstones of cretaceous age in the Uinta basin. Journal of Petroleum Technology, 34(11), 2-715.

Shabro, V., Torres-Verdin, C., & Javadpour, F. (2011, January). Numerical simulation of shale-gas production: from pore-scale modeling of slip-flow, Knudsen diffusion, and Langmuir desorption to reservoir modeling of compressible fluid. In North American Unconventional Gas Conference and Exhibition. Society of Petroleum Engineers.

Shan, C., Zhang, T., Guo, J., Zhang, Z., & Yang, Y. (2015). Characterization of the micropore systems in high-rank coal reservoirs of the southern Sichuan Basin, China. AAPG Bulletin, 99(11), 2099-2119.

Siddiqui, M. A. Q., Ali, S., Fei, H., & Roshan, H. (2018). Current understanding of shale wettability: A review on contact angle measurements. Earth-Science Reviews, 181, 1-11.

Simpson, J. P., & Dearing, H. L. (2000, January). Diffusion Osmosis-An unrecognized cause of shale instability. In IADC/SPE Drilling Conference. Society of Petroleum Engineers.

Singh, H., & Javadpour, F. (2013). Nonempirical apparent permeability of shale. Unconventional Resources Technology Conference (URTEC).

Slatt, R. M., & O'Brien, N. R. (2011). Pore types in the Barnett and Woodford gas shales: Contribution to understanding gas storage and migration pathways in fine-grained rocks. AAPG bulletin, 95(12), 2017-2030.

Stevens, P. (2012). The shale gas revolution: Developments and changes (p. 10). London: Chatham House.

Sondergeld, C. H., Ambrose, R. J., Rai, C. S., & Moncrieff, J. (2010, January). Micro-structural studies of gas shales. In SPE Unconventional Gas Conference. Society of Petroleum Engineers.

Sondergeld, C. H., Newsham, K. E., Comisky, J. T., Rice, M. C., & Rai, C. S. (2010, January). Petrophysical considerations in evaluating and producing shale gas resources. In SPE Unconventional Gas Conference. Society of Petroleum Engineers.

Song, W., Yao, J., Ma, J., Li, A., Li, Y., Sun, H., & Zhang, L. (2018). Grand canonical Monte Carlo simulations of pore structure influence on methane adsorption in micro-porous carbons with applications to coal and shale systems. Fuel, 215, 196-203.

Starov, V. M., Velarde, M. G., & Radke, C. J. (2007). Wetting and spreading dynamics. CRC press.

Sun, Z., Li, X., Shi, J., Zhang, T., & Sun, F. (2017). Apparent permeability model for real gas transport through shale gas reservoirs considering water distribution characteristic. International Journal of Heat and Mass Transfer, 115, 1008-1019.

Takbiri-Borujeni, A., Fathi, E., Kazemi, M., & Belyadi, F. (2019). An integrated multiscale model for gas storage and transport in shale reservoirs. Fuel, 237, 1228-1243.

Tan, J., Weniger, P., Krooss, B., Merkel, A., Horsfield, B., Zhang, J., ... & Tocher, B. A. (2014). Shale gas potential of the major marine shale formations in the Upper Yangtze Platform, South China, Part II: Methane sorption capacity. Fuel, 129, 204-218.

Thomas, M. M., & Clouse, J. A. (1990). Primary migration by diffusion through kerogen: II. Hydrocarbon diffusivities in kerogen. Geochimica et Cosmochimica Acta, 54(10), 2781-2792.

Thomas, J. A., & McGaughey, A. J. (2009). Water flow in carbon nanotubes: transition to subcontinuum transport. Physical Review Letters, 102(18), 184502.

Thompson, S. L., & Owens, W. R. (1975). A survey of flow at low pressures. Vacuum, 25(4), 151-156.

Tian, S., Ren, W., Li, G., Yang, R., & Wang, T. (2017). A theoretical analysis of pore size distribution effects on shale apparent permeability. Geofluids, 2017.

U.S. Energy Information Administration Page. (2016). https://www.eia.gov/todayinenergy/detail.php?id=27512.

Vidic, R. D., Brantley, S. L., Vandenbossche, J. M., Yoxtheimer, D., & Abad, J. D. (2013). Impact of shale gas development on regional water quality. Science, 340(6134), 1235009.

Wang, F. P., & Reed, R. M. (2009, January). Pore networks and fluid flow in gas shales. In SPE annual technical conference and exhibition. Society of Petroleum Engineers.

Wang, S., Feng, Q., Javadpour, F., Zha, M., & Cui, R. (2017, October). Multiscale modeling of shale apparent permeability: an integrated study of molecular dynamics and pore network model. In SPE Annual Technical Conference and Exhibition. Society of Petroleum Engineers.

Wang, W., Su, Y., Zhang, X., Sheng, G., & Ren, L. (2015). Analysis of the complex fracture flow in multiple fractured horizontal wells with the fractal tree-like network models. Fractals, 23(02), 1550014.

Wang, Y., Chen, Z., Morah, V., Knabe, R. J., & Appel, M. (2012). Gas-Phase Relative Permeability Characterization on Tight-Gas Samples. Petrophysics, 53(06), 393-400.

Wenzel, R. N. (1936). Resistance of solid surfaces to wetting by water. Industrial & Engineering Chemistry, 28(8), 988-994.

Whitby, M., Cagnon, L., Thanou, M., & Quirke, N. (2008). Enhanced fluid flow through nanoscale carbon pipes. Nano letters, 8(9), 2632-2637.

Wu, K., Li, X., Wang, C., Yu, W., & Chen, Z. (2015a). Model for surface diffusion of adsorbed gas in nanopores of shale gas reservoirs. Industrial & Engineering Chemistry Research, 54(12), 3225-3236.

Wu, K., Chen, Z., & Li, X. (2015b). Real gas transport through nanopores of varying cross-section type and shape in shale gas reservoirs. Chemical Engineering Journal, 281, 813-825.

Wu, K., Li, X., Wang, C., Chen, Z., & Yu, W. (2015c). A model for gas transport in microfractures of shale and tight gas reservoirs. AIChE Journal, 61(6), 2079-2088.

Wu, K., & Chen, Z. (2016). Review of gas transport in nanopores in shale gas reservoirs. Petroleum Science Bulletin, 1, 91.

Wu, K., Chen, Z., Li, X., Xu, J., Li, J., Wang, K., ... & Dong, X. (2017a). Flow behavior of gas confined in nanoporous shale at high pressure: Real gas effect. Fuel, 205, 173-183.

Wu, K., Chen, Z., Li, J., Li, X., Xu, J., & Dong, X. (2017b). Wettability effect on nanoconfined water flow. Proceedings of the National Academy of Sciences, 114(13), 3358-3363.

Wu, Q., Bai, B., Ma, Y., Ok, J. T., Yin, X., & Neeves, K. (2014). Optic imaging of two-phase-flow behavior in 1D nanoscale channels. Spe Journal, 19(05), 793-802.

Wu, Q., Ok, J. T., Sun, Y., Retterer, S. T., Neeves, K. B., Yin, X., ... & Ma, Y. (2013). Optic imaging of single and two-phase pressure-driven flows in nano-scale channels. Lab on a Chip, 13(6), 1165-1171.

Xiao, B., Fan, J., & Ding, F. (2012). Prediction of relative permeability of unsaturated porous media based on fractal theory and Monte Carlo simulation. Energy & Fuels, 26(11), 6971-6978.

Xu, J., Wu, K., Yang, S., Cao, J., Chen, Z., Pan, Y., & Yan, B. (2017). Real gas transport in tapered noncircular nanopores of shale rocks. AIChE Journal, 63(7), 3224-3242.

Xu, P., Qiu, S., Yu, B., & Jiang, Z. (2013). Prediction of relative permeability in unsaturated porous media with a fractal approach. International Journal of Heat and Mass Transfer, 64, 829-837.

Xu, P., Yu, B., Feng, Y., & Liu, Y. (2006). Analysis of permeability for the fractal-like tree network by parallel and series models. Physica A: Statistical Mechanics and its Applications, 369(2), 884-894.

Xue, B., Zhang, J., Tang, X., Yng, C., Chen, Q., Man, X., & Dang, W. (2016). Micro-pore Structure and Gas Accumulation Characteristics of Shale in the Longmaxi Formation, Northwest Guizhou. Petroleum Research, 1(2), 191-204.

Yang, D., Wang, W., Chen, W., Wang, S., & Wang, X. (2017). Experimental investigation on the coupled effect of effective stress and gas slippage on the permeability of shale. Scientific reports, 7, 44696.

Yang, F., Ning, Z. F., Zhang, S. D., Hu, C. P., Du, L. H., & Liu, H. Q. (2013). Characterization of pore structures in shales through nitrogen adsorption experiment. Natural Gas Industry, 33(4), 135-140.

Yang, F., Ning, Z., & Liu, H. (2014). Fractal characteristics of shales from a shale gas reservoir in the Sichuan Basin, China. Fuel, 115, 378-384.

Yang, R., Huang, Z., Yu, W., Li, G., Ren, W., Zuo, L., ... & Sheng, M. (2016). A comprehensive model for real gas transport in shale formations with complex non-planar fracture networks. Scientific reports, 6, 36673.

Yang, Y., Wu, K., Zhang, T., & Xue, M. (2015). Characterization of the pore system in an over-mature marine shale reservoir: A case study of a successful shale gas well in Southern Sichuan Basin, China. Petroleum, 1(3), 173-186.

Yu, B. (2006). Fractal dimensions for multiphase fractal media. Fractals, 14(02), 111-118.

Yu, B. (2008). Analysis of flow in fractal porous media. Applied Mechanics Reviews, 61(5), 050801.

Yu, B., & Li, J. (2001). Some fractal characters of porous media. Fractals, 9(03), 365-372.

Yu, B., & Liu, W. (2004). Fractal analysis of permeabilities for porous media. AIChE journal, 50(1), 46-57.

Yu, H., Zhu, Y., Jin, X., Liu, H., & Wu, H. (2019). Multiscale simulations of shale gas transport in micro/nano-porous shale matrix considering pore structure influence. Journal of Natural Gas Science and Engineering, 64, 28-40.

Yu, W., Wu, K., Sepehrnoori, K., & Xu, W. (2017). A comprehensive model for simulation of gas transport in shale formation with complex hydraulic-fracture geometry. SPE Reservoir Evaluation & Engineering, 20(03), 547-561.

Yuan, Y., Doonechaly, N. G., & Rahman, S. (2016). An analytical model of apparent gas permeability for tight porous media. Transport in porous media, 111(1), 193-214.

shale in Sichuan Province, China

Zhang, H., Ye, H., Zheng, Y., & Zhang, Z. (2011). Prediction of the viscosity of water confined in carbon nanotubes. Microfluidics and nanofluidics, 10(2), 403-414.

Zhang, Q., Dong, Y., Liu, S., Elsworth, D., & Zhao, Y. (2017). Shale Pore Characterization Using NMR Cryoporometry with Octamethylcyclotetrasiloxane as the Probe Liquid. Energy & Fuels, 31(7), 6951-6959.

Zhang, T., Li, X., Sun, Z., Feng, D., Miao, Y., Li, P., & Zhang, Z. (2017). An analytical model for relative permeability in water-wet nanoporous media. Chemical Engineering Science, 174, 1-12.

Zhao, T., Li, X., Ning, Z., Zhao, H., & Li, M. (2018). Molecular simulation of methane adsorption on type II kerogen with the impact of water content. Journal of Petroleum Science and Engineering, 161, 302-310.

Zhao, Y. L., Tang, X. C., Zhang, L. H., Tang, H. M., & Tao, Z. W. (2018). Numerical solution of fractured horizontal wells in shale gas reservoirs considering multiple transport mechanisms. Journal of Geophysics and Engineering, 15(3), 739.

Zhou, S., Liu, D., Cai, Y., & Tang, J. (2015). Pore Structure Characteristics of Shale Gas Reservoir of Yingcheng Formation in Lishu Depression, Songliao Basin. Acta Geologica Sinica (English Edition), 89(s1), 142-142.

Zhou, Z., & Rossen, W. R. (1995). Applying Fractional-Flow Theory to Foam Processes at the" Limiting Capillary Pressure". SPE Advanced Technology Series, 3(01), 154-162.